Synthesis and Characterization of Thermoelectric Oxides at Macro- and Nano-scales

Feiyue Ma

A dissertation

submitted in partial fulfillment of the

requirements for the degree of

Doctor of Philosophy

University of Washington

2015

Reading Committee:

Jiangyu Li, Chair

Jihui Yang

Joseph Garbini

Program Authorized to Offer Degree:

Mechanical Engineering

University of Washington

Abstract

Synthesis and Characterization of Thermoelectric Oxides at Macro- and Nano-scales

Feiyue Ma

Chair of the Supervisory Committee:
Professor Jiangyu Li
Department of Mechanical Engineering

Thermoelectric materials can directly convert a temperature difference into electrical voltage and vice versa. Due to this unique property, thermoelectric materials are widely used in industry and scientific laboratories for temperature sensing and thermal management applications. Waste heat harvesting, another potential application of thermoelectric materials, has long been limited by the low conversion efficiency of the materials. Potential high temperature applications, such as power plant waste heat harvesting and combustion engine exhaust heat recovery, make thermoelectric oxides a very promising class of thermoelectric materials. In this thesis, the synthesis and characterization of thermoelectric oxide materials are explored.

In the first part of this thesis, the measurement methodologies and instrumentation processes employed to investigate different thermoelectric properties, such as the Seebeck coefficient and

carrier concentration at the bulk scale and the thermal conductivity at the nanoscale, are detailed. Existing scientific and engineering challenges associated with these measurements are also reviewed. To overcome such problems, original parts and methodologies have been designed. Three fully functional systems were ultimately developed for the characterization of macroscale thermoelectric properties as well as localized thermal conductivity.

In the second part of the thesis, the synthesis of $Na_xCo_2O_4$, a thermoelectric oxide material, is discussed. Modification of both composition and structure were carried out so as to optimize the thermoelectric performance of $Na_xCo_2O_4$. Nanostructuring methods, such as ball milling, electrospinning, auto-combustion synthesis, and core-shell structure fabrication, have been developed to refine the grain size of $Na_xCo_2O_4$ in order to reduce its thermal conductivity. However, the structure of the nanostructured materials is very unstable at high temperature and limited improvement on thermoelectric performance is observed. Therefore, another technique was adopted to address this issue. A texturing process was also explored to optimize the $Na_xCo_2O_4$ structure. It was found that a highly textured structure can be obtained using a combined process of combustion synthesis, chemical demixing, and a flux method.

Table of Contents

List of Figures

List of Tables

ACKNOWLEDGMENTS

My deepest and sincerest gratitude goes to my advisor, Prof. Jiangyu Li. He has shown the ideal role model as a scientific researcher with his deep insight into materials science and persistence of the truth. I appreciate the endless encouragement as well as guidance he has provided to me for pursuing the research of my own interest. Also I would like to thank my committee members including Prof. Guozhong Cao, Prof. Jihui Yang, and Prof. Joseph Garbini for their valuable comments and advice.

I would like to thank all my lab mates, Liangjun, Yuanming, Yang, Chihou, Nataly, Peiqi, Ahmad and Yile, for their intellectual support and companionship through my time at UW. I am so lucky to have some friends from MSE department who were great researchers on thermoelectrics. Shanyu, I would like to thank you for all the valuable discussions and help on my experiments. Chris, I enjoyed every conversation we had, and I really appreciate your time on editing my writings. I also would like to thank the staff in UW ME machine shop, Kevin, Eamon, and Vee, for helping me improve my machining skills.

Lastly, I would like to thank my family for all their love and encouragement. For my parents who raised me with a love of science and supported me in all my pursuits. For the presence of my lovely daughter, Lilian, who brightened up every day of my life during the final stage of this Ph.D. study. And most of all for my beloved wife, Yanan Yuan, whom I am so lucky to have on my side while facing all the happiness, sadness, successes and failures. Thank you.

Chapter 1 Introduction

1.1 Overview

Energy, is a fundamental ingredient of human life, and exists in a variety of nature forms. For thousands of years, people learned to utilize different sources of energy, including coal, oil, wind, and solar. Such energy resources can be transformed into other useful forms of energy like heat, electricity and light. Electricity is one of the newest forms of energy that humans have mastered. Due to its versatility, controllability, instant availability and consumer-end cleanliness, electricity became one of the most preferred forms of energy immediately after its discovery. Nowadays, electricity is already an indispensable component of human life, and nearly all the other sources of energy are used for generating electricity so as to satisfy the needs of human society. In contrast, thermal energy is almost the oldest form of energy in human history. Almost all the other forms of energy will partially transform into thermal energy during consumption; such energy is often considered to be the unwanted "waste heat". For example, in a vehicle powered by a typical gasoline-fueled internal combustion engine, the vast majority of the fuel energy is lost as waste heat, while only 25% of the fuel energy is used for vehicle mobility and accessory power [1], as shown in Figure 1-1(A). Solar energy is among the most promising renewable energy resources, but photovoltaic solar cells are unable to harvest a large amount of energy in the infrared wavelength range, which comprises 42% of the total solar energy. This portion of solar energy is also lost as heat [2], as shown in Figure 1-1(B).

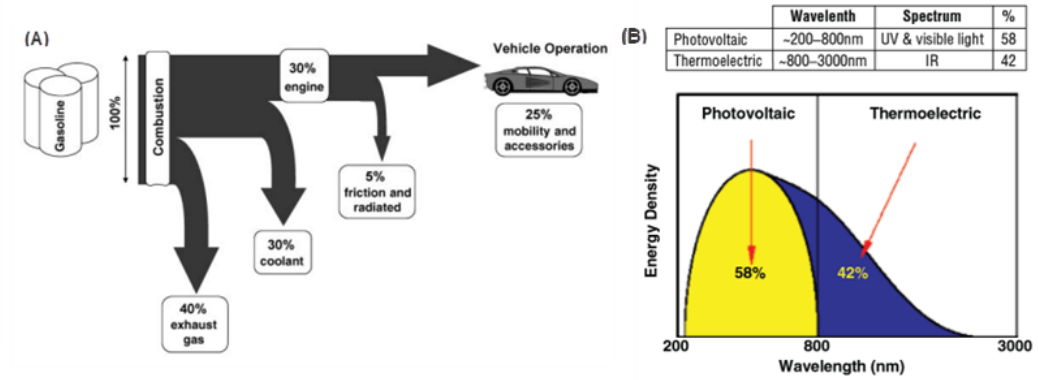

Figure 1-1 Potential applications of the thermoelectric energy conversion; (A) a vast amount of fuel energy lost as waste heat in combustion engines can be harvested by thermoelectric materials [1], (B) 42% of solar energy in the infrared spectrum lost as heat in photovoltaic conversion can also be harvested by thermoelectric materials [2].

The world energy crisis and concerns over the environmental have spurred a great deal of interest in the development of advanced technologies to improve the efficiency of energy utilization. In particular, considerable effort has been devoted to reducing the "waste" part of energy during consumption. Since the majority of energy subject to conversion is lost as heat, it would be advantageous to develop some techniques that can directly harvest the waste heat into some other useful forms of energy, and the most favorable of which would be electricity.

1.2 Thermoelectric Effects

Thermoelectric effects refer to three separately identified phenomena: the Seebeck effect, Peltier effect, and Thomson effect.

1.2.1 Seebeck effect

The Seebeck effect is named after Thomas Johann Seebeck, who first observed this phenomenon in 1821. An illustration of the experiment performed by Seebeck is shown in Figure 1-2. Here, a bimetallic loop of copper and bismuth wires was first constructed. When a burner was employed to heat one of the joints, deflections in a magnetic needle placed close to the loop were observed. This phenomenon was first explained, albeit incorrectly, as magnetic polarization produced by a temperature difference in the metals. After years of experiments and debate, it was concluded that what Seebeck has observed was actually due to ***an electrical current induced by disturbing the equilibrium of temperature***.

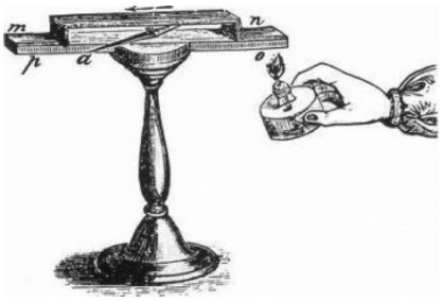

Figure 1-2 Illustration of Seebeck's Experiment [3].

So what happens in the materials on an atomic level? Considering a single, chemically homogeneous conductor subjected to a small thermal gradient, as shown in Figure 1-3. The charge carriers at the hot end of the material are more energetic (larger volume in the figure) and thus, they tend to flow to the cold end. Consequently, the colder region has more charge carriers per volume than the hot end, resulting in the establishment of an internal electrical potential that repels charge carriers arriving from the hot region. At the equilibrium, there will be a stable electrical

potential difference $\Delta V = (U_{hot} - U_{cold})$ between the two ends along with a temperature difference of $\Delta T = (T_{hot} - T_{cold})$ to balance the thermal driving force.

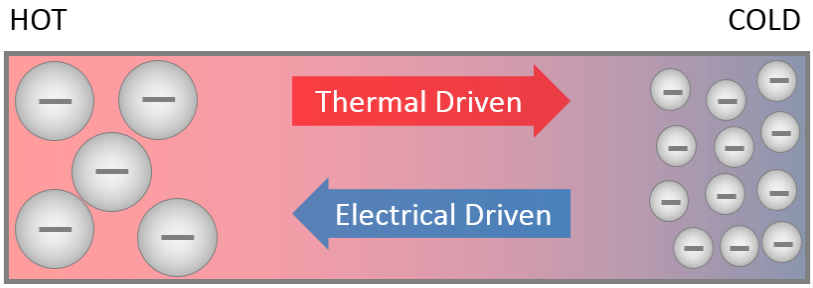

Figure 1-3 A simple microscopic schematic of the Seebeck effect.

At the same ΔT, the generated electrical potential ΔV could vary depending on the properties of the materials or average temperature. The Seebeck coefficient $S_x(T)$ is then used to quantify the relationship between ΔV and ΔT in a certain material at a fixed average temperature $T = (T_{hot} + T_{cold})/2$.

$$S_x(T) = -\lim_{\Delta T \to 0} \frac{\Delta V}{\Delta T} \tag{1.1}$$

The negative sign in Eq. (1.1) arises due to the sign convention employed for the Seebeck coefficient. According to this convention, a negative Seebeck coefficient is assigned to n-type materials that have negative charge carriers, such as electrons, as their major charge carrier. In reference to Figure 1-3, the cold end of the materials at equilibrium has more negative charge carriers and thus, a lower electrical potential than the hot end. Therefore, $\Delta V/\Delta T$ is positive and a negative sign is needed to fulfill the proposed sign convention.

1.2.2 Peltier effect

In 1834, about 13 years after the discovery of the Seebeck effect, Jean Peltier discovered that when an electrical current passing through a joint between two different conductors produces a heating

or cooling effect, depending on the direction of the current [4]. This phenomenon is now known eponymously as the Peltier Effect.

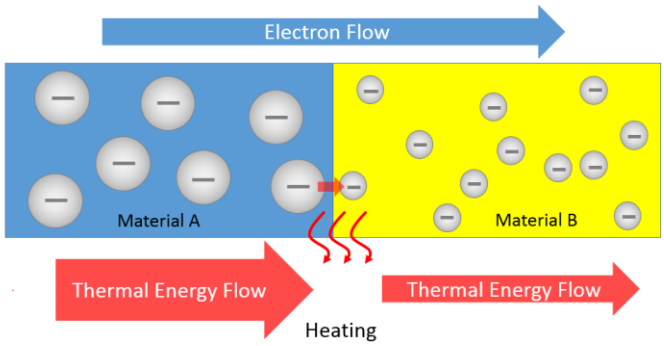

Figure 1-4 A simple microscopic schematic of the Peltier effect.

While the Peltier effect is considered to be the reverse effect of the Seebeck effect, but it is more difficult to be observed than the latter due to the significant role of Joule heating in most materials. At an atomic level, negative charge carriers flow opposite to the current direction, carrying both negative charges and thermal energy, as shown in Figure 1-4. At the junction of two different conductors, the carriers exchange charge and thermal energy so as to maintain a continuous electrical current across the boundary. However, the thermal energy of a single charge carrier can vary in different materials, even at the same temperature. This excess or deficiency in thermal energy ultimately leads to a temperature change at the junction.

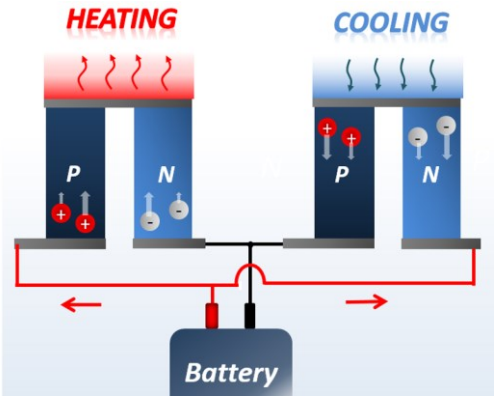

Figure 1-5 Thermocouples with p and n junctions.

In order to maximize the Peltier effect, the assembly shown in Figure 1-5 was established. This structure is called a thermocouple, and it represents a modern application of the Peltier and Seebeck effects. A thermocouple contains two parallel segments with Seebeck coefficients that are different in sign. When an electrical current is passed through the thermocouple, the contributions of both legs are identical. Similarly, when a temperature difference is established between the two sides, both legs yield comparable contributions to the generated Seebeck voltage.

1.2.3 Thomson effect

As discussed above, the Seebeck and Peltier effects share the same underlying physics. However, this notion was not realized until the year 1855, when William Thomson (Lord Kelvin) theoretically showed theoretically, from the principles of thermodynamics, that there is a close relationship between the Seebeck and Peltier effects [5]. Thomson also noticed that the Seebeck coefficient is not constant with respect to temperature for many materials, i.e., a temperature gradient present inside a conductor will be accompanied by a Seebeck (or Peltier) coefficient gradient inside the material. When current passes through this conductor, a thermal effect similar to the Peltier effect (either heating or cooling) will be continuously present along the conductor depending on the direction of the Seebeck coefficient gradient; this is known as the Thomson Effect.

The Thomson effect is even more difficult to observe or measure than the Seebeck and Peltier effects. Furthermore, there are also no obvious advantages of using the Thomson effect in practical applications. However, the Thomson effect is very important in fundamental research of the thermoelectric effect. While the Peltier and Seebeck coefficients can be easily determined for pairs of materials, ascertaining the absolute values of the Seebeck or Peltier coefficients for an individual material is difficult. In fact, the Thomson effect is the only thermoelectric phenomenon that can

be observed in individual materials. The Thomson coefficient, μ, is directly related to the Seebeck coefficient; it describes how the Seebeck coefficient changes with temperature. As such, the Thomson coefficient provides a method from which an absolute scale of the Seebeck coefficient for all thermoelectric materials can be established.

1.3 Thermoelectric Device and Applications

The thermoelectric effects can directly convert temperature difference into electric voltage and vice versa. Based on these effects, many different applications and devices have been developed over the last century, including major applications in temperature measurement, electronic refrigeration and energy harvesting.

1.3.1 Temperature measurement

Thermocouples are tools that are used to measure the temperature of an object based on the Seebeck effect. As shown in Figure 1-6, a thermocouple is composed of two different metal wires connected at one joint. Normally the two free ends of the thermocouple are located at a place far from the joint and have a fixed temperature T_0, called reference point. When the temperature of joint is changing, there will be a voltage generated across the circuit due to the Seebeck effect, which is directly related to the temperature of joint T. Based on the type of thermocouple materials and the reference point temperature, the temperature of joint can be obtained using the measured voltage signal. It is worth noting here that the thermocouple actually measures the temperature difference between the joint and the free ends. The actual temperature of the joint is corrected through cold junction compensation techniques.

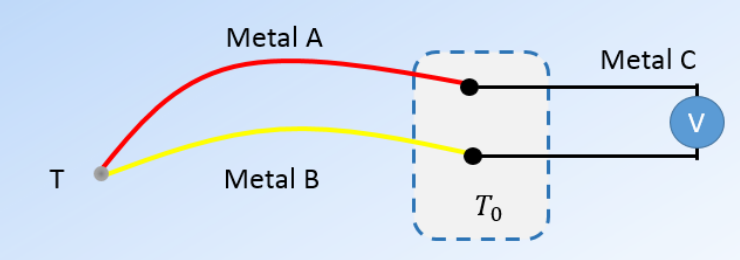

Figure 1-6 An example of a thermocouple measuring circuit.

Thermocouples are very widely used in both industry and scientific laboratories due to their numerous advantages, including:

- *Wide measurement range*

  Using different types of thermocouples, temperatures from 2K to over 2000K can be measured.

- *High precision and accuracy*

  Using a nanovoltmeter, a temperature measurement resolution of 0.001K or better can be achieved.

- *High reliability and reproducibility*

  For thermocouples of the same type, the temperature measurement results do not depend on the length and diameter of the thermocouple wires, while the generated voltage signal only depends on the temperature at the joint and free ends, rather than the thermal path of the entire wire.

- *Local measurements*

  As discussed above, a thermocouple measures the temperature at its joint. So the measured area could be as small as the joint of thermocouple, and the diameter of smallest thermocouple joint is reported to be less than 100 nm [6].

- *Fast response*

The response time of a thermocouple is around one millisecond, and is limited by the cooling and heating time of the joint. Normally thinner thermocouple wires have a shorter response time.

- *Compatible with electronics data acquisition devices*

  Measuring temperature with thermocouples is the same as measuring analog voltages signal. It is very easy to be incorporated into an electronic system for automatic temperature logging.

1.3.2 Electronic refrigeration

Another major application of thermoelectric effect is Peltier device, using Peltier effect for electronic refrigeration. As shown in Figure 1-5, when an electrical current passes through the module, it pumps the heat from one side to the other side. By simply reversing the current direction, the direction of heat flow reverses. Therefore this type of device is also considered as a heat pump and used as both heater and cooler for fast and accurate temperature modulation.

Peltier device is fully solid state, and no mechanical parts is moving when operating, so it is much quieter and more reliable than the conventional compressor based refrigeration, and the size of the module can be scale down to millimeter size. Because of those advantages, Peltier devices have been used in laser cooling, CPU cooling, and portable refrigerators. However, its application for large scale cooling has been limited because of its low energy efficiency, as discussed later.

1.3.3 Energy harvesting

Recently, there are great interests in the development of thermoelectric energy harvesting devices. This type of device is based on Seebeck Effect, similar to the thermocouple temperature sensor. Instead of using the electrical signal to sense the temperature, those electrical energies are

harvested for other use. Since the signal of a single thermocouple is in microvolts range, hundreds of couples are connected in series to boost the power output voltage, as shown in Figure 1-7.

Figure 1-7 Thermoelectric device with multi-thermocouples.

These thermoelectric generators have no moving parts, and are more compact and quieter than conventional heat engines. One of the potential applications is wasted heat recovery in power plants for additional electrical power. Automotive thermoelectric generators are in development for increased fuel efficiency of vehicles. Thermoelectric generators have also been used by NASA in space exploration for long time continuous power generation, where radioisotopes are used as the hot source [1].

Nevertheless, thermoelectric generators have been limited for widespread practical applications, because of its low energy conversion efficiency and high manufacturing cost.

1.4 Conversion Efficiency of Thermoelectric Devices

Conversion efficiency is one of the most important parameters for energy conversion devices, including Peltier devices and thermoelectric generators.

For a thermoelectric energy harvesting device, the conversion efficiency is defined as the ratio between the electrical power delivered to the load and the heat absorbed at the hot junction.

$$\Phi = \frac{Energy\ Supplied\ to\ the\ Load}{Heat\ Absorbed\ at\ Hot\ Junction} \tag{1.2}$$

In the formula above, Φ represents the conversion efficiency at device level, which is related to the materials properties, the device geometry, and the electronic load condition.

Since the device geometry and external electronic load could be different from device to device, it is necessary to develop a more universal metric that is independent of these factors and only depends on the intrinsic materials properties, so that the process of materials optimization could be separated from device level optimization.

To facilitate materials optimization, the dimensionless figure of merit (*ZT*), which only depends on thermoelectric properties of materials, has been derived in the following form [5]:

$$ZT = \frac{S^2\sigma}{\kappa}T \tag{1.3}$$

Here, σ, S, and κ are the electrical conductivity, Seebeck coefficient, and thermal conductivity of a given thermoelectric materials, respectively, and T is the working temperature. The dimensionless figure of merit represents the best efficiency one can obtain based on the given properties of a material. Furthermore, the maximum efficiency of a thermoelectric device made from one material depends on its *ZT* as follows:

$$\Phi = \eta\frac{\sqrt{1+ZT}-1}{\sqrt{1+ZT}+T_{cold}/T_{hot}}, \eta = 1 - T_{cold}/T_{hot} \tag{1.4}$$

Here, T_{cold} is the temperature of the cold side, T_{hot} is the temperature of hot side, T is the average temperature, and η is Carnot efficiency, which set the upper limit for thermoelectric devices.

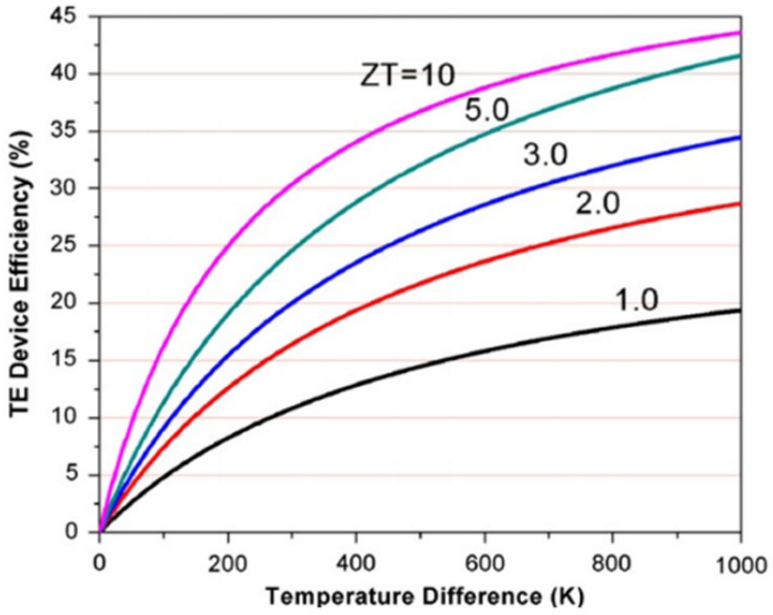

Figure 1-8 Relationship between conversion efficiency and *ZT*.

The thermoelectric conversion efficiencies versus imposed temperature difference for different *ZT* are shown in Figure 1-8. For a thermoelectric materials with *ZT*=3 operating between 500 C and 30 C, the conversion efficiency is around 25%, approximately half of the Carnot efficiency. Higher *ZT* values above 3 do not significantly increase the final conversion efficiency. Therefore, the Holy Grail of thermoelectric research is trying to achieve a *ZT* value on the order 2~3[2].

The value of *Z* is related to the Seebeck coefficient (S), electrical conductivity (σ), and thermal conductivity (κ) of the thermoelectric materials. In order to improve the conversion efficiency of thermoelectric devices, we need find materials that have a combination of these properties for a large *Z* value. This is not an easy task, since the figure of merit is intimately related to its electric and thermal transport properties. A large *Z* value not only requires high Seebeck coefficient, but

also high electric conductivity and low thermal conductivity. This turns out to be rather challenging, since high electric conductivity is usually accompanied by high thermal conductivity. In fact the total thermal conductivity of thermoelectric materials can be divided into two parts: electron contribution and phonon contribution. Electron contribution of thermal conductivity is proportional to electric conductivity according to Wiedemann-Franz Law, and this makes the reduction of phonon contribution to thermal conductivity the remaining option to enhance *ZT* by manipulating the ratio of electrical and thermal conductivity. Furthermore, the Seebeck coefficient is connected with the electrical conductivity through the density of state of charge carriers [7], for example, the electrical conductivity and Seebeck coefficient of semiconductors usually have an opposite relationship with charge carrier concentrations, as shown in Figure 1-9, making it necessary to optimize the carrier concentration for enhanced power factor $S^2\sigma$.

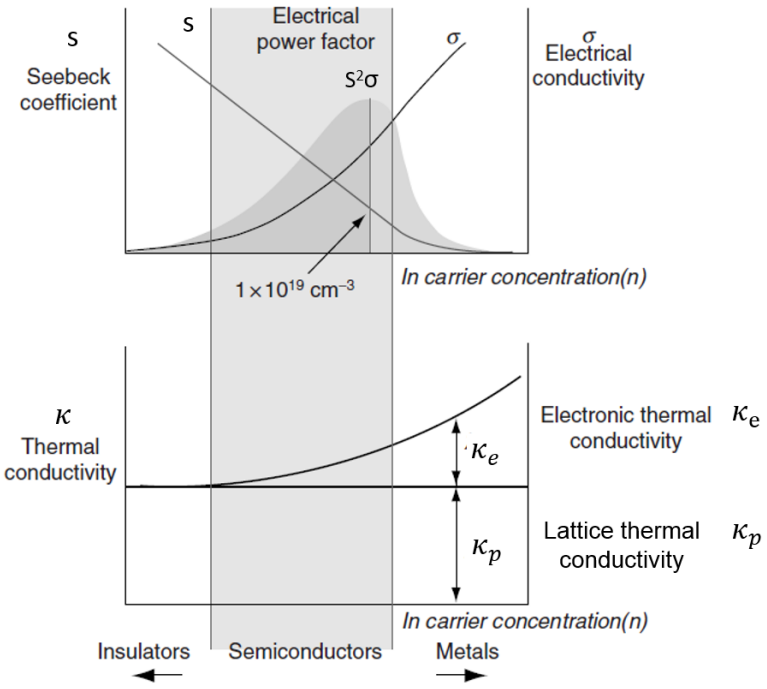

Figure 1-9 Relationship between thermoelectric properties and carrier concentration.

1.5 State-of-the-Art of Thermoelectric Materials

In the past decade, there are mainly two strategies in developing high performance thermoelectric materials: (1) searching for bulk materials with intrinsically high conversion efficiency; and (2) engineering nanostructured materials to enhance and optimize the conversion efficiency. While a few bulk thermoelectric materials have been developed successfully, for example skutterudite material system [7] with a *ZT* value larger than unity, in this thesis, we will focus on nanostructure thermoelectric materials that offer more degrees of freedom in controlling and optimizing their thermoelectric performance.

1.5.1 Nanostructured thermoelectric materials

Nanostructured materials are particularly suitable for thermoelectric applications. Compared to their bulk counterpart, there is increased electron density of states at the Fermi level in nanostructured materials, leading to potentially high Seebeck coefficient [8, 9] It is also possible to exploit phonon scattering at boundaries and interfaces in nanostructured materials to reduce thermal conductivity without compromising their electric conductivity too much [8]. Both strategies are helpful for improving thermoelectric figure of merit. Many nanostructured thermoelectric materials have been explored based on these two ideas, including low-dimensional system such as nanowires, nanotubes, and superlattices, and bulk thermoelectric materials with nanostructured components, such as nanocrystalline materials and nanocomposites.

Ideas of using superlattices to improve thermoelectric figure of merit was first proposed in 1990s [10, 11] taking advantage of quantum size effects on electron energy states as well as phonon scattering at interfaces. Extensive experimental and theoretical investigations were carried out afterward along this line, and enhanced *ZT* in various superlattice systems have been reported [12],

including Bi_2Te_3/Sb_2Te_3, Bi_2Te_3/Bi_2Se_3, and PbSeTe/PbTe, with *ZT* as high as 3.5 reported [13, 14]. Other low-dimensional materials, such as one-dimensional nanowires and nanotubes, have also been extensively investigated for their thermoelectric properties, including carbon nanotubes and silicon nanowires [8]. It has been reported that silicon nanowires with diameter in the range of 10s nanometers exhibit thermal conductivity 100-fold smaller than bulk silicon, while their Seebeck coefficient and electric conductivity remain essentially the same as bulk silicon, leading to a 100-fold improvement in thermoelectric figure of merit [15, 16]. While low-dimensional materials have demonstrated exciting thermoelectric conversion efficiency, it remains challenging to integrate these nanowires, nanotubes, and superlattices into bulk thermoelectric modules. The fabrication process of low-dimensional materials is often slow, expensive, and not easy to scale up, and the electric and thermal parasitic resistances in thermoelectric modular assembly using low-dimensional materials often lead to much degraded thermoelectric performance.

To overcome these difficulties, nanocrystalline materials and nanocomposites incorporating low-dimensional nanoparticles and nanowires have drawn increased attentions [17-21]. When appropriately designed, these nanostructured materials can have thermal conductivity reduced while Seebeck coefficient increased, for example by controlling carrier energy filtering, quantum confinement, and phonon scattering at grain boundary, resulting in substantially enhanced thermoelectric figure of merit [22, 23]. Indeed, it was reported that a peak *ZT* value of 1.4 have been achieved in nanocrystalline BiSbTe alloy, which is 40% higher than BiSbTe bulk alloys without nanocrystalline structure [8]. Such an enhancement is attributed to the low thermal conductivity caused by the increased phonon scattering at grain boundaries and defects. A large enhancement in thermoelectric power is also observed in nanocomposites consisting of bismuth nanowires embedded in porous alumina and porous silica [24] Recently, a *ZT* value of 1.5 has been

reported in nanostructured $Ag_{0.8}Pb_{m+x}SbTe_{m+2}$, which shows simultaneously enhanced electric conductivity and reduced thermal conductivity [25]. These studies demonstrate that nanostructured materials are very promising for thermoelectric applications, and phonon scattering at grain boundaries and interfaces is very effective in reducing thermal conductivity and improving thermoelectric efficiency.

1.5.2 Thermoelectric oxides

A *ZT* value of one or larger is generally considered to be necessary for practical applications and many of tellurium-, antimony- and germanium- based compounds [1, 26-29] have already exceeded that requirement. However, the stability and toxicity of these compounds is an issue for some applications, especially at higher temperature. In the last decade, some oxides of less toxic elements have been discovered to have good thermoelectric properties. Although their figure of merit is lower compare to those compounds mentioned above, their stability in the air and at high temperature with large temperature difference is much better, with lower materials cost and small negative environmental impact. Two of such oxides will be introduced next.

The most promising p-type oxide thermoelectric materials are those based on alkali or alkaline-earth cobaltite [30]. Figure 1-10 shows the crystal structures of $NaCo_2O_4$, $Ca_3Co_4O_9$, and $Bi_2Sr_2Co_2O_x$ [31-36]. They are layered materials consisting of complex crystalline structure, similar to artificially engineered superlattices [32]. In these layered oxides, CoO_2 nanosheets possessing a strongly correlated electron system serve as electronic transport layer, while the intercalate layers, such as sodium ions layer inside $NaCo_2O_4$ structure, serve as phonon scattering regions. As a result, it is possible to control and optimize electron and phonon transports separately and thus enhance their thermoelectric figure of merit. Numerous studies suggested that such

layered cobalt oxides exhibits low thermal conductivity and metallic like electrical conductivity [37, 38], and thus behave like phonon-glass and electron-crystal, very attractive for thermoelectric applications. Indeed, *ZT* value as high as 1.2 has been reported in $NaCo_2O_4$ single crystal [39][38], and a highest *ZT* of 0.8 has been reported in polycrystalline $NaCo_2O_4$ [40].

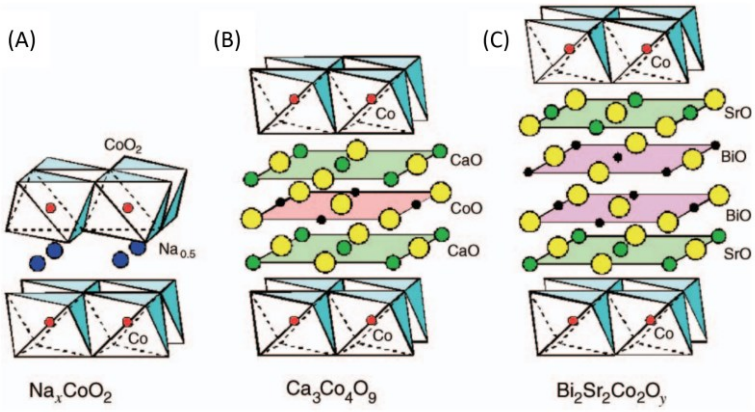

Figure 1-10 Schematic illustration of the crystal structure of CoO_2-based thermoelectric oxides: (A) Na_xCoO_2, (B) $Ca_3Co_4O_9$, and (C) $Bi_2Sr_2Co_2O_y$.

Compare to p-type oxides, n-type oxides seem to have wider ranges. There are several popular material systems, including $SrTiO_3$, $CaMnO_3$ and ZnO.

$SrTiO_3$ is a good electronic conductor when doped with higher valence ions, which act as electron donor [41, 42]. $CaMnO_3$ is typically doped to improve thermoelectric properties, like $SrTiO_3$, and can be doped on both Ca and Mn site [43, 44]. ZnO also requires doping for adequate n-type conduction. A *ZT* value as high as 0.6 has been reported for Al and Ga dual doped ZnO [45], and a *ZT* value of 0.44 is reported of Al doped ZnO fabricated through nanostructuring process to reduce the thermal conductivity [46]. Recently another strategy has been proposed for good n-type thermoelectric materials, where oxygen deficiency in transition metal oxides is suggested for n-

type conduction with large Seebeck effect. One of the example is reduced TiO_2, which have been found to have a *ZT* as high as 0.5 [47]. Nevertheless, it is note that the n-type oxides still have lower *ZT* compare to p-type cobaltite, though recent research on oxygen deficiency may provide a way to break the limit.

In contrast to traditional non-oxide compounds, few researches have been carried out on nanostructuring of thermoelectric oxides for improved conversion efficiency. The synthesis, measurement, and application condition of thermoelectric oxide could be very different from non-oxides. For example, one has to eliminate the oxygen content for a repeatable Seebeck coefficient measurement at high temperature for nearly all the non-oxide materials, but using the same measurement condition for the oxide materials the result could be very different. So it is necessary to develop synthesis and characterization methods designed for thermoelectric oxide materials.

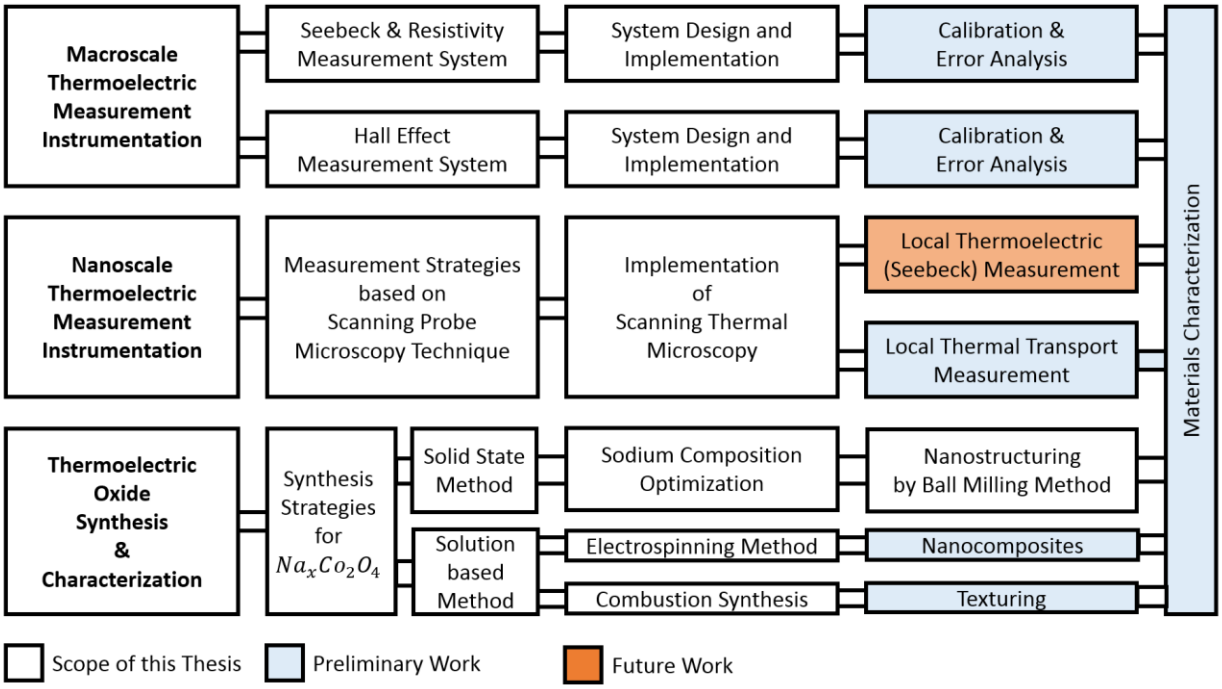

Figure 1-11 The scope of this thesis.

1.6 Scope of the Thesis and Contributions

Figure 1.11 shows the scope of this thesis, which is composed of three main parts covering the following topics: instrumentation for macroscale thermoelectric measurement, instrumentation for nanoscale thermoelectric measurement, and thermoelectric oxide synthesis and characterization. A brief summary of the contents for each part is as follows:

(1) For macroscale thermoelectric measurements, a high temperature Seebeck coefficient and electrical resistivity measurement system and a high temperature Hall effect measurement apparatus have been successfully designed, assembled and tested.

(2) For nanoscale thermoelectric measurements, preliminary work has been carried out on the localized measurement of thermal properties via the scanning thermal microscopy. Different modes of testing methodologies and calibration techniques are also introduced and discussed.

(3) For thermoelectric oxide synthesis and characterization, $Na_xCo_2O_4$ was chosen as a model material system. Different methods, including ball milling, electrospinning, and combustion synthesis methods, have been applied to engineer the microstructure and improve the thermoelectric properties of $Na_xCo_2O_4$.

These three parts are tightly connected. The thermoelectric properties of materials synthesized in Part 3 have been characterized by the measurement systems developed in Part 1. The measurement systems developed in Part 1 was designed to cover the special requirement of thermoelectric oxides, particularly high temperature measurement in oxidizing environment. The scanning thermal microscopy developed in Part 2 aimed to provide deeper physical insights of characterized material behaviors at the nanoscale.

The thesis has two major contributions. First, it provides detailed designs and procedures for both macroscale and nanoscale thermoelectric measurement. Measurement is as important as synthesis for materials research. However, as the instrumentation and measurement procedures became increasingly complicated, most researchers started to rely on commercial systems, which are usually treated as a black box to the operators. While there are some publications on instrumentation available in the literature, the designs are often overly complicated, lack of details, and without optimization. In this thesis, original parts and controls, which are designed and optimized repeatedly to solve the practical engineering challenges, are described in details. These designs may also have extended values for other measurement applications. In addition, novel measurement methodologies are also proposed for potential applications, for example the dynamic method for continuous Seebeck measurement at structure phase transition.

The second contribution is related to explore possible structure modifications of $Na_xCo_2O_4$ for optimization of thermoelectric performance. Most existing researches on $Na_xCo_2O_4$ have been focused on element doping and other composition modifications. Structure modifications of $Na_xCo_2O_4$, especially nanostructuring, have not been explored as extensively as other materials system such as Bi_2Te_3 and PbTe. The methods explored in this thesis can be applied to other thermoelectric oxides materials systems beyond $Na_xCo_2O_4$. For example, co-electrospinning method is applicable to most oxide materials, and texturing process is applicable to anisotropic systems similar as $Na_xCo_2O_4$.

Chapter 2 Development of High Temperature Seebeck Coefficient and Electrical Resistivity Measurement System

2.1 Introduction

Seebeck coefficient (S) and electrical resistivity (σ) are two main properties to determine the figure of merit (ZT) of a thermoelectric materials. With these two factors, another important index of thermoelectric performance, power factor (PF), can be calculated:

$$\mathrm{PF} = S^2\sigma \tag{2.1}$$

For many practical applications, where output power wattage is more concerned than energy conversion efficiency, power factor is more important than the figure of merit and is the main criterion for materials selection.

Since Seebeck coefficient and electrical resistivity are often not constants over a temperature range for thermoelectric materials, they are usually measured as a function of temperature. Similarly, ZT and power factor are also functions of temperature, and can be used to guide material selection for certain temperature range.

As discussed in Section 1.5.2, thermoelectric oxide is favored for high temperature applications over large temperature range, so measuring thermoelectric properties over a wider temperature range is needed for researches on thermoelectric oxides.

In this chapter, development of a high temperature Seebeck coefficient and electrical resistivity measurement system will be discussed, including detailed description of measurement principle, design of mechanical structures and electronic systems, measurement procedures and calibration processes. It is worth mentioning that, this system has been designed to incorporate the special

requirement for better characterization of thermoelectric oxides, unlike other high temperature testing system reported in the literature.

2.2 Theory and Methodology

2.2.1 Seebeck coefficient measurement

There are two main methods for measuring Seebeck coefficient: the integral method and differential method.

Integral method

In the integral method, the temperature of one end of tested sample is fixed at a temperature T_0. During the measurement process, temperature of the other end of the sample T varies, and the corresponding Seebeck voltage V generated between the two ends is measured and recorded [48]. Ideally, a continuous curve of V-T relationship can be obtained, and the relative Seebeck coefficient S between test sample and voltage probing wires at temperature T can be derived by measuring the derivative of the curve at T. Mathematically, it can be expressed as the following equation

$$S(T) = \frac{dV}{dT} \tag{2.2}$$

Noted that S here still contains a contribution of the testing leads.

Integral method always involves large temperature difference, and thus large Seebeck voltage signal. This property makes integral method insensitive to the small spurious emf noises generated in the measuring circuits [49]. The setup of integral method could be very simple, and only one heater is needed for temperature controlling at the hot end. The temperature of the cold end is held

constant, usually by connecting it with a large heat sink of copper. For samples that can be made into long wires or strips, integral method is a good choice.

The disadvantages of integral method are also obvious. It is very difficult to establish a large temperature difference for wide temperature range measurement with short and brittle samples, such as ceramics. The data analysis method is not well defined and lacks of standards, and calculating the derivative of a group of discrete data points requires special mathematical methods. Integral method is also insensitive to the abrupt change of Seebeck coefficient versus temperature, for example, sharp Seebeck coefficient change across phase transition point.

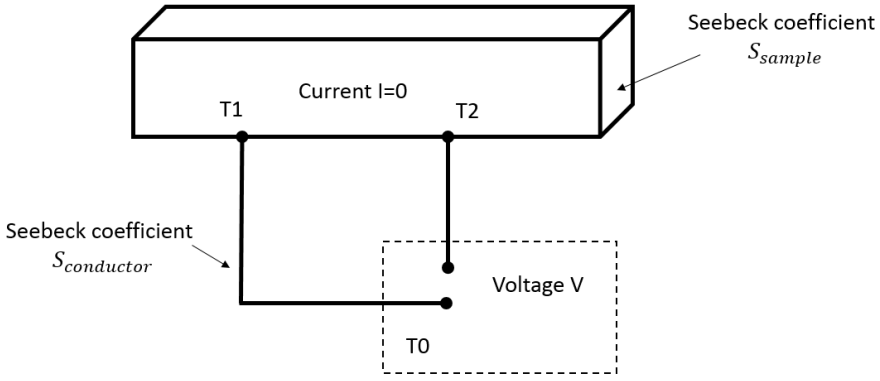

Figure 2-1 Configuration of Seebeck coefficient measurement by the differential method.

Differential method

In contrast to the integral method, differential method requires small temperature difference for Seebeck coefficient measurement. As shown in Figure 2-1, a small temperature gradient $\Delta T = T1 - T2$ is applied across the sample. At the spots of $T1$ and $T2$, two voltage measurement leads are connected with sample, and the other ends of the testing leads are located at a same temperature $T0$. The measured voltage V between two ends of testing leads can be expressed as:

$$V = -\int_{T0}^{T1} S_{conductor} dT - \int_{T1}^{T2} S_{sample} dT - \int_{T2}^{T0} S_{conductor} dT \quad (2.3)$$

$$= -\int_{T1}^{T2} (S_{sample} - S_{conductor}) dT$$

Noted that, $S_{conductor}$ and S_{sample} are the Seebeck coefficient of testing leads and sample, both of which are functions of temperature. Another detail that needs attention is that the measurement is carried out with the sample in an open circuit, with the current passing through the sample $I = 0$.

The assumption of differential method is that, when ΔT is small, the Seebeck coefficient can be considered as a constant representing its value at the average temperature, $T_{avg} = (T1 + T2)/2$. So the equation (2.3) be further reduce into:

$$V = -\int_{T_{avg}-\frac{\Delta T}{2}}^{T_{avg}+\frac{\Delta T}{2}} [S_{sample}(T_{avg}) - S_{conductor}(T_{avg})] dT \quad (2.4)$$

$$= -[S_{sample}(T_{avg}) - S_{conductor}(T_{avg})]\Delta T$$

The Seebeck coefficient of tested sample at temperature T_{avg} can then be calculated:

$$S_{sample}(T_{avg}) = S_{conductor}(T_{avg}) + (-\frac{V}{\Delta T}) \quad (2.5)$$

Since the temperature difference ΔT is required to be very small, normally less than 5℃, the measured voltage signal will also be small and in the microvolts range. In practical measurements, a constant voltage offset generated by the circuit, usually large than 100 μV, is large enough to distort the result. To eliminate this effect, a group of different temperature difference ΔT and the corresponding Seebeck voltage V are measured and plot as a $V - \Delta T$ curve. The slope of the curve

reveals the true $V/\Delta T$ value independent of the constant voltage offset, and the better linearity of the data points, the more reliable of the result.

Compared to integral method, the differential method requires more advanced hardware for small voltage signal measurement and better temperature control. Normally a voltmeter with resolution better than 0.1 μV is used to monitor the Seebeck voltage. At least two separately controlled heaters are used to ensure a stable average temperature T_{avg}, and a stable and variable temperature difference ΔT.

Differential method is much more popular than integral method, because it is more suitable for small and brittle samples, and for measurement at high temperature or over wide temperature range. And the data analysis based on slope ensures the accuracy and reliability of the measured Seebeck coefficient.

Thermoelectric oxides are usually fabricated as small pellets and most of thermoelectric oxides are developed for high temperature applications. So in this work, differential method is chosen as the method to measure the Seebeck coefficient.

2.2.2 Electrical resistivity measurement

Two methods are typically available for electrical resistivity measurement: four terminal method and Van der Pauw method [50]. Both methods can eliminate the error from electrical contact and wire resistance, though the sample requirement of these two methods are quite different. Four terminal method requires a long bar shape sample, while Van der Pauw requires a thin disc sample.

In this work, four terminal method is chosen to measure the electrical resistivity, because its required sample geometry and measurement setup, as shown in Figure 2-2, are compatible with differential method for Seebeck coefficient measurement.

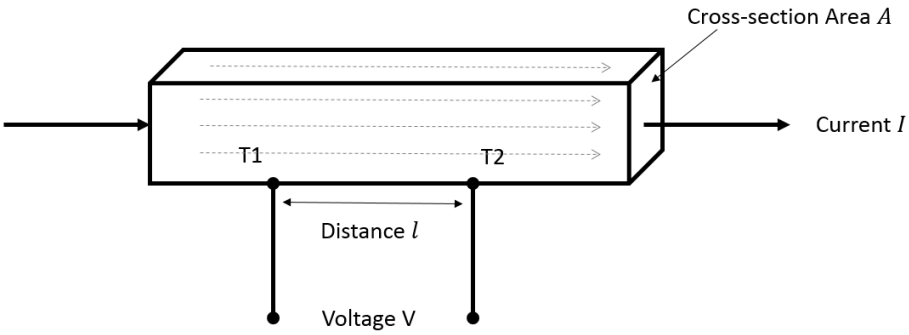

Figure 2-2 Configuration of electrical resistivity measurement.

To measure the electrical resistivity, both the environment temperature and temperature gradient are kept stable, and a current passes through the conductor from a constant current source. By sweeping a set of different current value I and measuring its corresponding voltage V between the two points, a set of $I-V$ data points is obtained. Using the least square method, the slope of the $I-V$ curve can be calculated, which is the resistance of sample portion between the two probes (R).

$$R = \frac{dV}{dI} \tag{2.6}$$

The resistivity ρ can then be calculated through the cross-section area A and probe distance l:

$$\rho = \frac{RA}{l} \tag{2.7}$$

Note that during the electrical resistivity measurement, the temperature gradient doesn't need to be perfectly zero. But if there is a thermal gradient presented, it has to be sufficiently stable for a reliable $I-V$ curve measurement.

2.3 Scientific and Engineering Challenges

The accurate measurement of the Seebeck coefficient is simple in concept but complex in practice. Although the principle of measurement is well established and a great deal of works [48, 51] have been done in the past several decades, there are still several experimental issues remain unsolved. Two of the major problems are: (1) establishment of the absolute Seebeck coefficient scale; and (2) difficulty in measuring the temperature and Seebeck voltage at exactly the same point.

2.3.1 Absolute Seebeck scale & standard sample

As mentioned earlier, Seebeck Voltage can only be measurement in pairs of two different materials. For example, in Equation (2.5), in order to get the absolute Seebeck coefficient of the sample, we have to know the absolute Seebeck coefficient value of test leads at the same temperature. In fact we just need one reference material that we can obtain its absolute Seebeck coefficient, and then we can measure all samples of interest relative to this reference material.

But how can we find a reference material with known absolute Seebeck coefficient? Fortunately, at low temperature, such materials exist. Superconductors have zero Seebeck coefficient at Meissner state ($T < T_c$) [52], and by using superconductors, the absolute Seebeck coefficient scale was able to be measured up to about 120K [52].

Another technique, Thomson-coefficient-integration method, is then required to extend the upper limit to a higher temperature (>120K) [48]. Seebeck coefficient of individual materials can be calculated by measuring the Thomson coefficient μ, which is also a function of temperature, and using the relation:

$$S(T) = \int_0^T \frac{\mu}{T} dT \tag{2.8}$$

This technique established the absolute scales of thermoelectricity for common reference materials such as pure Copper and Platinum. However, due to the difficulty of these measurements, there is no systematic experiment over a wide temperature range and very few experiments have been reported. All the current reference data is established based on the literature more than 30 years ago by summarizing the experiment results that was done even earlier. Even now, it is still difficult to find the absolute Seebeck coefficient data of common materials such as Chromel over a wide temperature range.

The lack of completeness for absolute Seebeck scale also causes another problem - the lack of standard samples. To fully calibrate a measurement system, more than one standard samples should be used to verify the accuracy of the measurements. The standard samples should be very stable and be able to cover the measurement range of the system. For a high temperature system, such standard samples is very difficult to find and, especially for a system that performs measurement at an oxidizing environment.

In this work, copper has been used as one of the standard sample for the calibration of Seebeck measurements.

2.3.2 Simultaneously measuring temperature and Seebeck voltage at the same point

Ideally, the temperature should be measured at the exactly the same point where the Seebeck voltage is probed, as shown in Figure 2-1. But, in practice, this requirement is very difficult to fulfill, and the temperature measurement spots and electrical contacts are usually separated and a discrepancy of distance larger than the diameter of thermocouple wire exists, as shown in Figure 2-3(A). In Figure 2-3(B), Wood and his colleagues propose a cross wire method using

thermocouple wires with very thin diameter to reduce this error [53, 54]. Even though, the actually thermal and electrical contacts are still one wire diameter apart. There is no direct comparison data either showing that the error will be reduced using this setup compare to the conventional beaded thermocouple junction. This problem become more serious when measuring a sample of high thermal conductivity, such as copper, or in an environment with rapid temperature changing, such as dynamic measurement environment that will be discussed later, because it could take a longer time (over seconds or minutes) for the heat propagation at the junction.

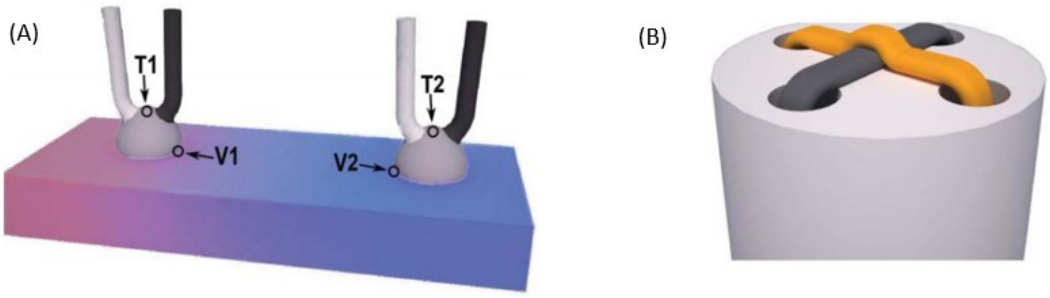

Figure 2-3 Thermocouple probes used for Seebeck measurement, (A) thermocouple probes with a beaded junction, and (B) crossed-wire thermocouple probe [53].

Another technique that could solve this problem, has been used for measuring thermal diffusivity by flash method [55]. In this method, the two branches of thermocouple are not directly connected and separated by a small distance. Instead, they are connected electrically through the sample, as shown in Figure 2-4. This ensures the measured temperature is same as the surface temperature of sample and also a faster response speed that is typically less than a milli-second. However, it is evident that this method is limited to materials with low electrical resistivity, doubles the number of actual contact points, and requires more complicated mechanical design to ensure the contacts

reliability. To our knowledge, there is no reported Seebeck measurement system that has been built using this method.

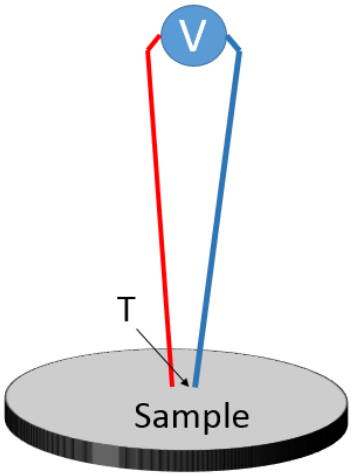

Figure 2-4 Fast response thermocouple probe for thermal diffusivity measurement via flash method.

In this work, conventional beaded thermocouple junction is used to make thermal and electrical contact with the tested sample. One of the major reasons for this choice is that the beaded contacts have better corrosive resistance against samples (such as $Na_xCo_2O_4$) at high temperature.

2.3.3 High temperature thermal and electrical contact

It is very important to keep good and reliable contact during the measurement. At high temperatures, few materials are available for a reliable probing setup. There are many designs for high temperature measurement systems [48, 51, 53], but most of designs are complicated and difficult to manufacture and maintain.

In this work, a robust high temperature test fixture is designed for this measurement system using off-the-shelf parts.

2.4 Design of Mechanical Structures and Electronic Controls

The measurement system, as shown in Figure 2-5, is composed of three main parts: high temperature dual heater furnace, high temperature sample test fixtures, and environment controlled chamber.

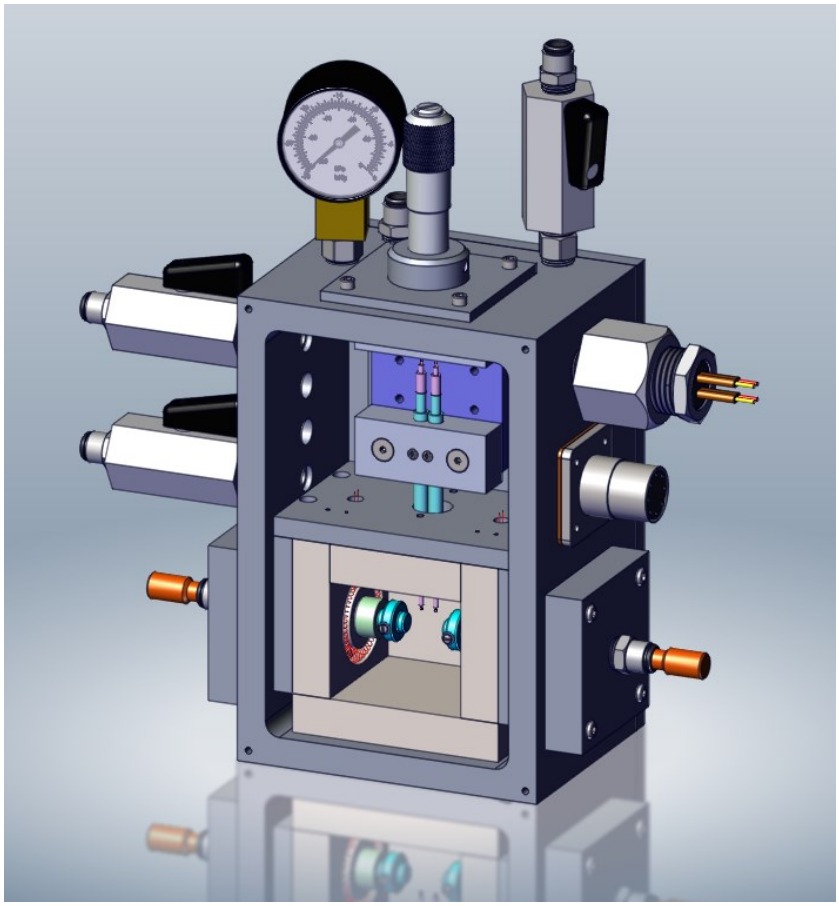

Figure 2-5 Overview of the mechanical structure design of the high temperature Seebeck coefficient and electrical resistivity (HT-S&R) measurement system

2.4.1 High temperature dual heater furnace

The furnace is composed of two identical nickel-chrome heaters aligned in parallel, as showing in Figure 2-6. Low density alumina ceramic fiber board is used as the thermal insulation layer to

minimize the heat loss out of the furnace. The heaters are able to raise the temperature of the furnace up to 1200°C in an inert environment and 900°C in an oxidizing environment. In addition, the heaters are powered separately using two programmable DC power supplies. By toggling the heating power difference between the two heaters, a horizontal thermal gradient can be easily and quickly established and stabilized in side this mini furnace.

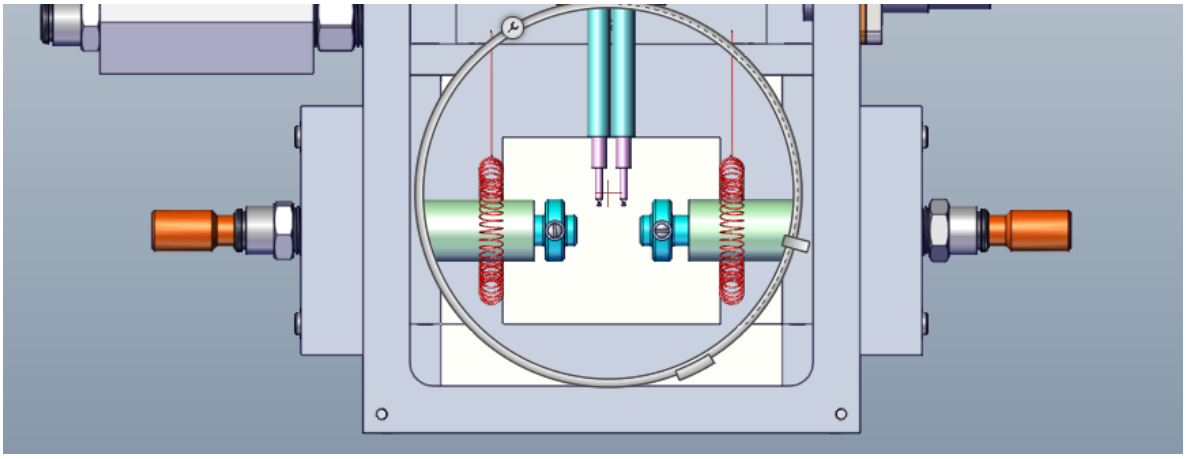

Figure 2-6 Mechanical design of the dual heater furnace

The thermocouples in contact with sample for Seebeck coefficient measurement are also used as the temperature sensor for controlling the furnace temperature. Two independent PID feed-back temperature controls have been implemented through the software and used for controlling both the average temperature and temperature difference of the two thermocouples.

Each DC power supply of the heaters has a maximum output power of 500W, and an output voltage resolution of 1mV. Normally it needs 30V for each heater to heat the furnace to 500°C, so theoretically the pair of power supplies are capable of controlling a furnace temperature with 0.02°C accuracy without the help of PID controller.

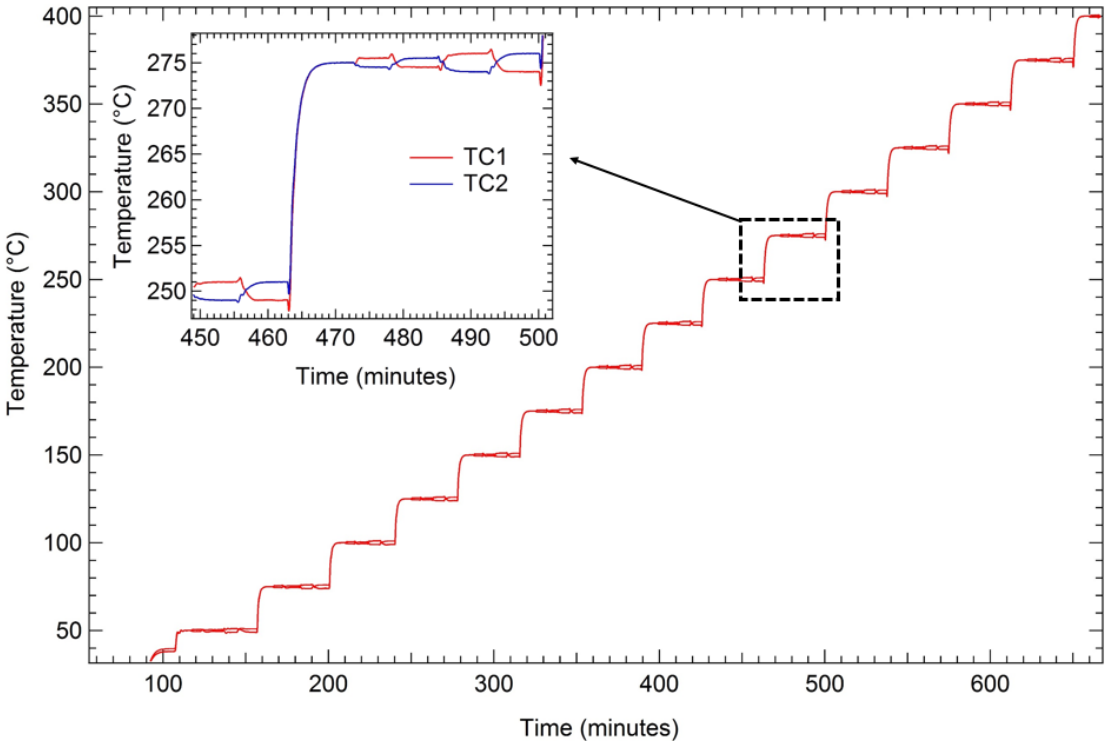

Figure 2-7 Temperature as a function of time during the Seebeck & resistivity measurement.

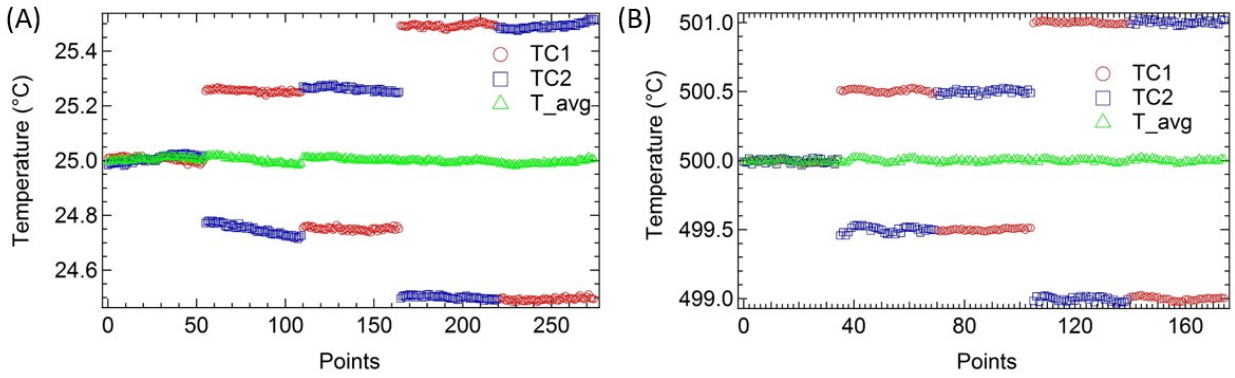

Figure 2-8 Temperature control with a stability tolerance of 0.1°C; (A) measurement at 25°C with temperature differences of 0, ±0.5 and ±1°C; (B) measurement at 500°C with temperature differences of 0, ±1 and ±2°C.

As shown in Figure 2-7 and 2-8, with the dual PID feed-back controlled heaters and precision DC power supply, preset average temperature and temperature difference targets can be achieved quickly, precisely and also with little oscillation.

2.4.2 High temperature thermocouple probes and test fixtures

The test fixture, shown below in Figure 2-9, is designed to ensure a reliable thermal and electrical contact for the measurements.

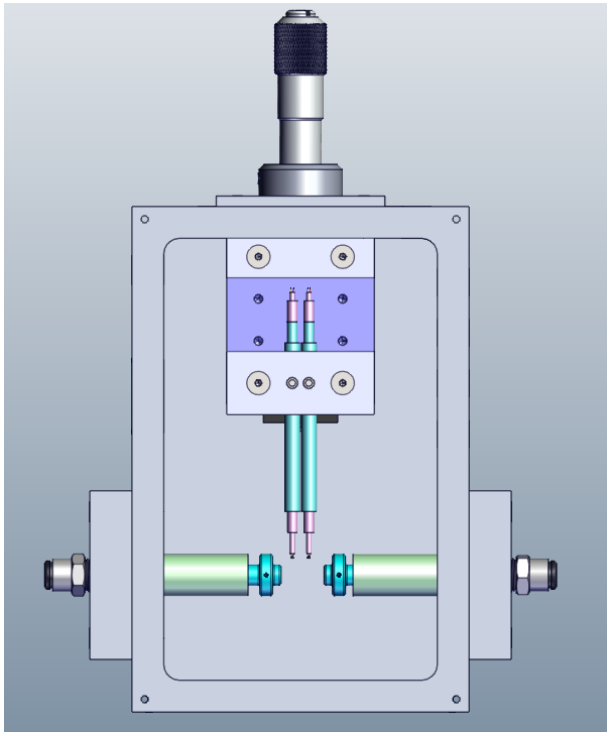

Figure 2-9 Test fixture design of the HT-S&R system.

Current electrodes

The sample is held horizontally by two high temperature electrodes (see Figure 2-10), which are made of Inconel HX, a high temperature nickel alloy, and have excellent oxidation resistance in temperatures up to 1100°C. High temperature nickel-chrome wires are used as current leads, with one end fixed on the high temperature electrodes and the other end connected to the Keithley 224 source meter. Set screws are used on each side to position the current electrode for sample clamping. Ideal samples should be in rectangular bar shape with a length between 6 ~ 15 mm, and

also a width or thickness between 1 to 3 mm. Two springs are used to ensure the reliability of sample clamping during a widely temperature range measurement. Ceramic tubes and spacers are used to guild the movement of electrodes and insulate the current leads from aluminum chamber.

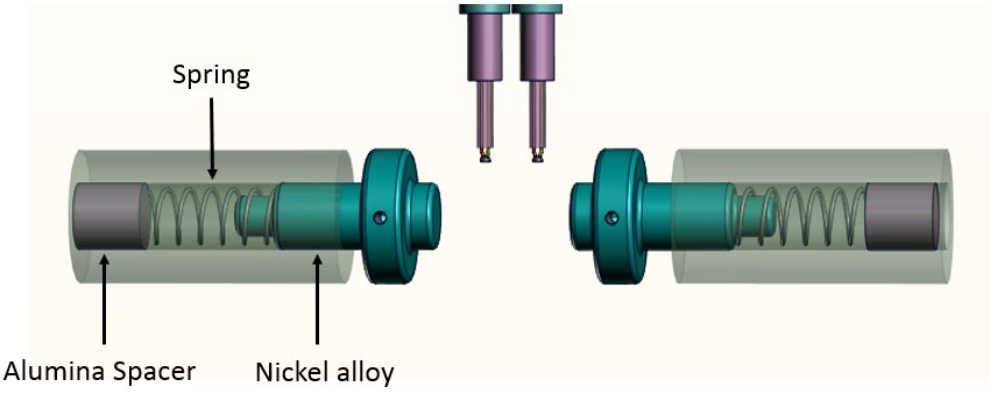

Figure 2-10 Close-up view of the current electrodes and the sample clamping mechanism.

Thermocouple probes

Figure 2-11 shows the design of thermocouple probes for temperature and voltage measurement. The position of the probe is controlled through a micrometer head and a linear slide. The probe spacing is controlled by a simple custom designed aluminum block, and can be switched any time when a different probe spacing is needed. Thermocouple probes are fixed in the aluminum block using set screws.

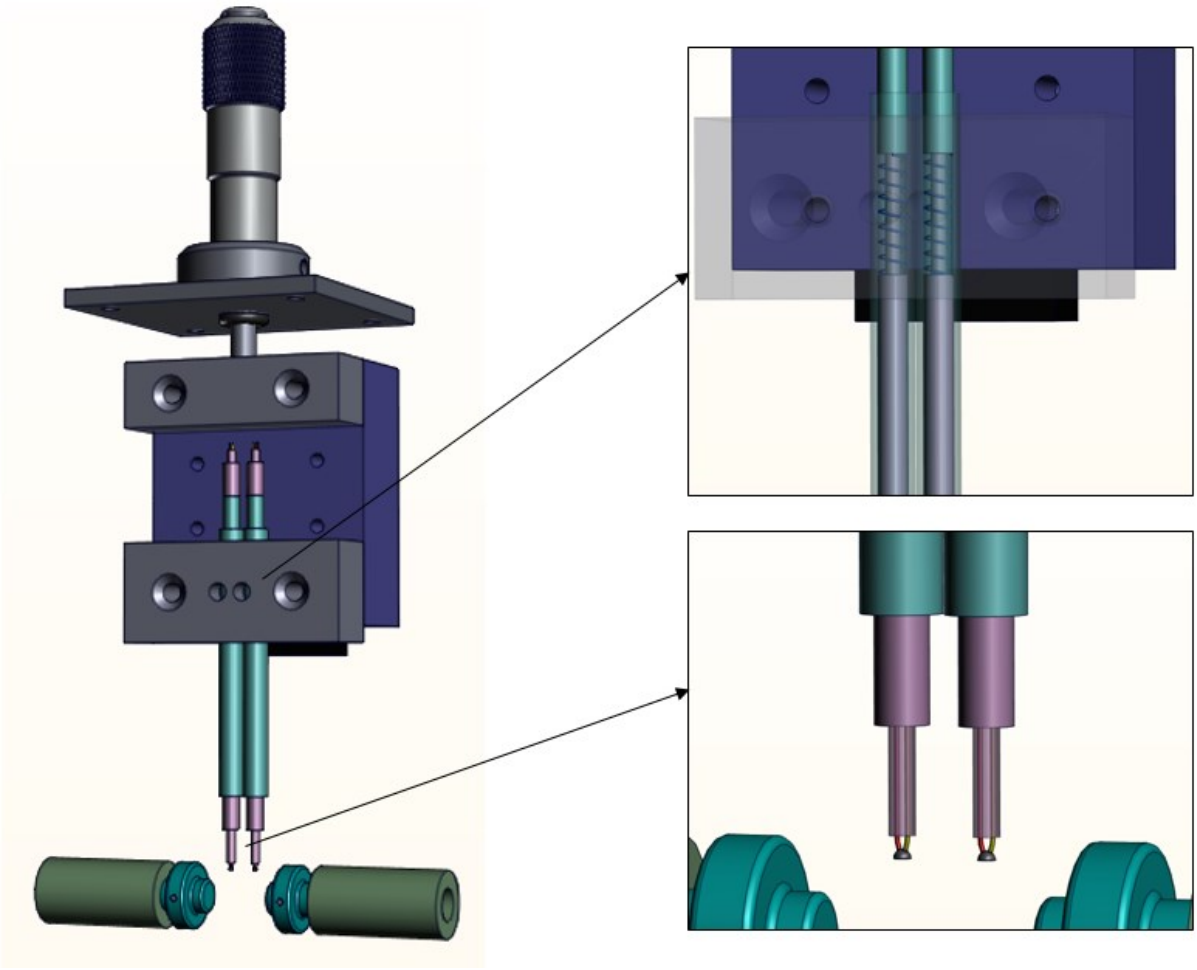

Figure 2-11 Overview of the thermocouple probes positioning mechanism.

The probe is made from three different types of alumina ceramic tubes, as shown in Figure 2-12. All the ceramic parts are available off-the-shelf, so there is no need for extra ceramic machining. A spring is used for each probe to ensure a reliable pressure contact with tested samples. When the probe is engaged with the sample, the inner probe moves up compressing the spring to the top of outer shell. There is also a lower limit block at the top of the probe. This block has two functions: (1) an index for monitoring how much the pressure has been applied to the sample; (2) a limit block that prevents the probe from falling down when the pressure is fully released.

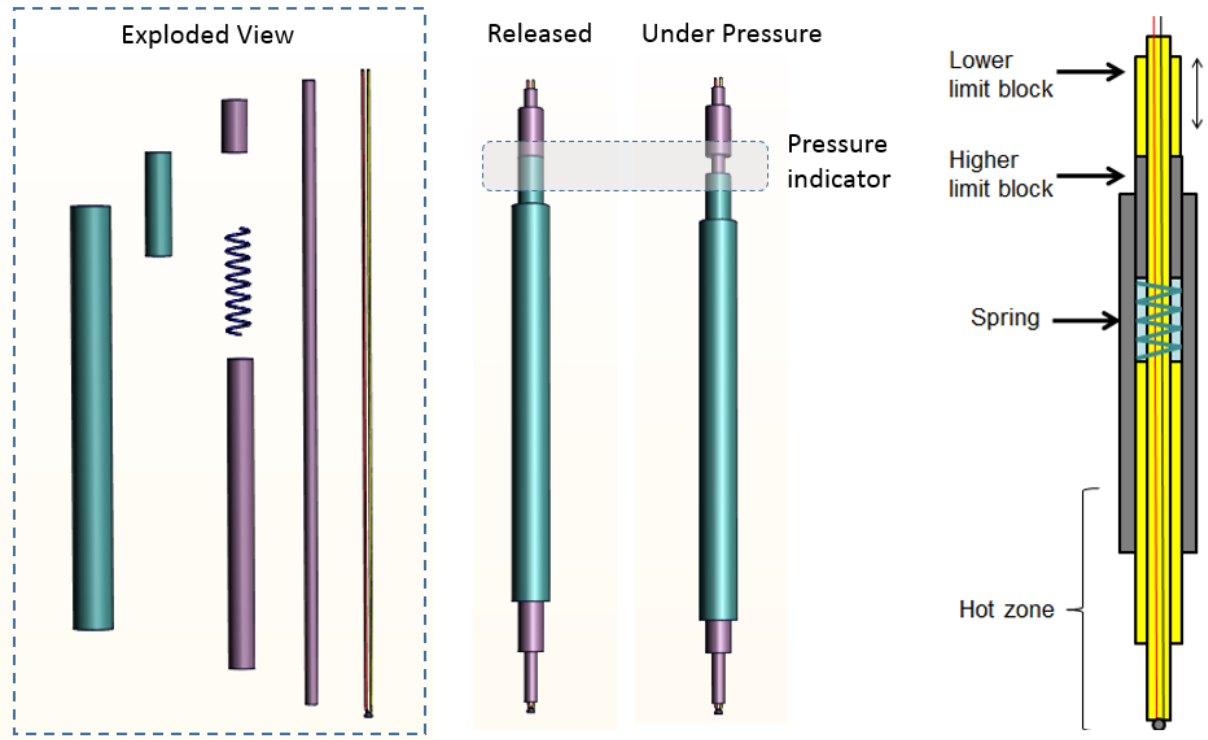

Figure 2-12 Design of the high temperature thermocouple probe.

The most unique part of this design is that the spring is placed inside the thermocouple probe. This build-in spring design not only reduces the design complexity and cost of entire positioning system, but also makes the probes more robust and durable. Figure 2-13 shows a design of thermocouple probe of a commercial system ZEM3, the replacement of each pair of R type thermocouple probes costs more than $2000.The thermocouple probe of ZEM3 is about 300mm long with a diameter of only about 1mm. The long and thin alumina tube, just as weak as spaghetti, can be broken very easily during operation. Compared to the ZEM3 design, the thermocouple probe in this system is very robust, because it has an outer diameter about 4mm and only 80 mm in length.

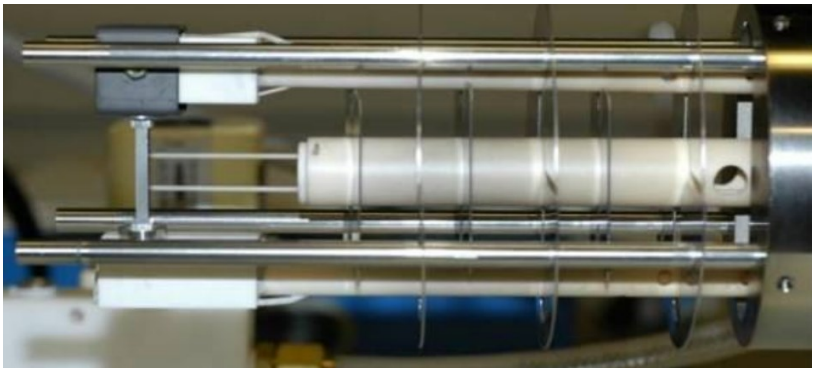

Figure 2-13 Thermocouple probe design for a commercial system (ZEM3 from ULVAC technologies, Inc.).

2.4.3 Environment controlled chamber

This measurement system is equipped with a water cooled aluminum vacuum chamber that allows three different testing environments: vacuum, low pressure inert gas, and air.

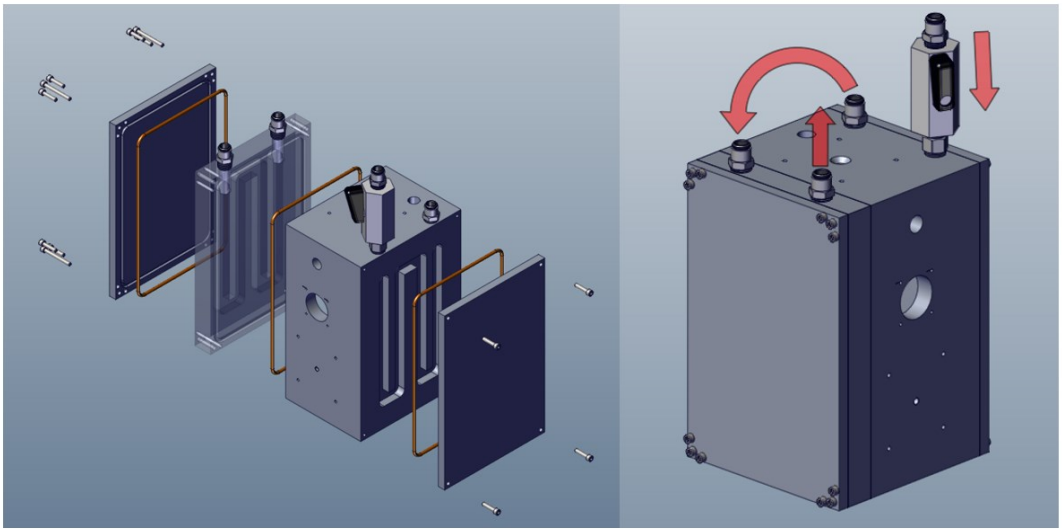

Figure 2-14 Design of the water cooling system for the main testing chamber.

Water cooling

Figure 2-14 shows the water cooling system design in the front and back. The inlet and outlet are connected to a refrigerated circulator with a temperature setting at 17°C. A minimum water flow

rate of 2L/ min will keep the outer chamber cold (less than 30°C) even after the furnace has been operating at 900°C for hours.

Vacuum chamber

Figure 2-15 shows the design of the main chamber. On the top, there is a micrometer head feedthrough for positioning of thermocouple probe and a vacuum pressure meter monitoring the air pressure. On the left, there are inlet and outlet ball valves for purging and evacuating the chamber. On the right, there are electrical feedthrough for the thermocouples, current source and heaters. On the bottom part of two sides, two quick-disconnect tube fitting enable easy access to the set screws for sample fixing and also a quick seal option for vacuum.

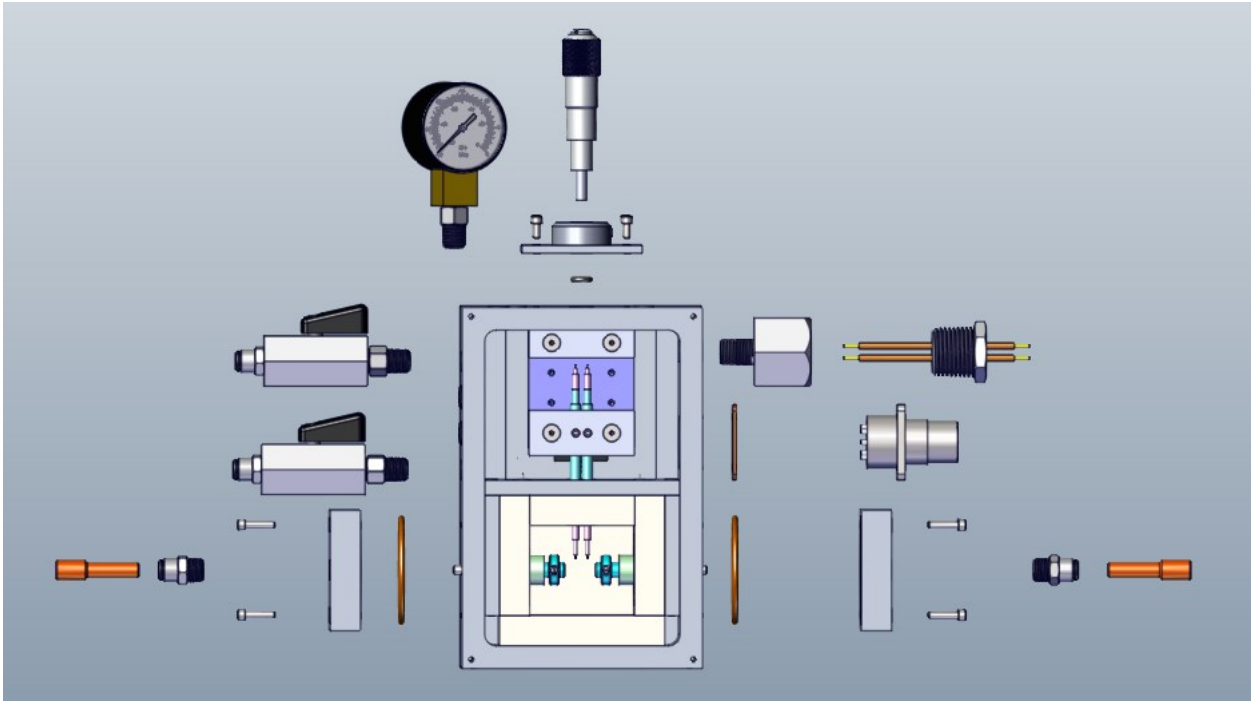

Figure 2-15 Design of the vacuum system for the main testing chamber.

2.4.4 Instrumentation and measurements

Table 2-1 lists the voltage meters, current source and power supply used for this system.

Table 2-1 Instrumentation list for Seebeck & resistivity measurement system

Model	Function	Quantity
Keithley 2000 DMM	Measure temperature	2
Keithley 181 Nanovoltmeter	Measure Seebeck Voltage	1
Keithley 224 Source Meter	Current Source	1
Array 3663A DC Power Supply	Heater Power	2

The electrical connection diagram is shown in Figure 2-16. Voltages of two thermocouple probes are measured by two Keithley 2000 digital multimeters (DMM), and Keithley 181 nanovoltmeter is used to measure the Seebeck voltage signal. Keithley 224 source meter is used as the constant current source for electrical resistivity measurement. All the meters and power supplies are remotely controlled in LabVIEW through GPIB and RS232 connections.

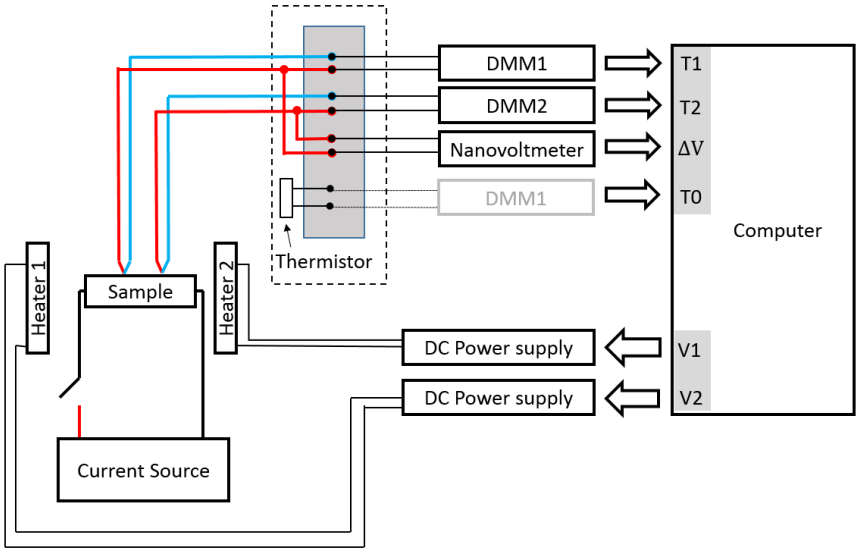

Figure 2-16 Schematic electrical diagram of the Seebeck & resistivity measurement system (grayed DMM1 denotes a temporarily channel of DMM1 for occasional usage).

Temperatures are converted from the measured voltages using polynomials from thermocouple calibration standards (ASTM E230). Cold junction compensation method (ASTM E230) and measured cold junction temperature, usually room temperature, are used to correct the measured thermocouple voltage. The cold junction temperature is calibrated by a precision thermistor (Omega Engineering 44005), which is measured by a Keithley 2000 DMM at the beginning of the experiment.

2.5 Development of Measurement Procedures

Three different procedures can be used to measure the Seebeck coefficient without making any changes of hardware: steady-state method, quasi-steady-state method, and dynamic method.

Electrical resistivity can be simultaneously obtained using steady state method and quasi-steady-state method. Dynamic method is developed for continuous Seebeck coefficient measurement only.

2.5.1 Steady-state method

Steady-state Method is the most popular method because of its simplicity and accuracy [48, 51]. Figure 2-17 shows the measurement procedures of steady-state method. For each Seebeck coefficient measurement at a single point of temperature T_i, it requires several different temperature difference $\mathrm{d}T_j$ established between the two contacts. The Seebeck voltage and $I-V$ measurements start when both the average temperature T_i and temperature difference $\mathrm{d}T_j$ are stable.

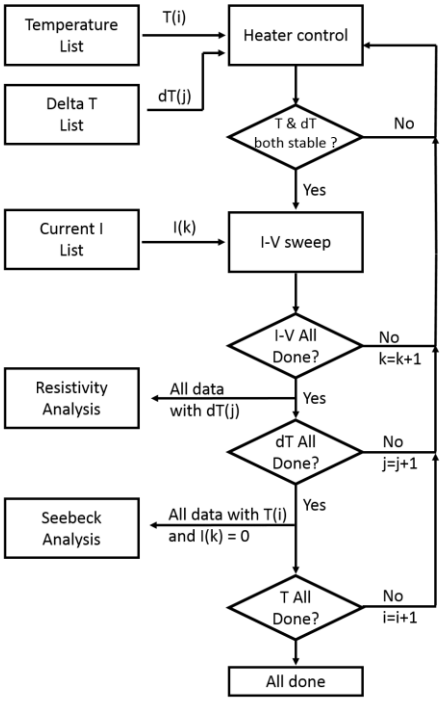

Figure 2-17 Flow diagram of the steady-state measurement procedure.

Figure 2-18 shows the Seebeck coefficient measurement raw data of copper at 50 °C using steady state method. Chromel wire, the positive leg of K type thermocouple, is used as the Seebeck voltage probe. Seebeck voltage data at five different temperature differences have been recorded. There are five points at each temperature difference. To calculate the Seebeck coefficient of the copper, the 25 data points are plot in Figure 2-18 (B) and least square method is used to perform the linear fit to obtain the slope. The slope value is the relative Seebeck coefficient of copper versus Chromel at 50 °C, so the Seebeck coefficient of copper can be calculated if Seebeck coefficient of Chromel is already known. Sometimes this process is reversed, since copper is one of few materials have complete standard absolute Seebeck coefficient, by measuring against copper the absolute Seebeck coefficient of Chromel can be calibrated.

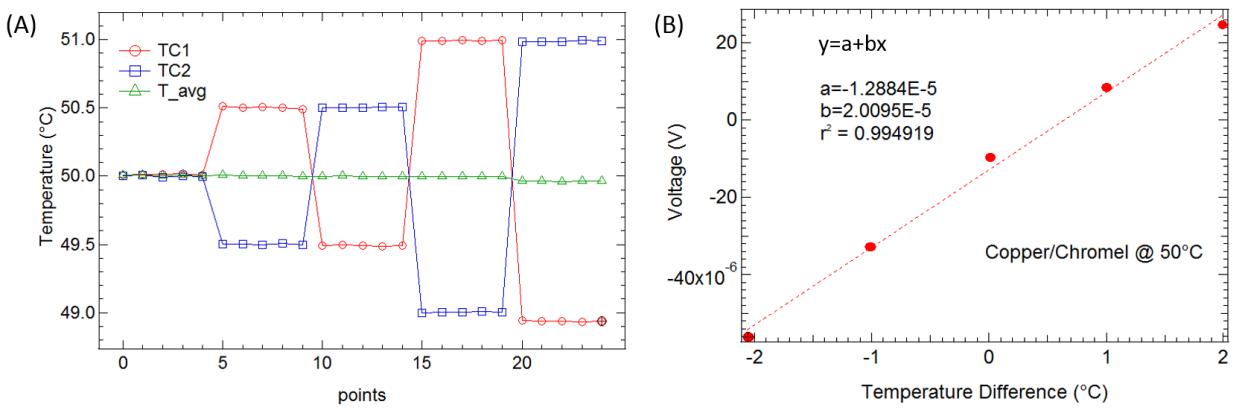

Figure 2-18 Raw data analysis of steady-state method measurements.

2.5.2 Quasi-steady-sState method

Quasi-steady-state method is developed to reduce the time of Seebeck coefficient measurements [48]. Unlike steady-state method, there is no need to wait for temperature stabilization at temperature difference level. The measurement procedure is shown in Figure 2-19. After the average temperature stabilization, $I-V$ measurement is performed first when temperature difference is unchanged. Then the software starts to toggle the dual heater offset setting, which ends up with a slow changing rate of temperature difference dT while keeping the average temperature T unchanged. During the dT ramping process, both dT and Seebeck voltage are recorded for linear regression analysis.

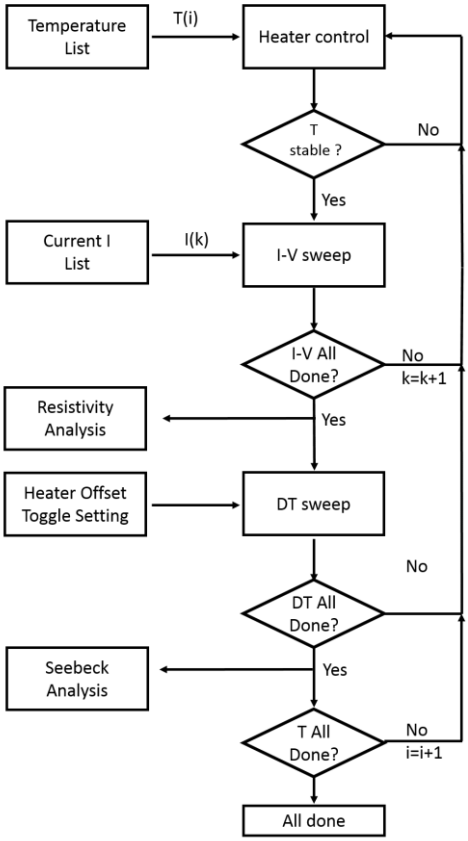

Figure 2-19 Flow diagram of the quasi-steady-state measurement procedure.

Compare to other reported systems in literature [48, 53], this work has better control on average temperature during the temperature difference ramping, and this advantage become more important when measuring a temperature sensitive phase-changing materials or with a large temperature difference. In Figure 2-20 (A), each point was taken every 10 seconds, so the changing rate of the temperature difference is about 0.45°C/min. From the plot, it can be seen that the average temperature is kept stable at target temperature of 50°C. Similar as steady-state method, the Seebeck coefficient is obtained by fitting the data point using least square method, and the data in Figure 2-20(B) show very good linearity.

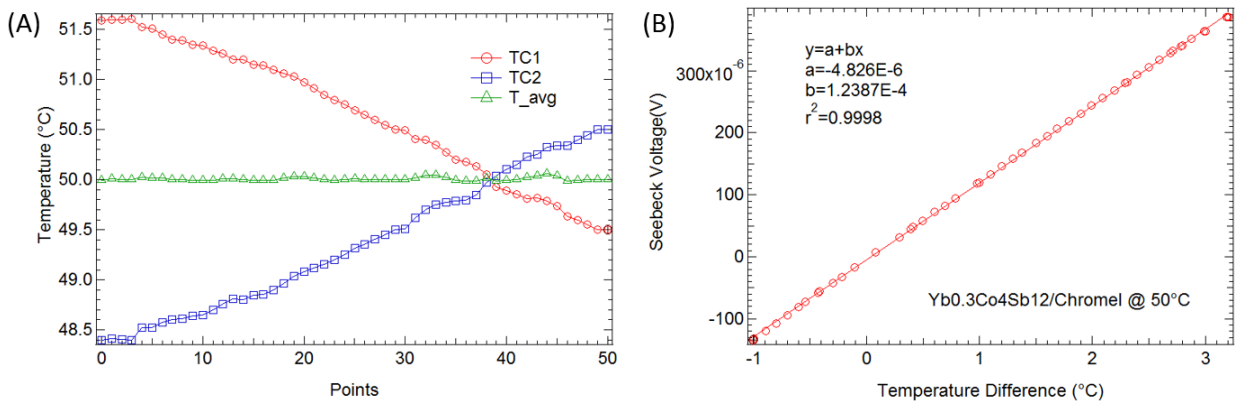

Figure 2-20 Raw data analysis of the quasi steady-state method measurement

2.5.3 Dynamic method

Although quasi-steady-state method is able to save much of measurement time without compromising the accuracy, it still needs a thermal stabilization process for each temperature point of the measurement. Therefore, the quasi-steady-state method can only measure Seebeck coefficient of discrete temperature points.

Review of the state-of-the-art in dynamic measurement

Dynamic method is developed to collect all the raw data continuously during temperature ramping without establishing any long term thermal stabilization. However, it does not mean the dynamic method should be faster than steady state method in any measurement situations. For example, if only 4 data points are needed between 50 and 200 °C, a steady-state method can finish the measurement in 4 hours, and the quasi-steady-state method can finish within 2 hours. For dynamic method if the average temperature ramping rate is chosen as 0.5°C/min, the measurement will take 5 hours. Instead of only 4 data points, Seebeck coefficient at all the temperatures in the sweep range can be derived from the raw data. The goal of dynamic method is to achieve a high time

efficiency (total data points needed / total time) and data resolution at temperature scale simultaneously.

AC methods involving frequency dependent data collection using lock-in amplifiers have been developed in 70s [56]. In most of these reports, light pulses are utilized to create small periodic temperature gradient. The temperature difference at the two contacts is not periodic, and large thermal drift could contribute to the generated Seebeck voltage. For example, in Figure 2-21, the light power is modulated at frequency f, and this causes oscillations of both ΔT and ΔV, even though the magnitude of the oscillation is too small to be directly observed in DC data collection. Using lock-in amplifier the signal at frequency f can be extracted and used to calculate Seebeck coefficient.

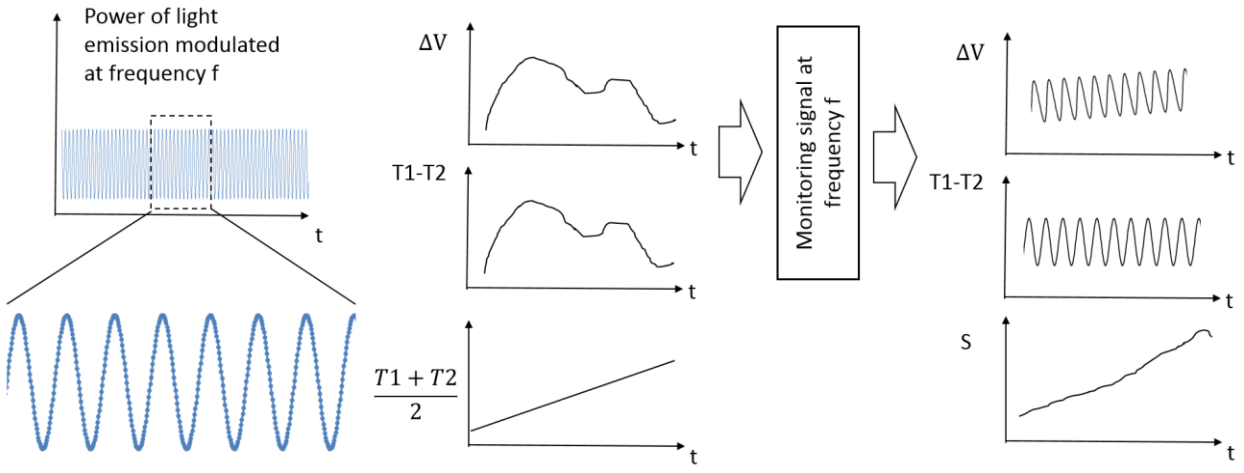

Figure 2-21 Schematic of the data analysis procedure for AC dynamic method.

The limitation and practical challenges come from the thermocouple measurement, which could be non-linear with temperature, and most time could not represent the real time temperature at the sample due to the contact issue discussed in Section 2.3.2. In addition, the light pulse can also involve other effects such as photo-thermoelectric effect for lightly-doped semiconductors. Period thermal gradient has also been carried out using parallel resistive heaters [57, 58], but because the

control accuracy and the slow thermal conduction speed, data collection of lock-in amplifier can be problematic when a stable oscillation over temperature and time is impossible. A recent work on DC dynamic method using large temperature difference has been reported [59]. The measurement could be very fast and continuous, but the methodology is oversimplified: the offset voltage has not been taken care of, and the large temperature difference limits the resolution of Seebeck coefficient at temperature scale.

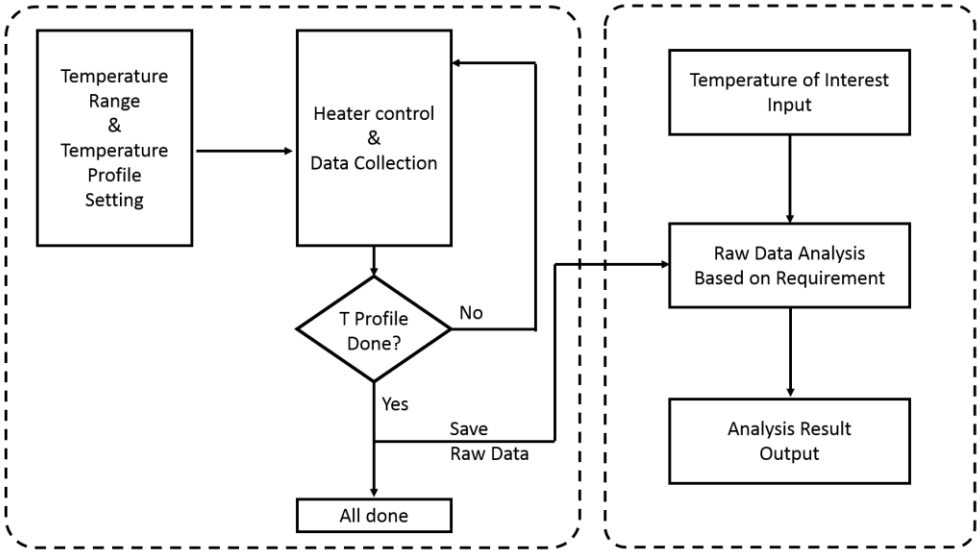

Figure 2-22 Flow diagram of the DC dynamic measurement procedure.

DC dynamic method

In this work, a new strategy of dynamic method is proposed using DC measurement techniques. The measurement procedure flow diagram is developed in Figure 2-22. Compared to steady-state and quasi-steady-state methods, there is no requirements for temperature stabilization. The controller controls the furnace temperature and thermal gradient according to the preset temperature profile. During the measurement, $T1, T2, \Delta V$ are collected simultaneously. After all raw data is collected, they will be analyzed to extract the Seebeck coefficient at any temperature of interest in the measurement range.

In this method, the most important and unique design is the temperature profile, which contains an oscillating temperature difference and a ramping average temperature. The ideal temperature profile is showing in Figure 2-23, where T_{avg} and ΔT are oscillating at different frequency, and T_{avg} is oscillating at a slower rate than ΔT, and also ramping up with the time. By choosing a temperature of interest and the tolerance of error, a band can be generated to pick the useful data for next step analysis, as shown in Figure 2-23(A). In Figure 2-23(B), the data with an average temperature around T_{avg} is picked out, and ΔT of those point is variable independently from T_{avg} due to the nonsynchronous change between ΔT and T_{avg}. After this step, the Seebck coefficient can be calculated similarly as in steady-state method.

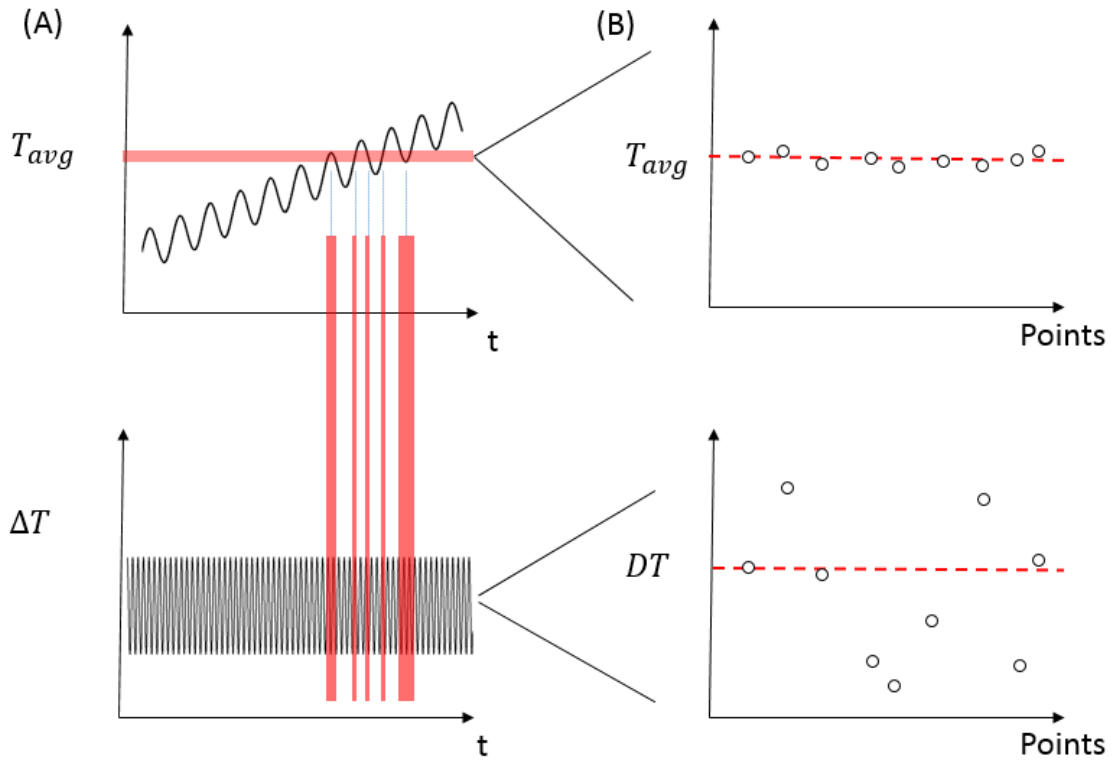

Figure 2-23 Schematic of data analysis for the proposed DC dynamic method

It is worth mentioning that, T_{avg} actually does not need to be oscillated. As long as T_{avg} varies much slower than ΔT, it can be viewed that ΔT varies while T_{avg} stays unchanged, and then the dynamic method is actually the same as a quasi-steady-state measurement.

Challenges

The main challenges come from two aspects.

First is the thermal contact as mentioned before in Section 2.3.2. Any lag in temperature sensing could distort the result from the true value.

Second is thermal drift of the circuit. Noted in Figure 2-23(A), those picked data are somehow distributed over time. It is quite possible that a large thermal drift arise during the experiment and totally distort the final result. Considering this situation, a temperature profile with smooth T_{avg} ramping path (without oscillation) could be less affected by this problem.

Implementation

The heater output is composed of three parts: a low frequency term $V_{f1}(t)$ for average temperature oscillation, a high frequency term $V_{f2}(t+\phi)$ for ΔT oscillation and a linear increasing term $V_0(t)$ for average temperature ramping. Phase angle ϕ is used to create a phase difference, usually a difference of π, between two heaters.

$$V_{heater1}(t) = V_{f1}(t) + V_{f2}(t+\phi) + V_0(t) \tag{2.9}$$

$$V_{heater2}(t) = V_{f1}(t) + V_{f2}(t-\phi) + V_0(t)$$

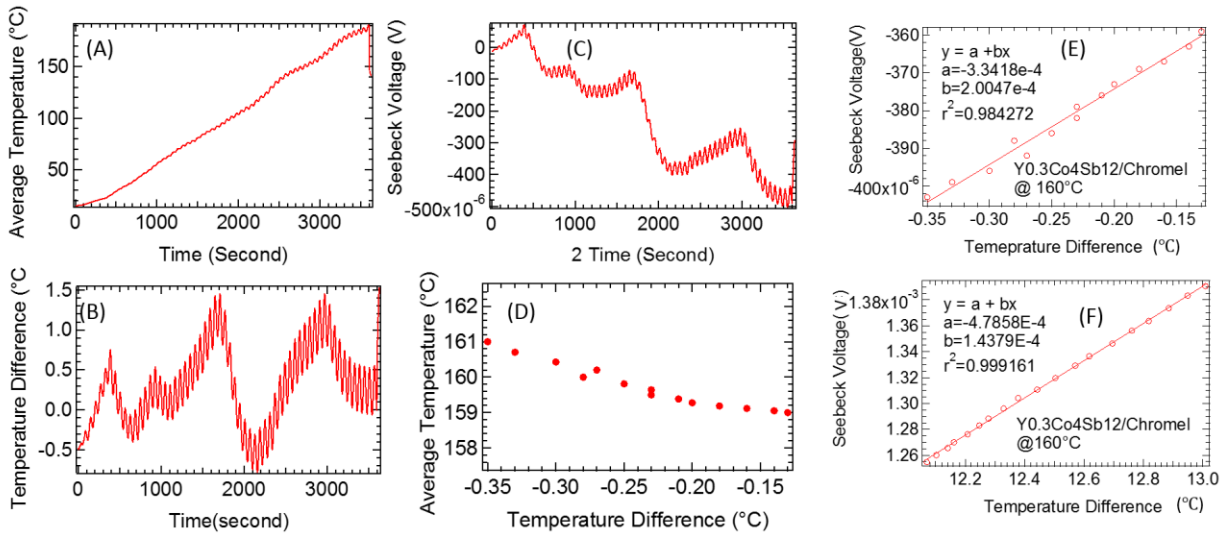

Figure 2-24 Seebeck coefficient measurement data of $Y_{0.3}Co_4Sb_{12}$ using dynamic method; (A) average temperature; (B) temperature difference; (C) Seebeck voltage; (D) data points for Seebeck coefficient analysis at 160℃; (E) analysis of Seebeck coefficient using data point from (D); (F) an another analysis at same temperature using a large temperature difference.

As shown in Figure 2-24 (A) and (C), ΔT is oscillating while T_{avg} is slowly increasing with temperature. From Figure 2-24 (C), the Seebeck voltage is oscillating with ΔT, but obviously not in a proportional manner over in a long time scale due to thermal drifting or thermal contact problems. Data points were picked around 160℃ with a tolerance of ± 1℃. The analyzed result shows good linear relationship of $\Delta V - \Delta T$ curve in Figure 2-24(E). To double check the reliability of this result, another similar experiment is carried out using large $V_{f2}(t + \phi)$ in Equation 2.9 for a larger ΔT oscillation amplitude. Considering that the Seebeck voltage signal at larger ΔT should be significantly larger than the thermal drift noise voltage, the analyzed result is less affected by thermal drifting of the circuit. But on the other hand, a large temperature difference means higher temperature changing rate, and this may induce more errors from the thermal contact. As seen from Figure (E) and (F), the discrepancy of the result is quite large, even though both have good linearity.

In order to fully solve these uncertainties, the second challenge identified earlier must be solved, potentially using the split thermocouple method suggested in Section 2.3.2.

2.6 Calibration and Cross-Platform Comparison

2.6.1 Calibration method

The calibration of the system mainly involves the calibration of the absolute Seebeck coefficient of thermocouple probes. In this system, K type thermocouple is used for the measurement, and for most measurement the positive leg, Chromel, is used for Seebeck voltage sensing.

Copper has been chosen as the calibration sample, because there are published absolute Seebeck coefficient values of copper available over a wide temperature range [51]. By measuring the relative Seebeck coefficient of copper/Chromel, the absolute Seebeck coefficient of Chromel can be derived. Figure 2-25 show the measurement result of relative Seebeck coefficient ($S_{Chromel} - S_{copper}$) from room temperature to 200℃. The result matches with the literature values [60].

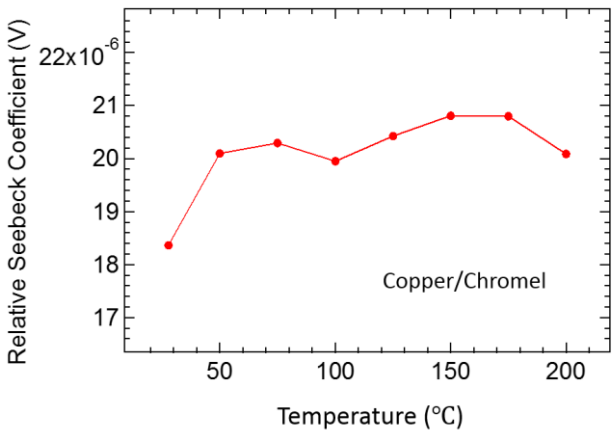

Figure 2-25 Calibration results of Chromel using copper as a standard sample.

2.6.2 Cross-platform comparison

Cross-platform comparisons with a commercial system, ZEM3, have been carried out using different thermoelectric samples.

The comparison of Seebeck coefficient measurement results for a $NaCo_2O_4$ sample is shown in Figure 2-26, and the difference in Seebeck coefficients measured by the two systems is less than 5 $\mu V/K$. Reduced Strontium Barium Niobate (SBN50) is used for a comparison of electrical resistivity measurements. As shown in the Figure 2-27, the shape of the measured curve is consistent, and with a small amount of offset about 8% in maximum.

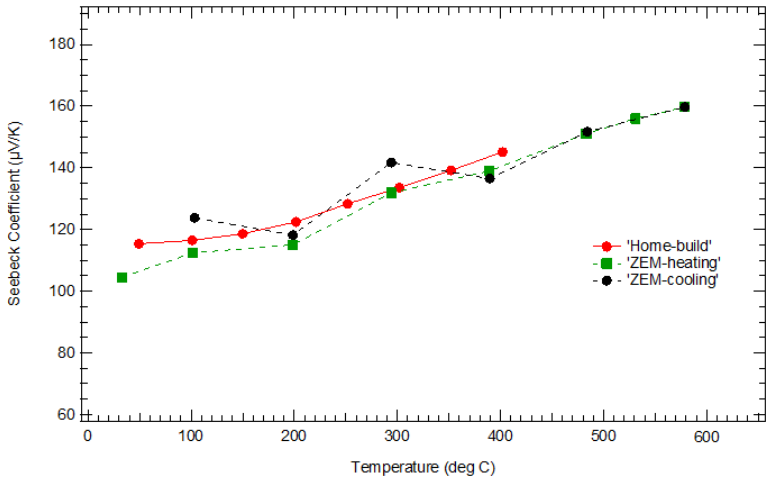

Figure 2-26 Cross-platform comparison of Seebeck coefficient measurement with ZEM3 system using a $NaCo_2O_4$ sample.

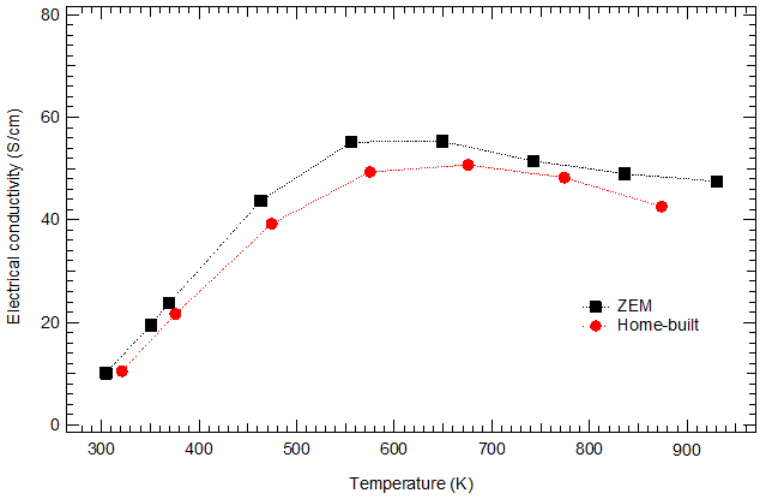

Figure 2-27 Cross-platform comparison of electrical resistivity measurement with ZEM3 system using a SBN50 sample.

2.6.3 Reproducibility test

$Ca_3Co_4O_9$ sample is used for testing the repeatability of the Seebeck measurement. Figure 2-28 shows a very good repeatability with five steady-state Seebeck coefficient measurement results, including measurement in cooling process. The standard deviation of the result is less than 0.5 μV/K.

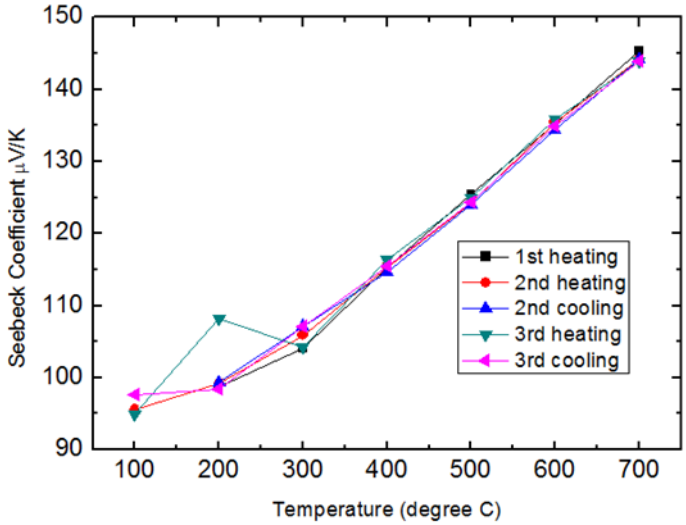

Figure 2-28 Repeatability of Seebeck coefficient measurement result of a $Ca_3Co_4O_9$ sample.

2.6.4 Temperature resolution test

Cu_2Se has been used for temperature resolution test for this system, since it has a sharp change of both Seebeck coefficient and electrical resistivity at its phase transition temperature around 125℃. The Seebeck measurement was taken every 2℃ with temperature difference smaller than 1℃ and an average temperature stability tolerance of 0.1℃/5min. Figure 2-29 (A) and (B) show the measurement results of Cu_2Se, which match well with the published results showing in Figure 2-29(C) and (D).

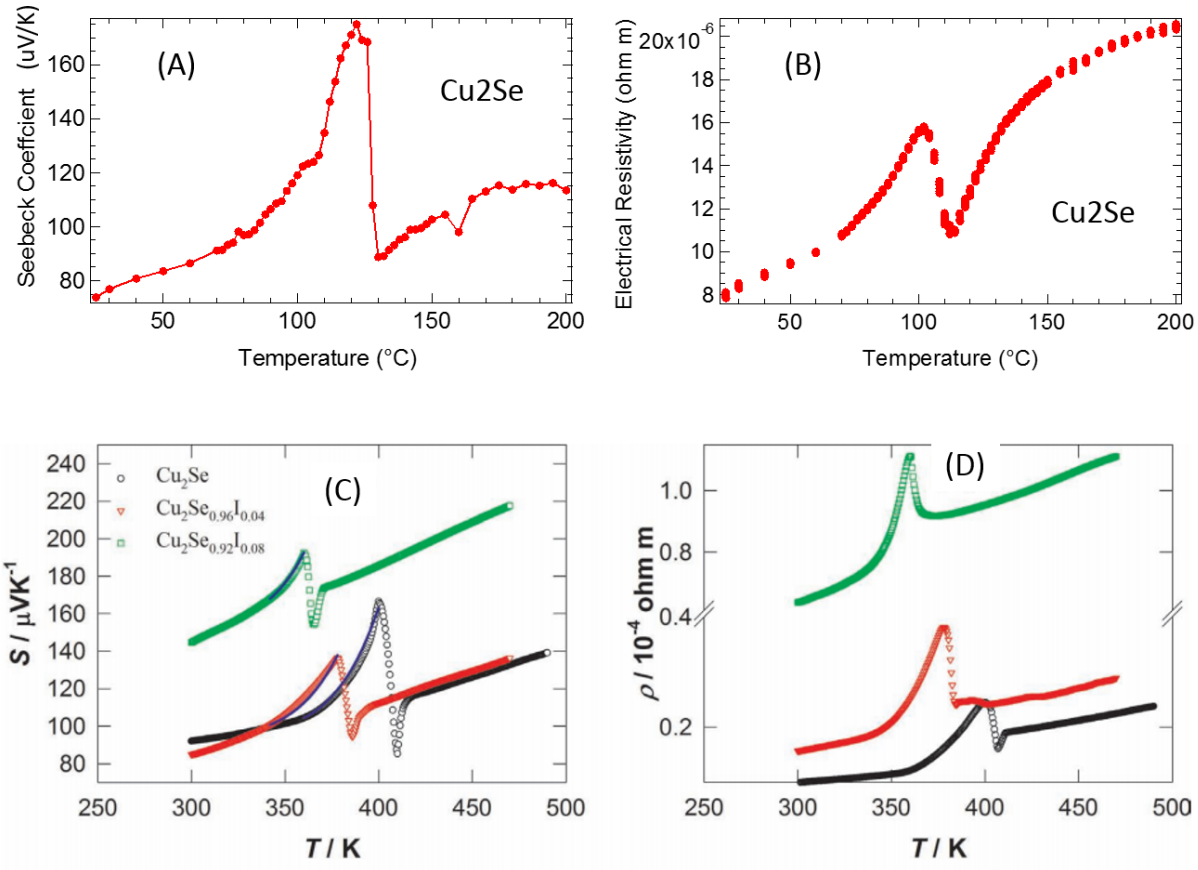

Figure 2-29 Seebeck coefficient and electrical resistivity measurement results from Cu_2Se; (A) Seebeck coefficient by this system; (B) Electrical resistivity by this system; (C) and (D) are results from literature [61].

2.7 Conclusion

In conclusion, a high temperature Seebeck coefficient and electrical resistivity measurement system has been successfully developed. The three main accomplishments of this system are listed as following:

1) Reliable mechanical structure is designed for a compact yet powerful high temperature measurement system. Original designs of test fixtures enhance the reliability and robustness of the system.
2) Design of the electronic controls and high temperature furnace allow accurate average and differential temperature control simultaneously, leading to a high Seebeck coefficient resolution in temperature.
3) Three different measurement procedures, including steady-state, quasi-steady-state, and DC dynamic methods, can be perform in the same setup without changing any of the hardware.

Future direction for further improvements is also discussed, for example the split thermocouple configuration for lag-free temperature measurement, which could potentially solve the major challenge existing in Seebeck coefficient measurements.

Chapter 3 Development of High Temperature Hall Effect Measurement System

3.1 Introduction

Although Seebeck coefficient and electrical resistivity measurement provides sufficient information for thermoelectric materials selection by rating their power factors, it is not enough for us to understand the microscopic material behaviors, the microscopic mechanism and how they are related to the overall performance. Hall effect measurement is an important experiment that can provide such insights.

Hall effect was discovered by E. H. Hall in 1879 during an investigation of the nature of the force acting on a conductor carrying a current in a magnetic field [62]. Hall found that when a magnetic field is applied perpendicular to the direction of current flow, as showing in Figure 3-1, an electric field is generated in a direction perpendicular to both the direction of the current and the magnetic field.

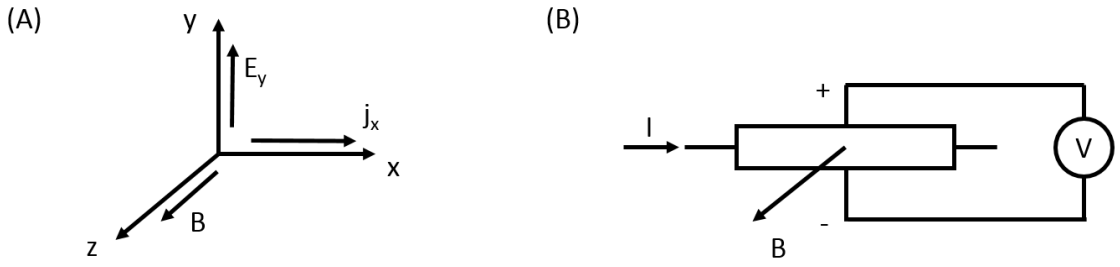

Figure 3-1 The Hall effect (A) relative direction of current, magnetic field and Hall field; and (B) schematic of Hall measurement

The hall coefficient R_H is defined as

$$\mathrm{R_H} = \frac{E_y}{j_x B} = -\frac{Vt}{IB} \tag{3.1}$$

Here, E_y, j_x, B are defined in Figure 3-1(A), V, I, B are defined in Figure 3-1(B), and t is the thickness of the tested sample along the magnetic field direction.

For a simple material where there is only one type of major charge carrier, the Hall coefficient can be used to calculate its charge carrier concentration:

$$R_H = \frac{1}{ne} \tag{3.2}$$

Here $\boldsymbol{e}$ denotes electronic charge, and the sign convention is adopted that when $\boldsymbol{e}$ is negative R_H is also negative.

Carrier concentration is directly related to the electrical conductivity and could changes substantially upon temperature change for semiconductors. In order to fully understand the electronic transport behavior of thermoelectric materials at high temperature, temperature dependent Hall effect measurement is needed in addition to Seebeck and resistivity measurement

3.2 Theory and Methodology

There are two methods available for Hall effect measurement, one is four probes method, and the other is Van der Pauw method.

3.2.1 Four probes method

The setup of four probes method for Hall effect measurement is actually the one that is used to define Hall effect, as shown in Figure 3-1. The measurement procedure and data analysis is straight forward, as discussed in section 3.1. The only difference in the real measurement is that there are noises and offset voltages to deal with. In order to eliminate errors from offset voltages and noises, linear regression method is used to derive the Hall coefficient by measuring the slope of multiple data points with different current and magnetic field values.

The sample for four probes method is a rectangular bar, with length at least twice of the width. From equation, it is clear that the sample should be thin to increase the magnitude of Hall voltage signal.

3.2.2 Van der Pauw method

Van der Pauw method is widely used for electrical resistivity and Hall effect measurement of thin films. There is no strict requirement on sample geometry, as long as the sample is thin and has a uniform thickness [63]. For bulk materials, the thickness of which is much larger than the thin film, several preferred geometries should be used for accurate measurement [50].

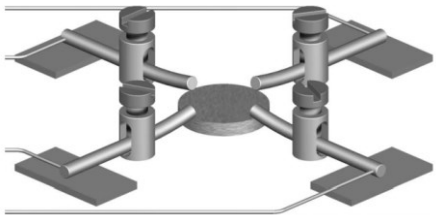

Figure 3-2 Hall effect test fixtures for a disc sample using the Van der Pauw method [50].

A simple Van der Pauw test fixture for measuring Hall effect of a round pellet is shown in Figure 3-2 [50]. A pellet sample actually is more convenient to prepare than a rectangular sample, because most thermoelectric sample are consolidated in a round die and come out in a disc shape. But there are also some disadvantages, for example, with a very small Hall coefficient, the sample has to be grinded to a thickness less than 0.5 mm. A disc sample at such thickness is very fragile for most materials.

In this work, four probes method is adopted for another reason, the difficulty in electronic control and data accuracy examination. A complete Van der Pauw method requires at least 8 measurements of current and voltage setups for all the combination of 4 leads, which requires a programmable controlled multiplexer in addition to other instruments, and the final result is derived from a non-linear equation [63]. It is more difficult to check the accuracy of the results from Van der Pauw measurements than four probes method, in which the linearity of data points is typically sufficient to indicate the reliability of the results.

3.3 Scientific and Engineering Challenges

High temperature Hall effect measurement for bulk specimen is known to be difficult. Following are three major challenges:

3.3.1 Voltage signal over thermal noise

From the Equations 3.1 and 3.2, it is easy to derive:

$$V = \frac{IB}{net} \tag{3.3}$$

Here V is the Hall voltage, the main signal of the experiment. For a current I of 100mA, a magnetic field of 1 T, and a sample with a carrier concentration of $10^{20}\mathrm{cm}^{-3}$ and a thickness of 1mm, the measured V is less than 10μV. For thermoelectric materials, a Seebeck coefficient larger than 100 μV is not unusual, so an oscillation of temperature difference around 0.1℃ at the Hall probe contact will completely distort the real signal.

The Hall voltage signal increases with current, but normally the applied current is smaller than 100 mA. One of the reasons is that current may cause temperature change in the sample, for example, by the Joule heating, Peltier effect and Thomson effect.

Reducing thickness is also helpful. But once a bulk sample is grinded down to 0.3 mm, the sample will be very fragile and easy to break during the handling.

3.3.2 Magnetic field

Large magnetic field is usually needed for Hall effect measurements in order to increase the magnitude of Hall voltage signal.

There are generally two types of magnets that are used for Hall effect measurements: superconducting magnets and DC magnets.

Superconducting magnet

Superconducting magnets are often used for high magnetic field (> 5T) applications. It does not have issues of overheating due to large current as normal DC magnet. But the superconducting coil needs to achieve its superconducting state in order to work, which requires special cooling techniques, and usually liquid helium is necessary. Because of the low operating temperature of superconducting coil, the mechanical system is complicated and the space available for sample fixture design is very limited.

DC magnet

Large DC magnet is capable of providing a magnetic field larger than 1 T. In addition to number of turns of coils and supplied current, the pole spacing is also very important and has a large effect on the final field strength generated. Figure 3-3 (B) show the relationship between the field strength and pole gap. In this system, a DC magnet with a pole face diameter of 100 mm is used. According

to Figure 3-3(B), to achieve a maximum field strength of 2T, a pole gap of 20 mm is required. 20mm spacing is not a problem for room temperature setup, but for a high temperature measurement that requires a vacuum chamber, water cooling system and heating stage, it is a quite difficult requirement.

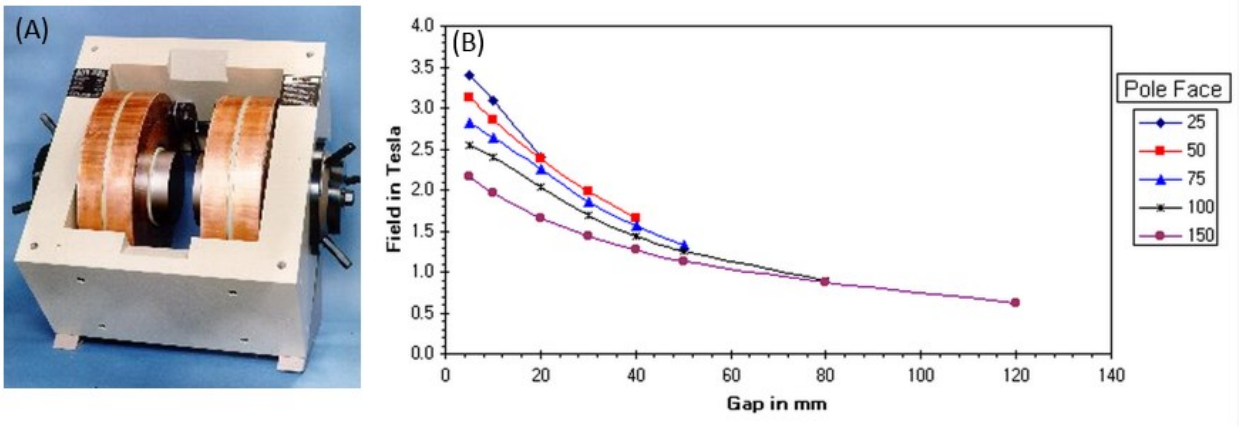

Figure 3-3 Magnetic field strength as a function of pole gap: (A) the DC magnet used for this measurement, and (B) magnetic field at a current of 70A with different pole configurations.

3.3.3 Electrical contact

Electrical contact is usually a problem for high temperature measurement. Pressure contacts are favored for high temperature test fixture, because they can accommodate large thermal expansion due to temperature change. But it is often difficult to find a spring that works at high temperature. C. Wood used sapphire leaf springs to exert pressure between the electrode and the sample [64]. In this work pogo pins was used for convenience.

Alignment of Hall probes is also very important, especially for sample that has high electrical resistivity. The misalignment will cause a large resistive voltage overlap on the tap of Hall voltage

signal. Alignment of Hall probes is mostly done manually and could be very time consuming, because of the poor designs of the test fixtures.

3.4 Design of Mechanical Structures and Electronic Controls

This design of Hall measurement system is guided by three goals: (1) achieve maximum magnetic field of 2T using existing DC magnet; (2) easy sample installation and reliable electrical contacts; and (3) high temperature measurement ability and low thermal noise. The system design of mechanical will be discussed following in three main parts: the heating stage, the electrical test fixtures, and the environment controlled chamber.

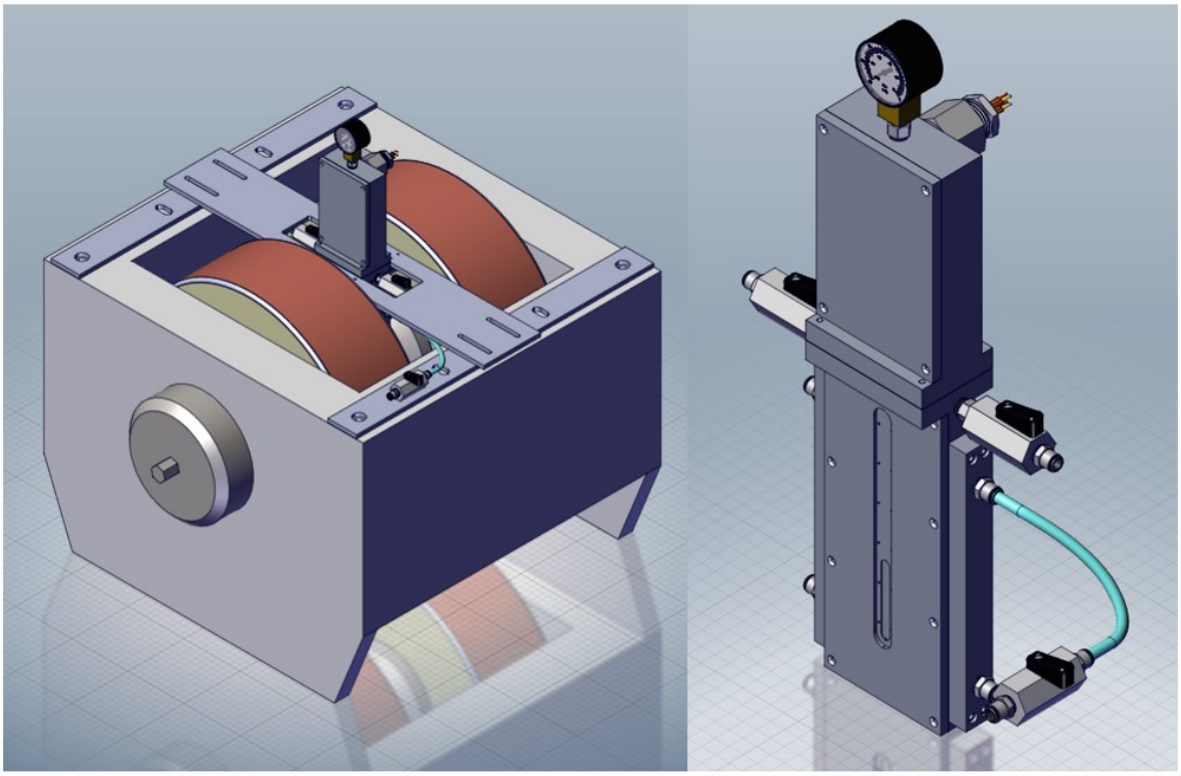

Figure 3-4 Overview of the mechanical structure design of the high temperature Hall effect measurement system.

3.4.1 Heating stage

Figure 3-5 shows the design of high temperature heating stage for this system. The main body of the heater is machined from a brick of boron nitride, which has a very high thermal conductivity to ensure uniform temperature distribution in the sample. Nickel Chrome wire is used as the heater, the wire is insulated from each other by the 4-bore ceramic tubes. The heating wire assembly is then plugged into the pre-machined holes in the boron nitride stage. With this heater, the stage can be easily heated up to 500 ℃.

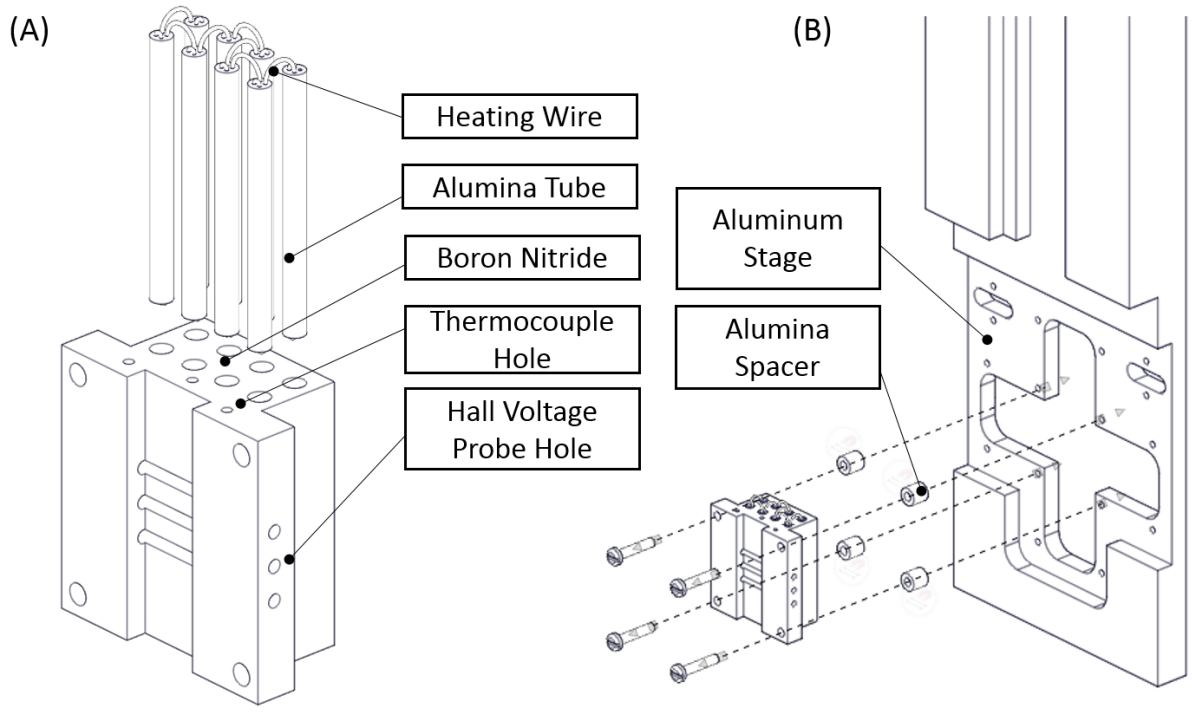

Figure 3-5 Heating stage design for the Hall effect measurement system.

On the top of the stage, as shown in Figure 3-5(A), there are holes for thermocouples to measure the temperature of the sample. On each side of the stage, there are three holes for Hall probes alignment.

The sample stage is fixed on an aluminum substrate using #0-80 stainless steel screws, as shown in Figure 3-5(B). Since the aluminum and boron nitride are both highly thermal conductive, the aluminum substrate could act as a large heat sink that will limit the heating ability of boron nitride heater. So an open slot in the middle of aluminum substrate is designed and four alumina ceramic spacers are used to separate the boron nitride stage from aluminum base. This design not only solves the thermal conduction problem but also reduces the total height of the assembly to the height of the heater itself.

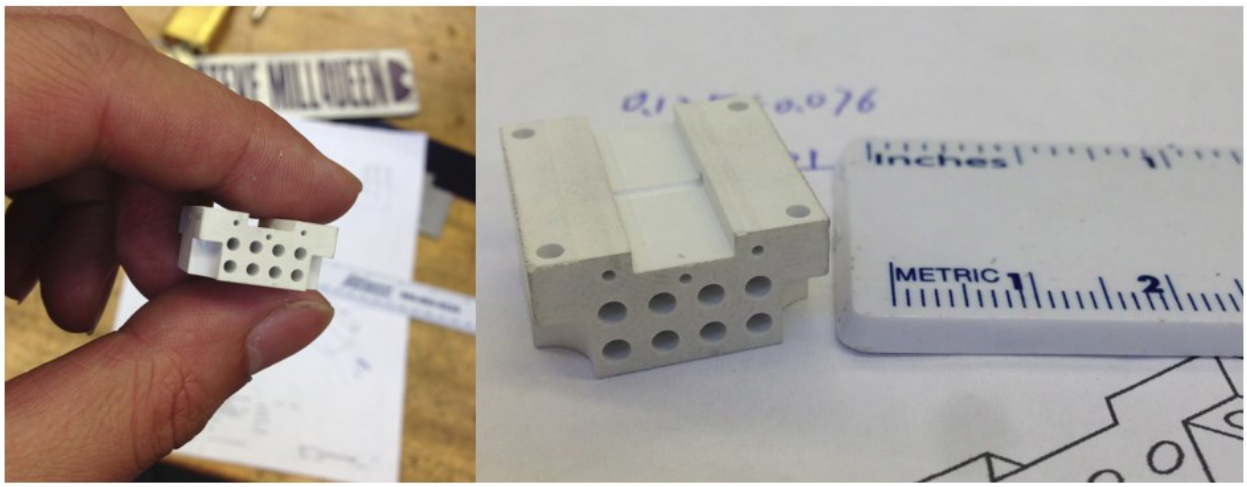

Figure 3-6 Actual size of the heating stage when compared to a finger and a ruler.

The size of the heater is the key for achieving the high magnetic field strength. The heater assembly in this design is as small as 0.75 inches wide and 0.5 inches thick, as shown in Figure 3-6.

3.4.2 Electrical contacts

The electrical contacts and wiring terminals are designed to be reliable, compact and compatible with high temperature measurement. All the parts are designed to be compact, as showing in Figure 3-7(B). The total thickness of the entire assembly is less than 12.7 mm.

The design is discussed separately in three parts bellow: the current terminals, the hall voltage probe, and the wire terminals.

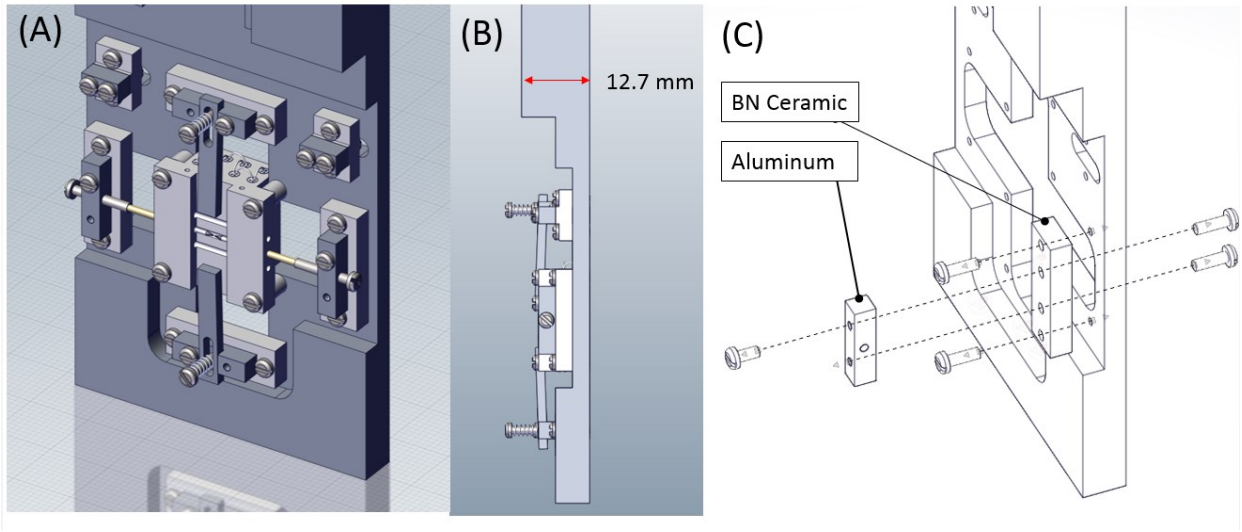

Figure 3-7 Electrical contact design in the Hall effect measurement system.

Current terminals

Current terminals are used to supply the current through the sample, and to fix the sample to the heating stage.

Two aluminum parts are designed to hold down the top and bottom end of the sample against the heating stage using a stainless screw and a spring. The spring ensures a pressured electrical contact between the electrodes and sample to accommodate possible thermal expansion during

measurement. In the future, nickel alloy will be used instead of aluminum for better high temperature compatibility.

Hall voltage probe

Pogo pins are used as the Hall voltage probe. The outer diameter of these pogo pins is about 1mm. The spring inside the pogo pin makes the electrical contacts very reliable during measurement. Unfortunately, the spring system can only work at a temperature less than 500°C.

The pogo pin is placed in the alignment hole on the heating stage. Simply by using the screw on the side to push the pogo pin against the sample, electrical contacts with good alignment of both probes are made, and there is no more painful alignment process.

Wire terminals and electrical insulations

The electrical insulations from probes to probes are very important. First, they need to be separated from the aluminum substrate. This is achieved by adding a boron nitride separator. Figure 3-7(C) shows the design of insulation setup, which avoids tapping threads inside the boron nitride and greatly increases the reliability of the mechanical structure.

3.4.3 Environmental controlled chamber

A water cooled aluminum vacuum chamber is designed and manufactured for this system, as shown in Figure 3-8.

The water cooling block is positioned on the left and right side instead of front and back, as shown in Figure 3-8(B). This design is chosen to reduce the total thickness.

The chamber is fixed on the DC magnet using designed frames. The frames lock the main chamber at the center position of the magnet pole. So when changing the sample, just extract the upper part, install the sample and plug it back, as shown in Figure 3-8(A). This snug fit design ensures a perfect alignment between the central axis of the magnet pole and the sample.

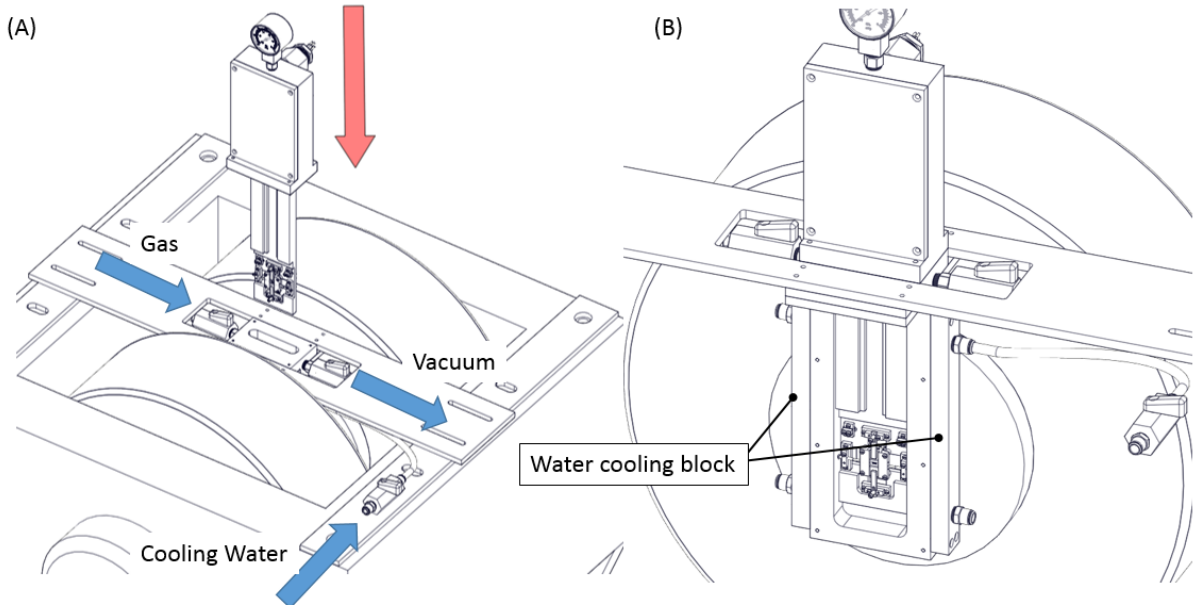

Figure 3-8 Environmental chamber design and the alignment-free plug-and-seal mechanism.

There are two ball valves on the sides of the main chamber, which controls the purging and evacuating process. The cooling water flow is also controlled by an in-line ball valve.

On the front cover of the main chamber, a slot is designed at the center of the surface for positioning of the Hall sensor, as shown in Figure 3-4. The Hall sensor is used to measure the magnetic field at the sample position.

3.4.4 Instrumentation and measurements

Table 3-1 lists the instruments used for this system. As shown in Figure 3-9, the magnetic field is sensed by a Gauss meter (Lakeshore 421) using a Hall effect sensor (Lakeshore HGT-1010). The magnetic field is controlled by manually adjust the Sorensen power supply (SGA60/83C-0AAA).

Table 3-1 Instrumentation List for Seebeck & Resistivity Measurement System

Model	Function	Quantity
Lakeshore 421 Gauss Meter	Magnetic field measurement	1
Keithley 181 Nanovoltmeter	Hall voltage measurement	1
Keithley 224 Source Meter	Constant current supply	1
Sorensen SGA60/83C Power Supply	Power supply for DC magnet	1
Variable AC transformer (500W)	Power for Heating Stage	1
PID Temperature Controller	Temperature Monitoring only	1

The temperature of the heating stage is controlled manually through a variable AC transformer, and the temperature is monitored by a commercial available PID controller. The reason of control the power manually is that the PID controlled dynamic equilibrium is not stable enough, the noise induced by the small temperature oscillation makes the measurement very difficult. Instead, an old school method is adopted, by blindly twisting the transformer to a voltage setting, and the heating eventually stables at a temperature, with much lower noise level. The drawback of this temperature control is that the testing temperature cannot be set precisely. After developed the DC PID heating control in Chapter 2, it may worth a try in the future to use the DC power supply plus PID algorithm to control the temperature.

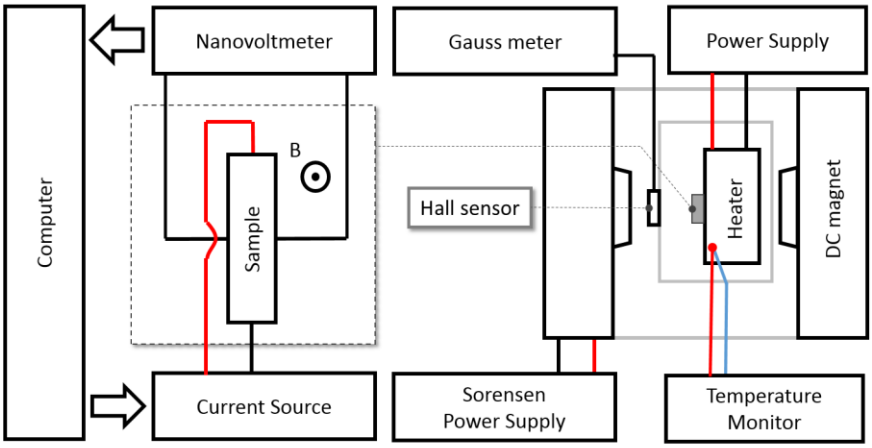

Figure 3-9 Schematic electrical diagram of Hall effect measurement system.

The current through the sample is supplied by Keithley 224 Source Meter and controlled through a custom designed software in LabVIEW. The Hall voltage is also monitored by the software through a Keithley 181 nanovoltmeter.

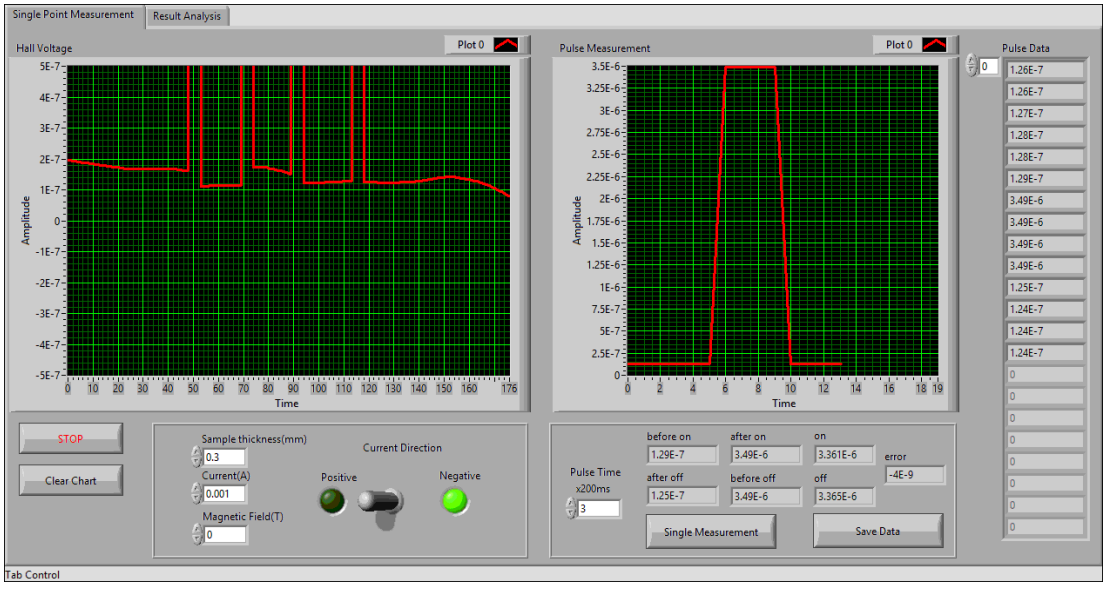

Figure 3-10 LabVIEW program for current control and Hall voltage measurement.

3.5 Development of Measurement Procedures

Figure 3-11 shows the measurement procedure of the Hall effect testing system. Same measurement is carried out at each temperature point. Before the $I-V$ measurement, the heater has to achieve its thermal equilibrium. When the temperature is stable enough, a magnetic field is set up corresponding to its process index (B_j). When the magnetic field is stable, usually taking only several seconds, $I-V$ sweep is performed. A Hall resistance value R_j can be obtained from the slope of $I-V$ curve. Then we move on to next magnetic field strength setting (B_{j+1}). After all the magnetic field levels are measured at this temperature, all the Hall resistance values and corresponding field can be plot in a $B-R$ curve, and the slope of the $B-R$ curve is directly related to the Hall coefficient and sample thickness. The Hall coefficient at this temperature is then calculated and the measurement moves on to the next temperature setting.

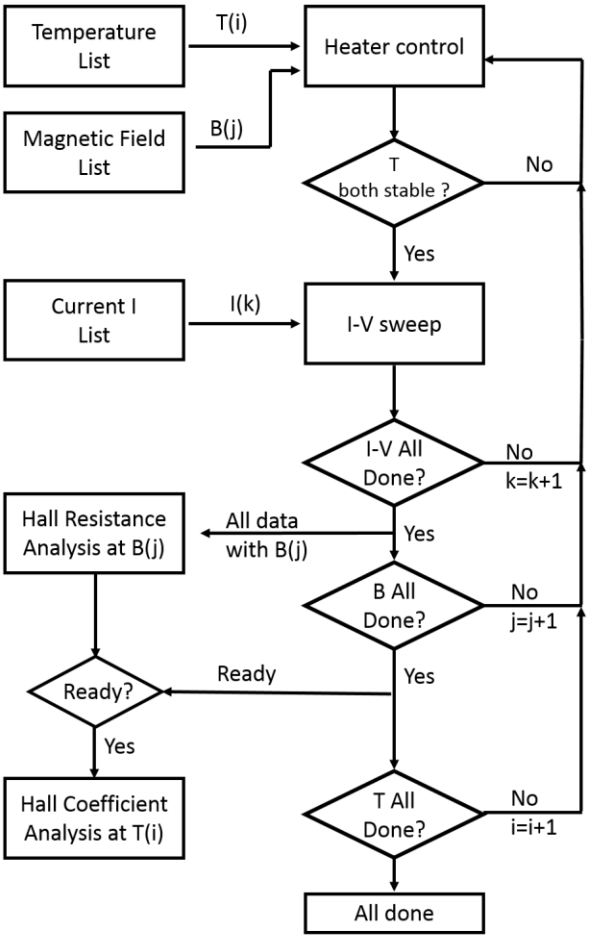

Figure 3-11 Flow diagram of DC dynamic measurement procedure

3.6 Performance and Error Analysis

3.6.1 Performance

Figure 3-12 shows the high temperature Hall effect measurement results of a $Y_{0.3}Co_4Sb_{12}$ sample. The carrier concentration of the sample is measured as a function of temperature from room temperature to 450 °C. All the data have good linearity for $I-V$ and $B-R$ curve fitting. The $B-R$ relation at 300°C is shown in Figure 3-12(B).

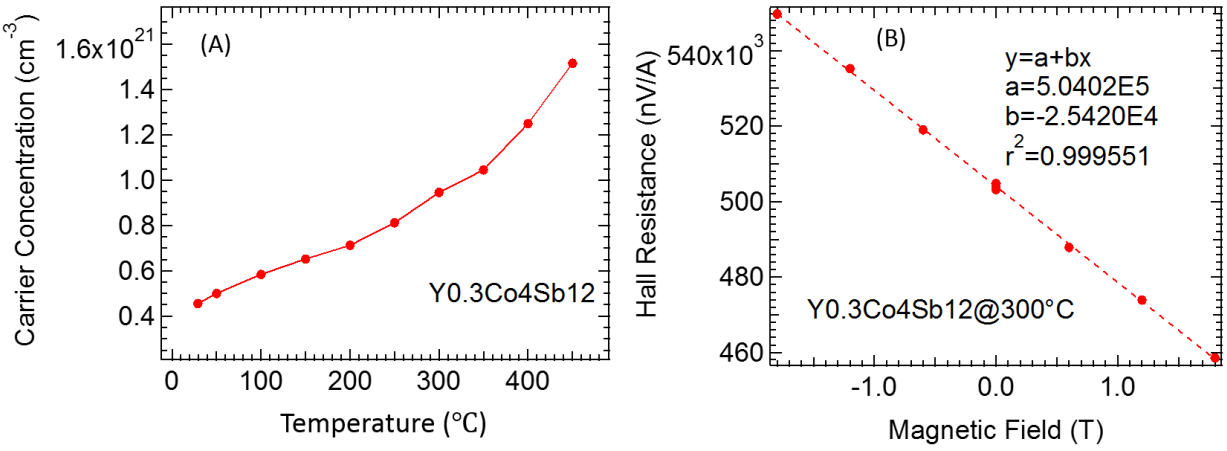

Figure 3-12 High temperature Hall effect measurement result; (A) Carrier concentration of $Y_{0.3}Co_4Sb_{12}$; and (B) B-R curve fitting for $Y_{0.3}Co_4Sb_{12}$ at 300°C.

3.6.2 Capability

This section is to summarize the measurement capability of the system. Table 3-2 lists the limits of the major control parameters.

The upper limit of the carrier concentration that can be measured can be estimated following the procedure discussed in Section 3.3.1. According to the maximium field and current setting, and considering a maximum Hall voltage signal of 100nV, the sample that can be measured should have a carrier concentration upper limit of $1 \times 10^{23}\text{cm}^{-3}$. However, the electrical resistivity could also play an important role in voltage noise, and for materials with high electrical resistivity, the carrier concentration upper limit should be lower than $1 \times 10^{23}\text{cm}^{-3}$.

Table 3-2 Instrument capability of the Hall effect testing system

Parameter	Maximum	Minimum	Resolution
Temperature	$500°C$	Room temperature	0.1℃
Magnetic field	$\pm$1.88 T	0T	10mT
Current	$\pm$100mA	0mA	5nA
Voltage	$\pm$2mV	0V	1nV

3.6.3 Error analysis

There are three main error source that affects the final measurement result, as discussed below:

Sample geometry

A good sample is very important for the measurement, and a parallel surface with a uniform thickness is needed for a high accurate measurement.

Spurious voltage

Spurious voltage from bad electronic contact and electrostatic charges are usually very small, but large enough to mess up the Hall voltage signal. During $I-V$ measurement, each point should be varied for multiple times, and ideally using a program controlled pulse measurement procedure.

Thermal drfting

Thermal drifting is the most difficult error source to eliminate. It is unavoidable for high temperature measurement. In addition to using high resolution PID controller, another choice is to perform the measurement as fast as possible, and each $I-V$ curve and magnetic field level

measurement should be completed before the voltages drifts too far away from the value at the beginning.

3.7 Conclusion

In this chapter, a high temperature Hall effect measurement system has been successfully developed and tested up to 500°C. Three main accomplishments of this systems are listed as following:

1) Low profile high temperature heating stage is designed successfully that minimizes the thickness of entire system by reducing the thickness of test fixture portion down to 0.5 inch.
2) Pogo pins and alignment channels are designed for easy sample installation and reliable electrical contact against the thermal expansion effect.
3) Environment controlled chamber are designed with a thickness less than 1 inch. This low profile design pushes the up limit of magnetic field to 1.88 T. Alignment free Plug-and-seal mechanical design ensures all the sample are located in the central of magnet pole, and also makes the sample change process much easier.

Further improvement options are also discussed: (1) a DC powered PID control could potentially solve the thermal noise problem while ensure the temperature control accuracy; (2) high temperature pogo pin and current electrode can be designed and used to extend the upper temperature limit of the system; (3) automatically data collection software including magnetic field control can be developed for more complicated and fast measurement.

Chapter 4 Development of Scanning Thermal Microscopy for Localized Conductivity Measurement

4.1 Introduction

As discussed in the beginning of Chapter 3, Seebeck coefficient and electrical resistivity measurement in bulk specimens are sufficient for materials selection purpose, but not enough to provide deep physical understanding on the measured materials behavior. As more and more studies are published on nanostructure engineering for thermoelectric performance improvement [65, 66], it is worthwhile asking why and how those nanostructures work, and these require measuring and quantifying the structure-performance relationship at the nanoscale. For example, many nanocomposites have nanoscale secondary phase and sharp boundaries that have great effects on bulk scale electrical and thermal transport properties [46], but there are very few work reported in probing these interfaces at the nanoscale. In addition to the technical difficulties, major barrier also exists on how to establish the relationship between observed local structures or properties and the macroscale performance.

Scanning Probe Microscopy (SPM) is a versatile tool that allows local characterization of different properties with nanoscale spatial resolution. Most applications of SPM are focused on characterization of low dimensional systems, such as thin films [67, 68], nanofibers and nanowires [69, 70]. In these low dimensional materials, boundaries and interfaces exist between materials of interest and other supporting or reference materials. Those boundaries can be studied by SPM to reveal the structure and properties of the target materials. For example, for a single $NaCo_2O_4$ nanofiber deposited on a SiO_2 substrate with one end grounded, when a conductive AFM (cAFM)

measurement is performed, the nanofiber geometry and current flow can be directly mapped in the scanned images [69].

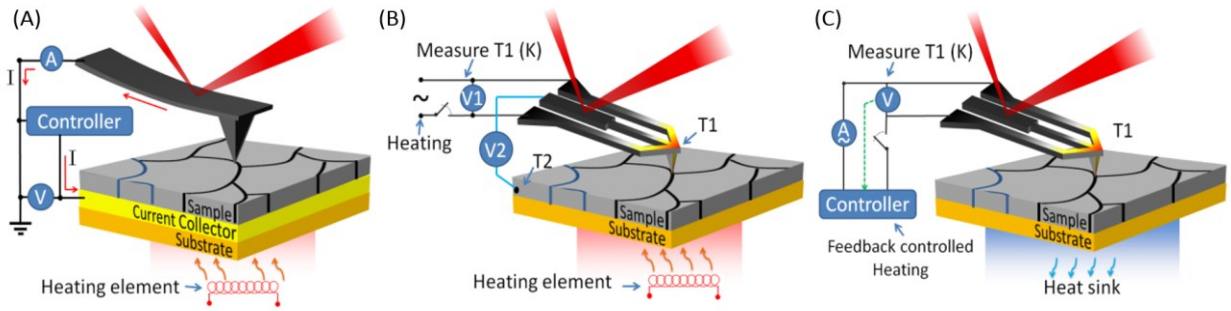

Figure 4-1 SPM setups for localized thermoelectric properties measurement; (A) localized electrical resistivity measurement; (B) localized Seebeck effect measurement; (C) localized thermal conductivity measurement.

Some proposed ideas for SPM characterization of local thermoelectric properties of nanostructured thermoelectric materials are shown in Figure 4-1. Three local properties are of interests, including electrical transport properties, Seebeck effect, and thermal transport properties. As showing in Figure 4-1(A), cAFM can be directly used for the study of local electrical transport properties. For local Seebeck coefficient measurement setup described in Figure 4-1(B), ideally it requires a probe with three separated conductive circuit paths [71], one for Seebeck voltage sensing and two for local heating. But it very difficult to find or fabricate such probes. For local thermal conductivity measurement, it only requires a probe with heating option. Nevertheless the scanning thermal microscopy has not been extensively researched, mostly due to the price of the heating probes and the difficulty of measurement including instrumentation and data analysis.

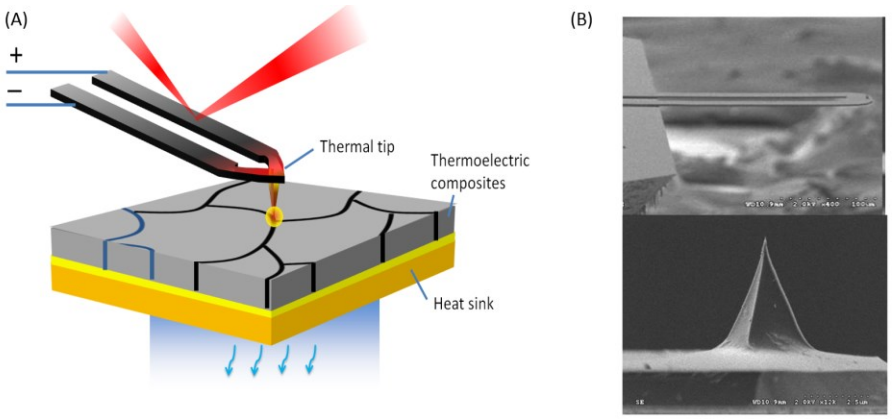

Figure 4-2 Schematic of scanning thermal microscopy; (A) localized thermal transport measurement using a heated probe; (B) SEM images of the heating probe.

4.2 Theory and Methodology

The basic idea of scanning thermal microscopy implemented in this thesis is very simple, as showing in Figure 4-2. The measurement technique is often called "hot finger technique". First the probe is heated to a temperature higher than room temperature, then the probe is moved toward the sample. When the probes is in contact with the sample, an extra solid-solid heat flux path is open for heat flow, so the temperature of the probe goes down. When the probe is in contact with materials of different thermal transport properties, the temperature of probe will be different. So the thermal properties of materials can be qualitatively measured by recording the difference of probe temperature at each location.

The scanning thermal microscopy instrumentation in this work is designed based on the hardware and software of Asylum MFP-3D AFM system. Figure 4-2 (B) shows scanning electron microscopy (SEM) images of the thermal probes used in this work. The probe have two separated legs with electrical conduction pads. The legs are heavily doped silicon and highly electrical conductive. It is at the tip where the most resistive part locates. When a current is applied through

the probe, the joule heating will be generated at tip area. When measuring the total resistance, the resistance change at the tip is responsible for majority of resistance changes in the circuit. Since the resistance change of the tip usually indicates a temperature change at tip, the temperature changing can also be obtained by measuring the total resistance change.

4.3 Scientific and Engineering Challenges

Although the basic idea of scanning thermal microscopy is simple, the real measurement and analysis could be very complicated, especially when a quantitative result is required. Following are several major difficulties and challenges in this area:

4.3.1 Cross-talk with topography

The earliest scanning thermal microscopy was actually designed for surface morphology characterization rather than thermal properties measurement [72], and applications such as thermal topography measurements have also been reported [73]. However, for pure thermal conductivity characterization, this feature is not desirable. To solve this problem, the easiest method is to polish the surface of the sample so that there is no height difference in the scanning area. Scanning in the vacuum environment may also helpful to eliminate this crosstalk, since the heat convection path is eliminated at high vacuum.

4.3.2 Temperature calibration

It is mentioned that the resistance of the probe is directly related with the tip temperature. But in order to get the real temperature value, one should calibrate the probe before the experiment. There are only several calibration techniques available, for example, using Raman spectroscopy [73] or

using polymers with different glass-transition temperatures [74]. None of those techniques are available to the normal users.

4.3.3 Heat propagation

This point of difficulty is noticed during the experiment of this work. A strong thermal drift is observed during a continuous contact mapping with a heated probe. Such heat propagation problem could potentially be minimized by controlling the scanning speed.

4.4 Development of Measurement Procedures and Electronic Controls

In this section, four different SThM measurement procedures are developed together with their electronic controls: calibration mode, constant voltage mode, constant current mode and constant temperature mode.

4.4.1 Calibration mode

The purpose of calibration mode is to identify a suitable range of heating power for the thermal probe. This power range is used to prevent the probe from overheating during the measurement. The calibration process measures the relationship between power input and probe resistance. The circuitry built for calibration mode is shown in Figure 4-3. A BNC output channel ($BNC_{out\ 0}$) on the Asylum MFP-3D controller is used to power the whole circuit, and the output voltage (V_{out_set}) can be adjusted through the software. A BNC input channel ($BNC_{in\ 1}$) is used to measure the actual output voltage (V_{out}), since there could be a non-negligible difference between the value set in software and the real output. A standard $1k\Omega$ resistor (R_{ref}) is connected in series to the tip for current sensing. Another BNC input channel ($BNC_{in\ 0}$) is used to monitor the voltage over the reference resistor (V_{ref}). So the current passing through the probe is V_{ref}/R_{ref}, and the voltage

drop over the probe is $V_{out} - V_{ref}$. Knowing the current and voltage, the power and resistance of the thermal probe can be easily calculated.

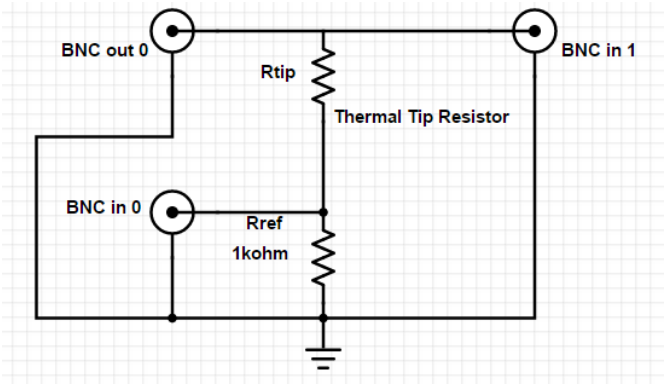

Figure 4-3 Electrical schematic of thermal probe calibration circuit.

In addition to its calibration purpose, the circuit shown in Figure 4-3 is also used for thermal conductivity measurement. A simple proof of concept experiment has been carried out: using the heated probe to approach a substrate such as glass slide and measures the temperature change at the tip. In this experiment, two equilibrium states are measured for simplicity:

(1) Withdraw state: the probe is far from the substrate;

(2) Engaged state: the probe is in pressured contact with the substrate.

Assuming a constant voltage output of V_{out} is applied to the circuit. At the withdraw state the BNC in 0 measures V_{ref}, and at the engage state it measures V'_{ref}. The resistance change of the tip ($\Delta R_{tip} = R_{engage} - R_{withdraw}$) can be calculated through following equation.

$$\Delta R_{tip} = R_{ref} * V_{out} * (\frac{1}{V'_{ref}} - \frac{1}{V_{ref}}) \quad (4.1)$$

Figure 4-4 shows the measurement results on glass slide and gold coated silicon wafer. The negative value of ΔR_{tip} indicates the tip becomes colder when it falls in contact with the substrate. It also shows that, with a higher heating power, a larger change of tip resistance takes place. By comparing the high power data ($V_{out} \geq 3V$), the resistance drop at gold coated silicon wafer is larger than the glass slide, which suggests gold coat silicon wafer is more thermally conductive.

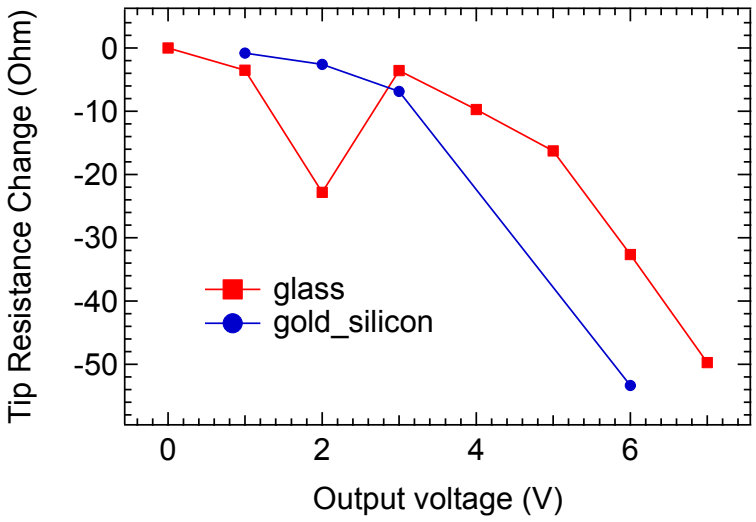

Figure 4-4 Single point thermal transport measurement on glass slide and gold coated silicon.

From Figure 4-4, it may be worth noting that the change of resistance (~10s Ω) is actually much smaller compared to the tip resistor value (~3 kΩ). Similarly, the measured thermal signal is at mV level, and the total voltage drop over the reference resistor is on the order of 1V. This makes it very difficult to accurately measure the small thermal signal, since any spurious noise at mV level from the output voltage line could easily distort the thermal voltage. This problem could become even more serious for thermal mapping. Figure 4-5 shows a mapping result on a gold coated silicon

wafer, the probe was scanning across the edge of the gold trace and the voltage signal V_{ref} was measured voltage drop over the reference resistor. From the color bar of Figure 4-5(c), it shows the effective thermal signal is about 0.6 mV, and the baseline of the voltage signal is about 1V. It is not a surprise that the thermal image is of such a low resolution. Based on the foregoing discussion, a higher V_{ref} signal leads to a lower tip resistance, and a lower tip temperature, therefore a location with higher thermal conductivity. So the result in Figure 4-5(C) indicates that gold has a high thermal conductivity than SiO_2, which is reasonable except the poor resolution.

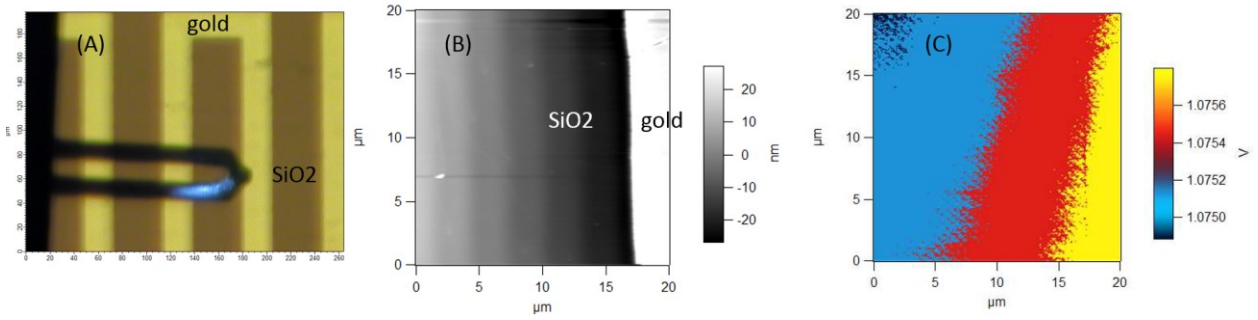

Figure 4-5 Thermal mapping of a gold trace on a SiO_2 substrate under calibration mode: (A) optical image, (B) height mapping, (C) mapping of thermal signal V_{ref}.

4.4.2 Constant voltage mode

To improve the resolution of thermal image, a circuit with Wheatstone bridge and operational amplifiers has been designed for constant voltage mode, as shown in Figure 4-6. The Wheatstone bridge is used to eliminate the baseline of the thermal voltage. For each scanning, the tip is heated with a constant voltage output through $BNC_{out\,0}$ channel, and, before engaging the tip to the sample, the voltage measured at $BNC_{in\,0}$ channel (V_{in}) is adjusted to near 0 mV through the variable resistor. A differential op-amp is used to measure the voltage difference at the two junction

of Wheatstone bridge, and two buffer op-amp are used to minimize the disturbance of original circuit. The gain of the differential op-amp is set to about 40.

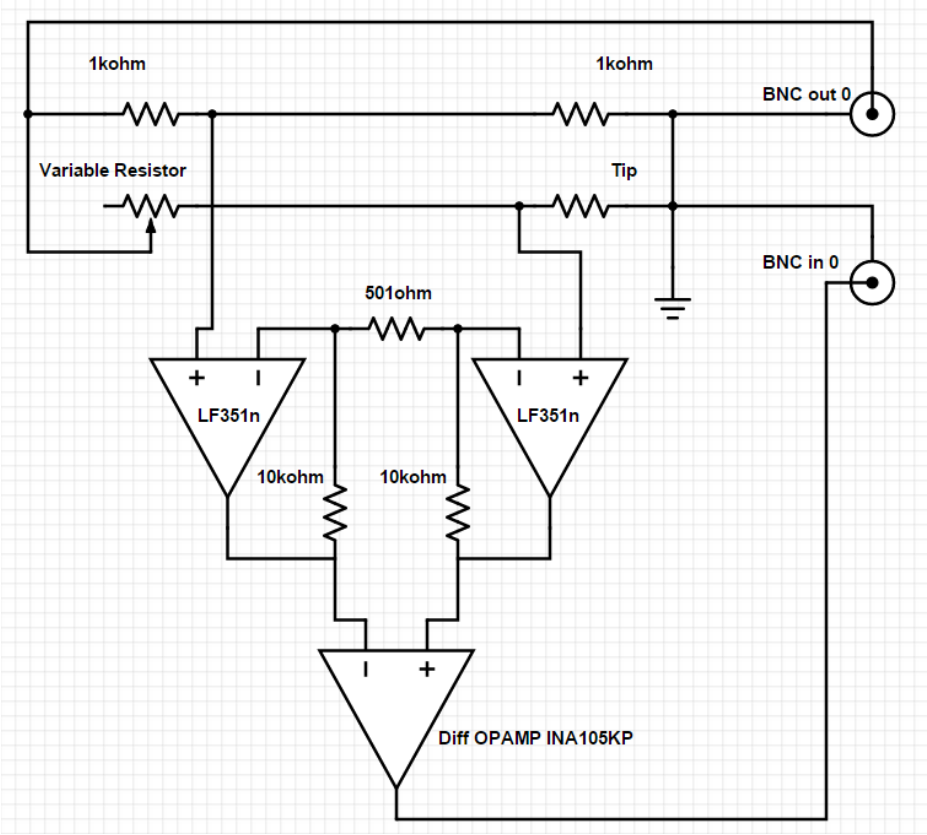

Figure 4-6 Electrical schematic of constant voltage mode circuit.

A thermal mapping at the same region of Figure 4-5 is performed using this circuit. The result is shown in Figure 4-7. From the color bar in Figure 4-7(C), the thermal signal is around 16 mV with a base line voltage less than 2mV. It is clear that the thermal image by this circuit is of a much higher resolution. The color scale is opposite to the calibration mode circuit due to different circuit arrangement. Here, cold color (blue) indicates lower tip temperature or higher thermal conductivity.

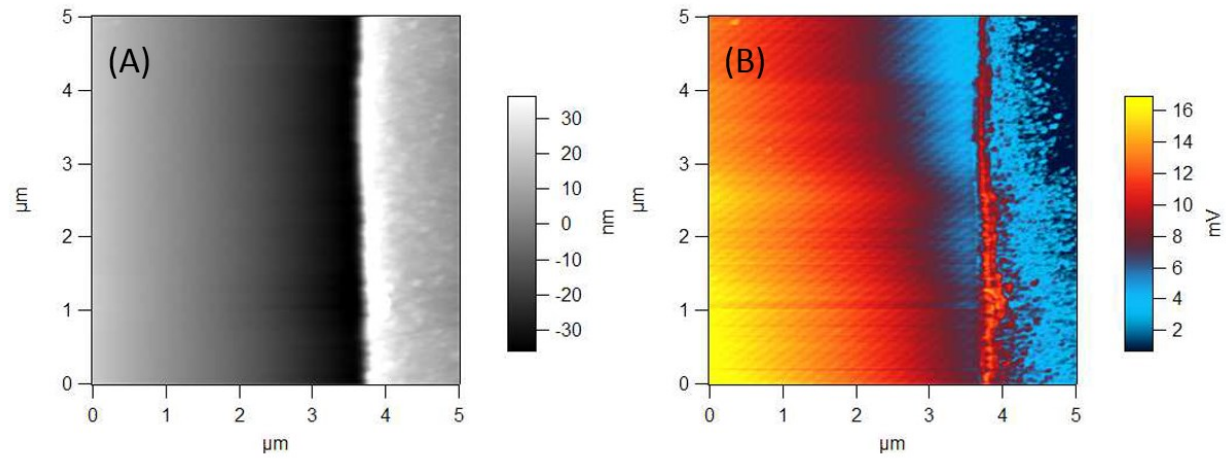

Figure 4-7 Thermal mapping of a gold trace on a SiO_2 substrate under constant voltage mode; (A) height mapping; and (B) mapping of thermal signal V_{ref}.

4.4.3 Constant current mode

The constant current mode circuit is developed, as shown in Figure 4-8, with a similar functionality as the constant voltage mode one. The only difference is that, in this circuit, when the $BNC_{out\ 0}$ output voltage (V_{out}) is fixed, the current that flows through the thermal probe is also kept as a constant. The purpose of constant current mode is for the convenience of heating power calculation at the tip area. Since the current always stays constant, the power is then directly related to the tip resistance. In contrast, in the foregoing constant voltage setup, whenever the voltage changes, the current and the resistance of the probe both changes, and it is more difficult to trace the total heating power change of the probe.

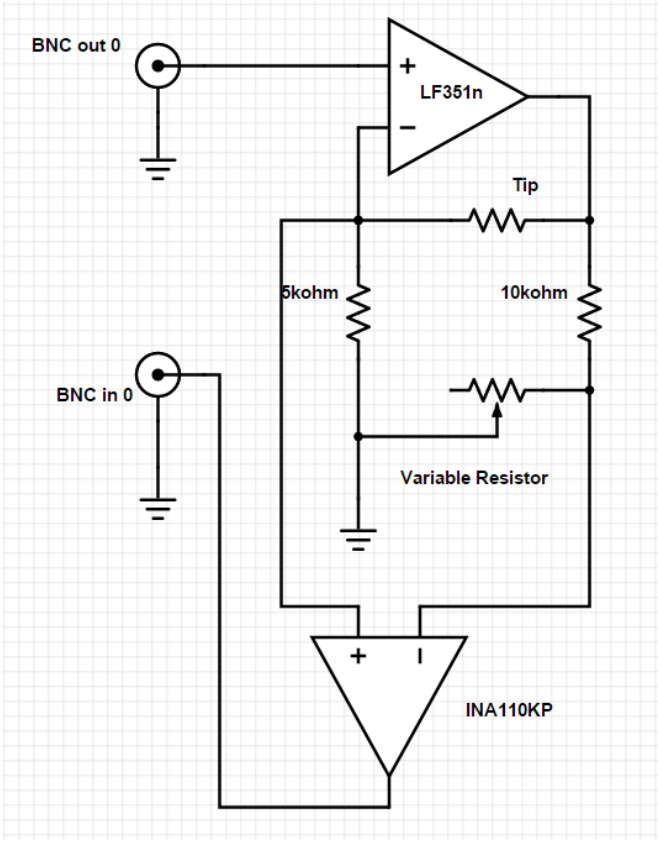

Figure 4-8 Electrical schematic of constant current mode and constant temperature mode.

4.4.4 Constant temperature mode

In constant temperature mode, the tip temperature is always kept as a constant during the scanning, and the contrast of localized thermal properties is represented by the extra heating power consumption at the tip. The circuitry of constant temperature mode is exactly the same as the constant current mode one. The only difference between the measurements of two modes is the operation procedure. In constant temperature method, the voltage output at $\mathrm{BNC}_{\mathrm{out}\,0}$ channel (V_{out}) is not kept as a constant, instead the output voltage keeps changing to ensure the thermal signal at $\mathrm{BNC}_{\mathrm{in}\,0}$ (V_{in}) stays unchanged. As long as V_{in} kept constant, the tip resistance is a constant, and so is the tip temperature.

4.5 Calibration and Measurement Results

4.5.1 Resistance calibration

As discussed earlier, it is necessary to perform the resistance calibration to find out the suitable range of working voltage and prevent unnecessary damage due to overheating. Figure 4-9 shows a resistance calibration result. In the calibration experiment, Keithley 224 Source Meter is used as constant current source and controls the current flow through the thermal probe. A Keithley 2000 digital multimeter (DMM) is used for the voltage measurement across the probe. From the Figure 4-9, a turnaround point shows around 2.2mA and with a tip resistance about 3.5kΩ. When the current goes over 2.2mA, the tip resistance drops as the heating power increases, which indicates the resistance no longer increases with the temperature. Normally, the power at this turnaround point is set as the maximum power limit of the probe during the measurement.

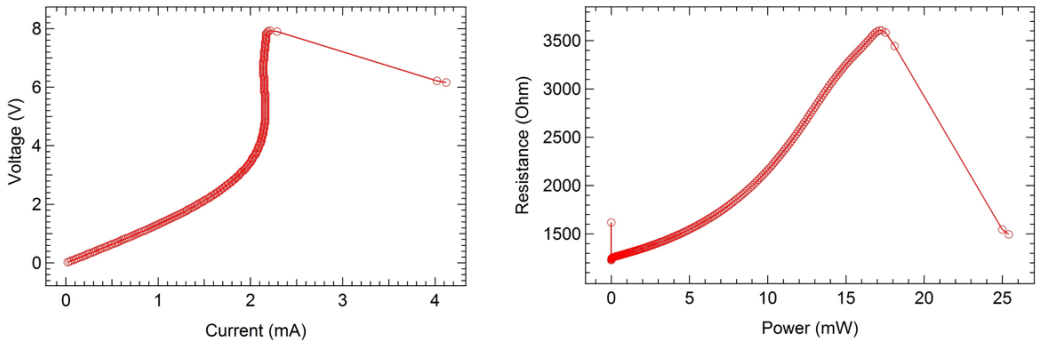

Figure 4-9 Resistance calibration of thermal probe using current source.

For the sake of convenience, a similar calibration procedure is developed using the AFM controller with the circuit design shown in Figure 4-3. Instead of accurate current control, voltage control is

chosen for the calibration process. Considering a long time heating with a high voltage could permanently damage the probe, a voltage sweep procedure is developed to heat the probe with different voltages at a very fast rate. Figure 4-10 shows a calibration result of thermal probe using this voltage sweep method. In that experiment, the voltage is swept from 0V to 10V and back to 0V again, and the whole process takes only 0.2 second. In Figure 4-10, measured tip resistance is shown as y-axis and time is shown as x- axis. The voltage at each point can be obtained using the timing and voltage sweep profile. Two resistance turnaround points show up around 80 ms and 120 ms, as shown in Figure 4-10, which indicates the turnaround voltage is about 8V. This result is consistent with previous measurement using constant current source, and the calibration process itself is much faster and safer.

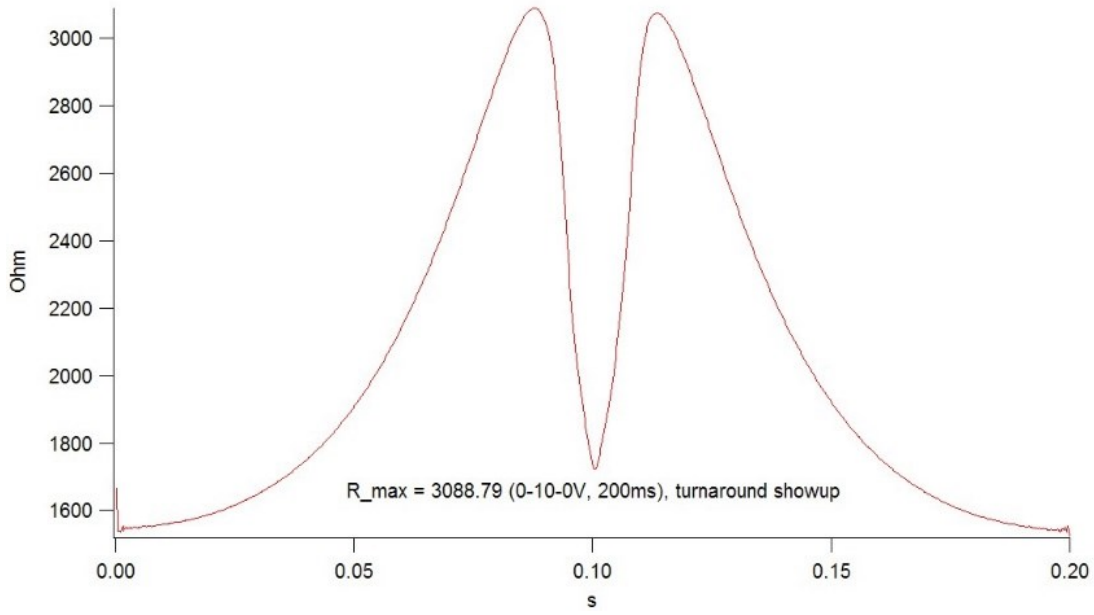

Figure 4-10 Resistance calibration of thermal probe using fast voltage sweep procedure.

4.5.1 Temperature calibration

The resistance – tip temperature calibration at the tip is very important and challenging, as mentioned in Section 4.3.2. As shown in Figure 4-11(A), an experimental setup is designed for the resistance-temperature relationship measurement. A small heater (Polyheater, Asylum Research) is used in this experiment to control the environment temperature, and a Keithley 2000 multimeter is used to measure the resistance of the probe. The calibration process is carried out in following steps:

(1) Engage the probe to a bare silicon wafer clamped on the heater

(2) Set a temperature for the heater

(3) Wait for temperature to be stable

(4) Measure the resistance of the probe using Keithley 2000 meter

(5) Move to next temperature, and repeat steps (2) ~ (4)

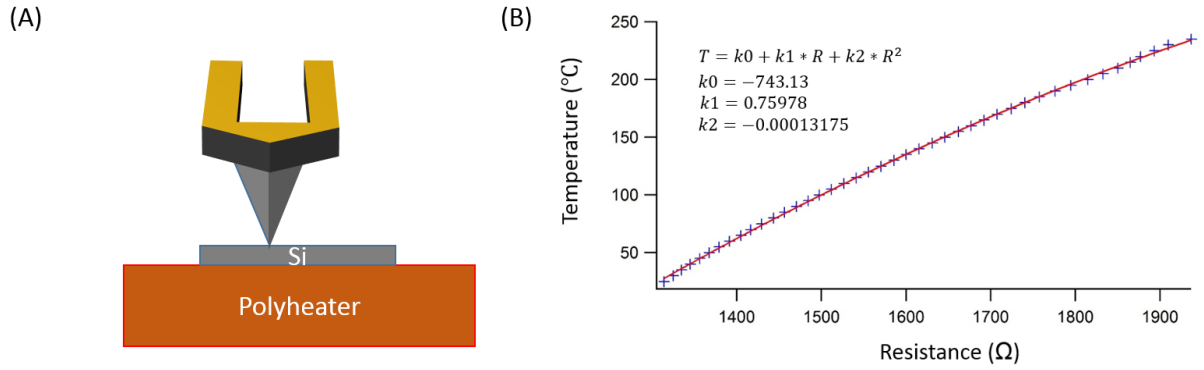

Figure 4-11 Temperature calibration of thermal probe; (A) the experiment setup; and (B) the calibrated R-T curve.

The temperature calibration result is shown in Figure 4-11(B), where it is observed that the resistance and tip temperature almost varies linearly with each other. In this calibration process, it is worth noting that the temperature is measured by a thermocouple embedded inside the heater, and there could have several degrees difference between this measured value and the actual temperature at the tip. Compared to other calibration method, such as Raman spectroscopy, this method is simple, convenient and inexpensive. The major drawback of this method is the low maximum temperature limit. Due to the temperature limitation of the heater and probe holder, the calibration temperature cannot go beyond 250℃.

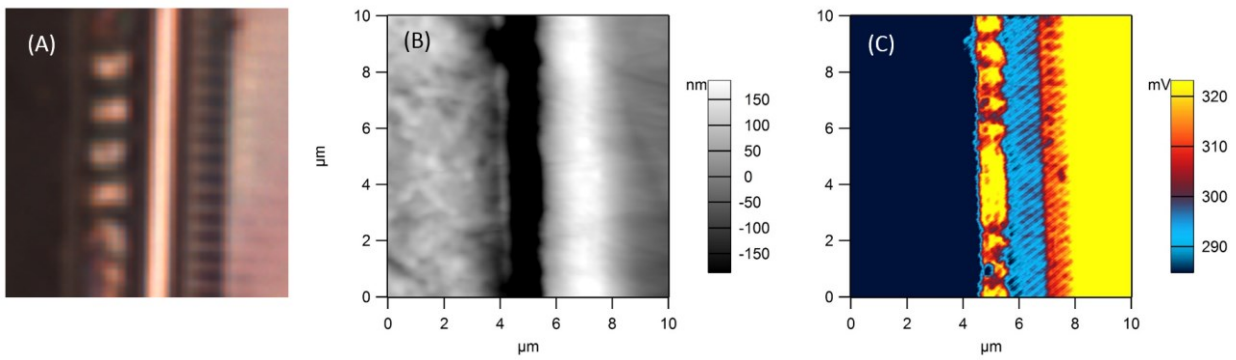

Figure 4-12 Localized thermal conductivity measurement of a SDRAM chip: (A) optical image, (B) height mapping, (C) thermal mapping.

4.5.2 Thermal conductivity contrast measurement on a SDRAM chip

Figure 4-12 shows SThM mapping results on the cross-section of a SDRAM chip using constant current mode. An optical microscopy image of the sample (not the exactly location for SThM) is shown in Figure 4-12(A). It is clear that, the sample contains multiple materials and interfaces. The dark area on the left is the plastic electronic packing materials, and the bright dots are the

cross-section of copper wires. On the right, the bright area shows the single crystal silicon substrate, and the grating like memory cell structures show on the left edge of silicon area. In Figure 4-12(B), none of those details shown in the optical image is observed in the height image, but, in the thermal image shown in the Figure 4-12(C), most of those structures are revealed and can be differentiated by colors. According to the circuit in Figure 4-8, higher voltage (warm color) indicates lower resistance, lower tip temperature, and therefore higher thermal conductivity. The result is reasonable: the silicon and copper area show warmer color and higher thermal conductivity, and the plastic packaging area shows cold color and lower thermal conductivity. The fine memory cell structure is observable in the thermal image but with limited resolution. In Figure 4-13, at a reduced scanning size of 5 μm, the memory unit cells are clearly shown in the thermal image with a much higher resolution.

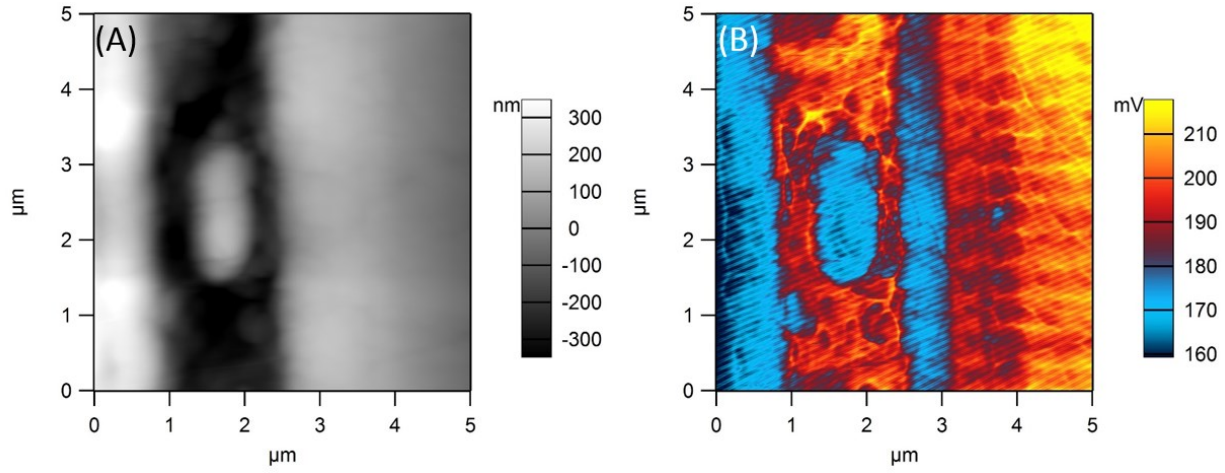

Figure 4-13 SThM images showing the memory unit cells of a SDRAM chip: (A) height mapping, (B) thermal mapping.

4.5.3 Scanning parameters

Scanning parameters of SThM measurement, such as scanning rate and scanning direction, could have a large effect on the resulting thermal images. An experiment is developed to trace the origin of artifacts produced in the thermal mapping. Two different silicon gratings are used as standard samples. These samples are made of single crystal silicon, and all features should have the same thermal conductivity. Ideally, there should be no thermal contrast origins from the thermal conductivity difference.

In Figure 4-13(A), however, color difference shows clearly between the bump and pit area in the thermal mapping. The color bar is adjusted that warmer colors indicate higher tip temperature. This contrast is purely due to the height difference, as discussed earlier in Section 4.3.1. The tip temperature at the bottom of the pit is lower due to increased convection heat transfer path. It is noted that the average tip temperature along each horizontal scan line increases from the bottom to the top of the image. This is because the image was scanned from bottom to the top, and the whole area was heated up gradually due to the continuous thermal scanning.

Similarly, in Figure 4-13(B), the scan direction was from top to the bottom. So the thermal drifting direction is opposite to Figure 4-13(A). Another artifact shows up inside Figure 4-13(B): right side of the hill shows higher tip temperature than the left side. This is because the tip scanning direction in each horizontal scan line is from left to right. In this case, less pressure is exerted between the tip and sample when the tip scans to the right side of the hill. Therefore, the right side should have a higher tip-sample resistance and also a higher tip-temperature than the left side.

In order to reduce similar artifacts in future experiments, several rules could be applied: (1) samples should be as flat as possible to minimize the cross-talk with surface topography; (2)

cooling time of the probe and the sample should be added to the scanning process to minimize the thermal drift effect.

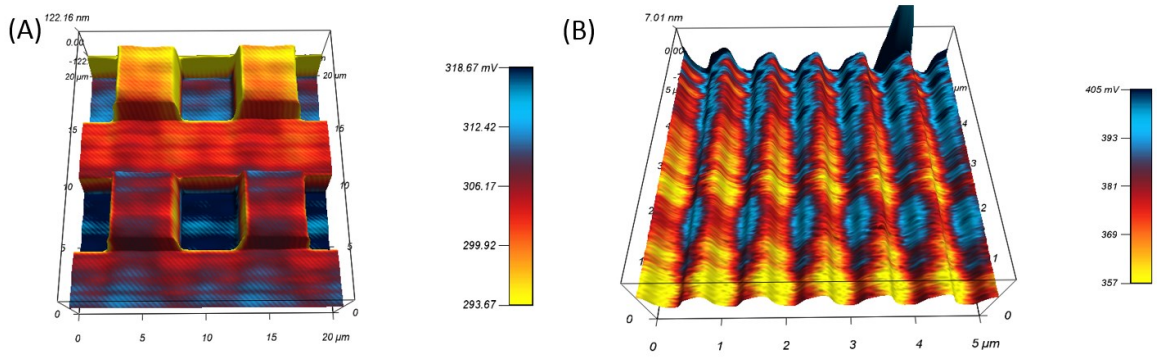

Figure 4-14 Scanning thermal microscopy of silicon gratings; (A) 5 µm square pattern; and (B) 500 nm grating.

4.6 Conclusion

In this chapter, preliminary work on instrumentation development of nanoscale thermoelectric measurement instrumentation has been carried out. The work is mainly focused on the development of localized thermal conductivity measurement:

1) Four different measurement modes and electronic circuits have been developed for local thermal conductivity measurement.
2) Calibration procedures of the thermal probe has been studied, including *I-V* (current-voltage), *P-R* (power-resistance) and *R-T* (resistance-temperature) relationship.
3) Localized thermal conductivity measurement has been carried out on different sample, such as single point measurement on glass, thermal mapping on gold pattern and memory

chip. All the results reveal some levels of the contrast from thermal properties difference rather than purely contributed from height difference.

Further improvements on localized thermal conductivity mapping can be achieved through optimization of scanning parameters, such as scanning rate and probe cooling time. Quantitative measurement of localized the thermal properties still requires more work, such as tip-sample heat transfer mechanism analysis and modeling. From a broader perspective, there are two main directions on nanoscale thermoelectric measurement worth more attention: One is applying those developed tools in the existing nanocomposite thermoelectric materials systems. The other one is developing reliable measurement procedures for localized Seebeck measurement and quantitative measurement of local thermal and electrical transport properties.

Chapter 5 Synthesis Strategies for $Na_xCo_2O_4$ Thermoelectric Oxide

5.1 Overview of $Na_xCo_2O_4$

Due to the high thermal and chemical stability, ceramic oxide materials have the potential for high temperature power generation applications. However, traditional thermoelectric theory considers oxides as poor thermoelectric materials due to their low carrier mobility. The emergence of a new transition-metal oxide, $NaCo_2O_4$ with unexpected good thermoelectric properties reported by Terasaki in 1997 [37] challenged this traditional point of view. As shown in Figure 5-1, $NaCo_2O_4$ has a hexagonal layered structure with edge-sharing 2D triangle CoO_2 sheets and Na layers alternately stacked along c-axis [75].

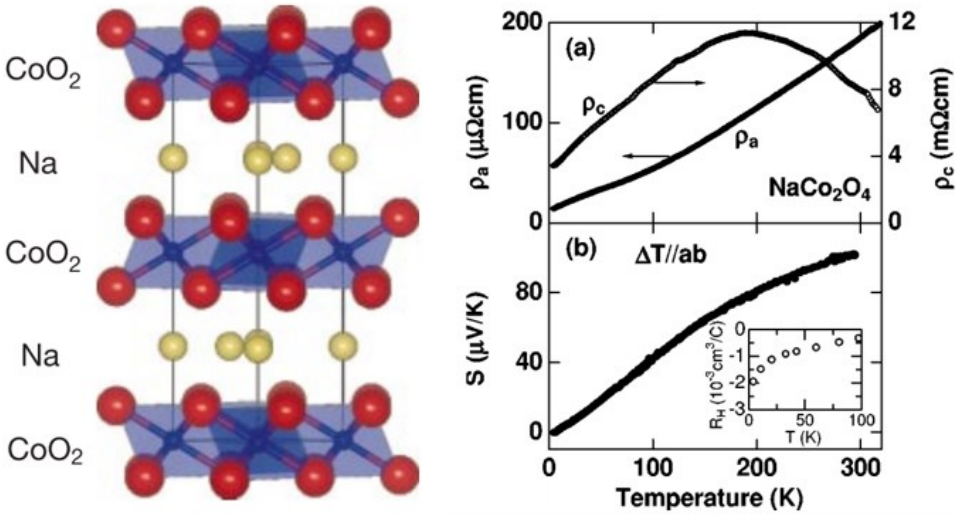

Figure 5-1 Structure and electrical properties of single crystal $NaCo_2O_4$.

It was discovered that the in plane resistivity of single crystal $NaCo_2O_4$ is as low as 0.2 mΩ·cm and its Seebeck coefficient of 100 μV/K is pretty good as well. Although the carrier mobility is quite low (about 13 cm^2/Vs), the power factor at 300K is 50 W/mK^2, and this is even larger than

that of Bi_2Te_3, which is about 40 W/mK^2 at 300K. The electrons in CoO_2 layer are localized and confined due to the strong electron interaction, which is likely of the reason for low metallic electrical resistivity and large enhanced Seebeck coefficient. The low thermal conductivity in the single crystal, measured to be around 5 W/mK [39], is believed to be due to the randomly distributed sodium ion between the CoO_2 layers. The sodium vacancies are acting as phonon-point defect to scatter the phonons. In 2001, the *ZT* of $NaCo_2O_4$ single crystal is found to be 1.2 at 800K [39]. This is still the record ZT for the thermoelectric oxides materials today.

While it is very difficult and time consuming to grow large $NaCo_2O_4$ single crystal for practical thermoelectric applications, polycrystalline $NaCo_2O_4$ can be easily fabricated in large quantity using solid state reactions [76]. However, because of the structure anisotropy and grain boundaries, the thermoelectric properties of polycrystalline $Na_xCo_2O_4$ is not as good as single crystals. The electrical resistivity of polycrystalline samples processed by traditional solid state reaction is about ten times larger than single crystal value at room temperature. As a result the power factor is much smaller, and *ZT* is only 0.2 at around 1000K in most reports.

5.2 Strategies for Synthesis $Na_xCo_2O_4$

In order to improve the thermoelectric properties of $Na_xCo_2O_4$, two strategies have been used: composition modification and structure modification.

5.2.1 Composition modification:

Sodium composition is the first choice for composition modification, since it can be changed without largely altering the crystal structure. However, it is not easy to precisely control the sodium composition because of the volatility of sodium at high temperature [76]. A systematical low

temperature study shows that the increased Na composition will monotonously increase the Seebeck coefficient without changing of the electrical and thermal properties significantly.

Doping with other elements is another popular option for enhancing the thermoelectric properties. Doping of different elements for both Na site and Co site have been extensively researched [31, 38, 77], and it was found out that partial substitution of Cu into Co site can effectively enhance the Seebeck coefficient and *ZT* [31].

5.2.2 Structure modification:

Grain size reduction

Grain size reduction is a widely accepted strategy for thermoelectric properties enhancement. It is believed that fine grain structure will effectively reduce the thermal conductivity without compromising the electrical conductivity much. For example, bulk $La_{1-x}Sr_xCoO_3$ thermoelectric material fabricated from nanowires by high pressure cold press technique shows very low thermal conductivity of 0.35 W/mK, and finally leads to a higher $ZT = 0.18$ at room temperature [66], compared to typical value of 0.1. However, this strategy would be difficult to implement for high temperature materials, since the grain size tends to grow at elevate temperatures.

Texturing

Texturing is a popular structure modification method for anisotropic thermoelectric materials. The electrically favored direction often shows higher power factor, and thus better thermoelectric properties. To certain extent, a single crystal could be considered as a perfectly textured polycrystalline material. So it is feasible to reproduce the high *ZT* of the single crystal through texturing of the polycrystalline materials. Much research has been carried out for highly textured

$Na_xCo_2O_4$, typically using a hot press technique for extended period of time [78]. A reactive template grain growth (RTGG) technique was reported to be very effective in obtaining highly textured polycrystalline samples as well. However, even the textured polycrystalline sample has highly anisotropic structure similar to the single crystal, the performance is still much lower [79]. This may be due to the sodium and oxygen levels inside the crystal. If these factors can be managed and controlled during the processing, it is believed that performance comparable to single crystal can be achieved in polycrystals.

5.2.3 Proposed methodology:

In this thesis, structure modification is the main focus for the study of $Na_xCo_2O_4$. Both solid state methods and solution based methods have been explored to synthesize different structures of $Na_xCo_2O_4$ thermoelectric oxides:

1) A systematic study of sodium composition has been carried out first in order to determine the best x value in $Na_xCo_2O_4$. A study of anisotropy has also been performed to see how the texture could affect the thermoelectric properties.
2) Ball-milling method has been chosen to fabricate the nanostructured materials of $Na_xCo_2O_4$.
3) Sol-gel based Electrospinning method has been developed to fabricate $Na_xCo_2O_4$ nanofibers and powders with nano grain size.
4) A core-shell structured $Na_xCo_2O_4$ nanocomposite has been designed to lower the thermal conductivity.
5) Solution based Combustion synthesis of $Na_xCo_2O_4$ have been explored to create fine nanopowder and highly textured bulk materials.

5.3 Characterization of $Na_xCo_2O_4$

5.3.1 Structure characterization

Lattice structure

X-ray diffraction (XRD, Bruker D8) was used to characterize the crystalline structure of $Na_xCo_2O_4$ powders and pellets.

Microstructure

Scanning Electron Microscopy (SEM) was used to characterize the particle size and shape of powders and grain size and microstructure of sintered pellets.

5.3.2 Thermal transport properties characterization

Thermal conductivity of sintered sample κ can be calculated using following equation:

$$\kappa(T) = c_p(T)\alpha(T)\rho_d \tag{5.1}$$

Here, c_p is specific heat capacity, α is thermal diffusivity, and ρ_d is density. These three parameter can be measurement through separated experiments.

Heat capacity measurement

Specific heat capacity c_p is the amount of heat that sample needs to absorb to raise its temperature by one degree. It can be measured by differential scanning calorimetry (DSC) method using standard sapphire sample as a reference. The detail of this method can be found in ASTM E1269-11 standards.

Thermal diffusivity measurement

Thermal diffusivity was measured using laser flash method [80], as shown in Figure 6-3, by shooting a short heat pulse on the front surface of a uniform thin sample and measuring the temperature on the back side. The thermal diffusivity can be calculated through following equation:

$$\alpha = -\frac{\ln(1/4)h^2}{\pi^2 t_{1/2}} \tag{5.2}$$

where h is the thickness of the sample and $t_{1/2}$ is the time it takes to raise the back side temperature to the half of the maximum equilibrium temperature after shooting the heat pulse.

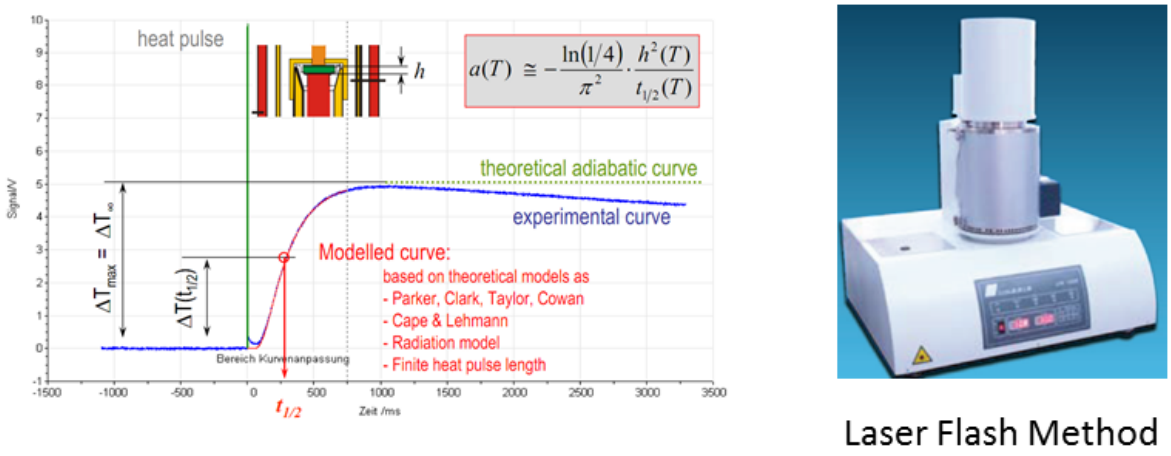

Figure 5-2 Laser flash setup, measurement curve and actual photo of the instrument.

Density measurement

Density of the sample was measured using the Archimedes method and normally it is considered as temperature independent. Figure 6-4 is a home-designed setup to measure density using Archimedes method. By measuring the dry weight m_{dry} and wet weight m_{wet} inside the ethanol, the density of sample ρ_d can be calculated:

$$\rho_d = \frac{m_{dry}}{m_{dry} - m_{wet}} \rho_{ethanol} \ , \tag{5.3}$$

where $\rho_{ethanol}$ is the density of ethanol.

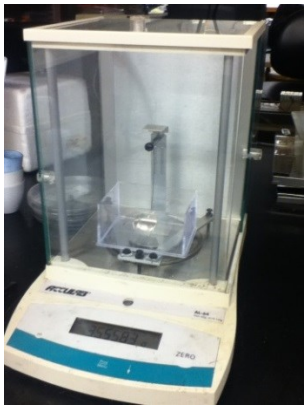

Figure 5-3 Setup for density measurement using Archimedes method.

5.3.3 Electrical transport properties characterization

The Seebeck coefficient and electrical resistivity were measured using ZEM3 and Custom made system (see Chapter 2). The sample was cut into a rectangular bar of 2x2x10 mm using a diamond saw.

Chapter 6 $Na_xCo_2O_4$ Synthesis by Solid State Method

6.1 Introduction

Solid state reaction (SSR) is a traditional method to fabricate ceramics. The reaction formula is usually very simple, and involves high temperature processing. SSR is the most favorable method for industrial ceramic materials synthesis due to its good repeatability and scale-up ability. From research perspective, SSR is also convenient choice to start on a new materials. The involved equipment is simple, usually a furnace and a crucible. Samples fabricated by this method can easily obtain high crystallinity and purity. Based on these consideration, SSR was chosen as the fabrication method of $Na_xCo_2O_4$.

In this chapter, three main experiments will be described: (1) optimization of sodium composition; (2) characterization of anisotropy thermoelectric properties; (3) nanostructuring of $Na_xCo_2O_4$ through Ball milling.

6.2 Synthesis Process

6.2.1 Raw materials preparation

The raw material of $Na_xCo_2O_4$ was fabricated by solid state reaction. The process is very simple and only involves one step, as shown in Figure 6-1. Cobalt oxide and sodium carbonate with a weight ratio according to the chemical formula of target $Na_xCo_2O_4$ was mixed together and put into a large crucible. Then the mixed powder was annealed in a high temperature furnace for 12 hours at 800℃. The rapid annealing process was adopted to prevent the evaporation loss of sodium. Normally the furnace is heated using its maximum speed and it takes about 10 minutes to reach 800℃; the ramping rate is set at 100℃/min.

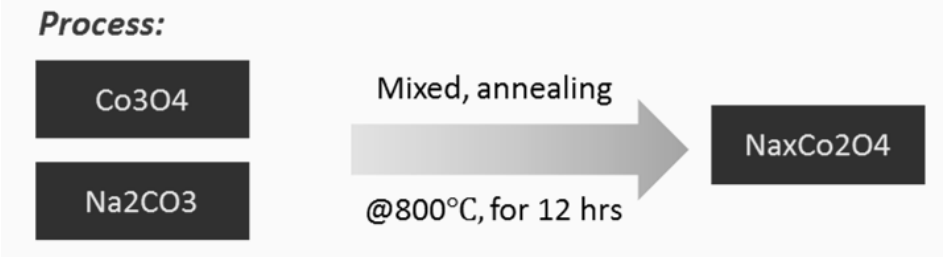

Figure 6-1 Solid state reaction process.

6.2.2 Spark plasma sintering

Dense bulk material is needed for thermoelectric properties measurement and industrial applications, so the fabricated loosed powders have to be consolidated into hard and dense pellets. Spark plasma sintering (SPS) is a relative new method for creating dense bulk samples, compared to common consolidation methods such as cold press and hot press.

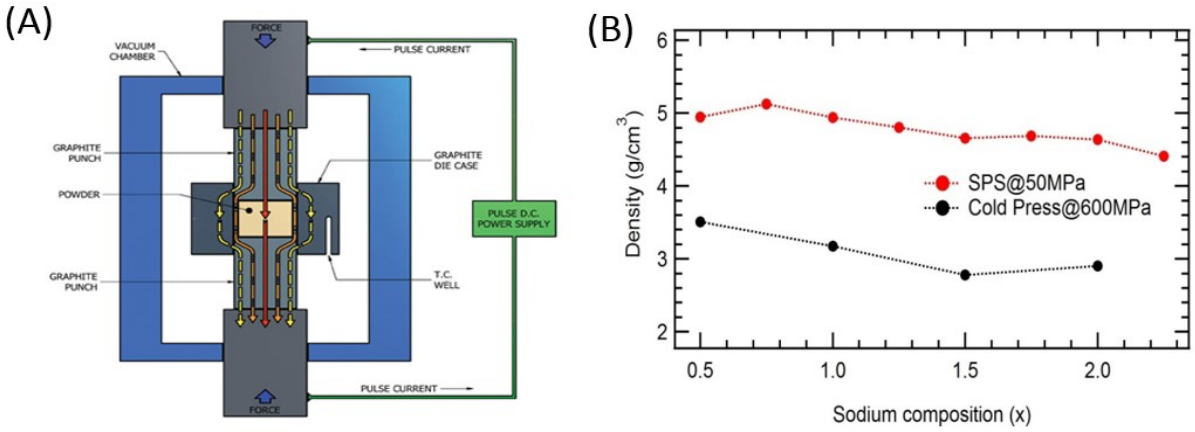

Figure 6-2 Schematic of SPS process; (A) schematic of a SPS system; (B) comparison of density between SPS and cold press pellets with different sodium contents.

SPS is an efficient way to prevent grain growth during consolidation process, because materials are sintered in a very short time. Figure 6-2 shows a schematic of SPS system. The powder is pre-

loaded in a graphite die and then placed between two graphite punch head. Normally the pressure applied to the die is about 50 MPa. When sintering starts, a DC pulsing current about 500~800 A is passing through the die and heating up the samples very quickly. The heating rate can be faster than 100℃/min. Similar as hot press, the sintered pellets usually achieve a higher density than cold pressure method. Figure 6-2 shows a comparison of density between SPS sintered and cold pressed pellets of $Na_xCo_2O_4$ with different sodium contents. The SPS sintered sample are all around 100% theoretical density, while cold press is only around 70 percent with a compressing pressure that is 10 times higher than that was used for SPS.

6.3 Optimization of Sodium Composition

A group of $Na_xCo_2O_4$ samples with different sodium composition (x = 0.5 ~2.25) was synthesized by SSR as discussed in **Section 6.2**.

6.3.1 Structural analysis

The crystal structures of $Na_xCo_2O_4$ powders with different sodium composition are shown in Figure 6-3. Most samples show their major phases as $Na_xCo_2O_4$, though there are tiny amount of impurities of Co_3O_4 or CoO. The sample with x=2 is slightly different from other samples, showing a relatively higher portion of CoO.

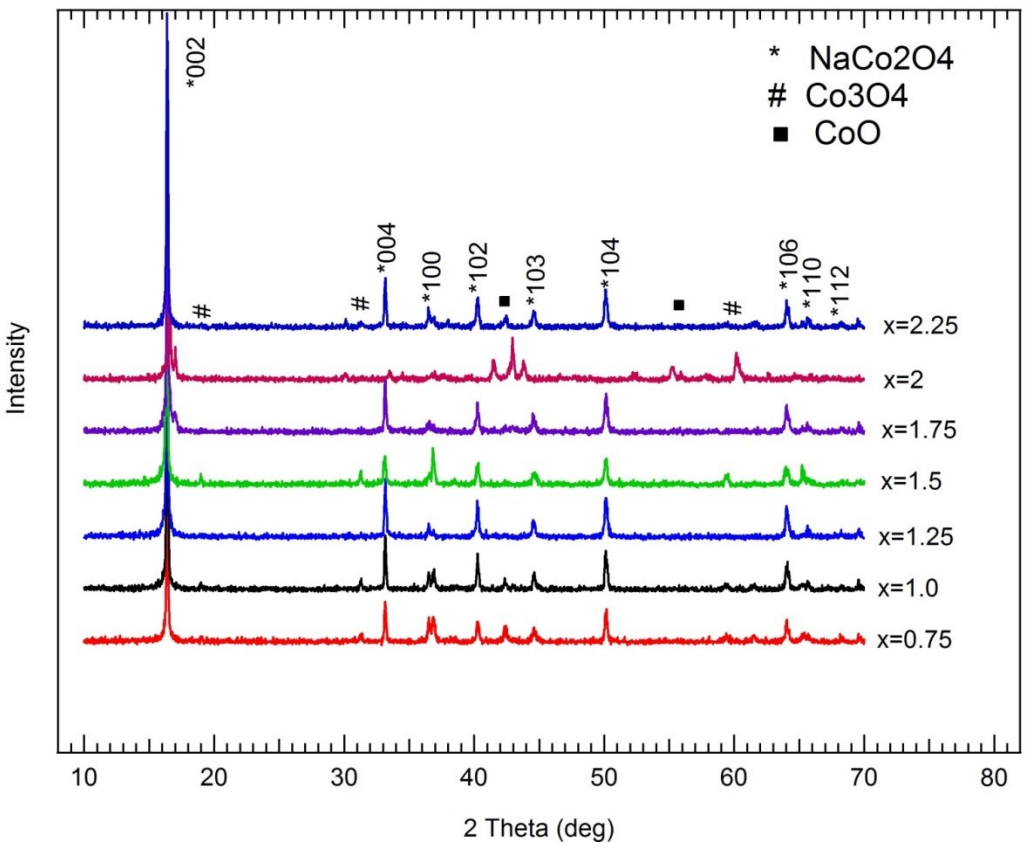

Figure 6-3 XRD of solid state reaction samples with different sodium compositions.

6.3.2 Thermoelectric properties analysis

The thermal and electrical transport properties of $Na_xCo_2O_4$ with different sodium compositions are measured and shown in Figure 6-4. The thermal conductivity decreases when the sodium composition increases, though there is no obvious decrease when $x > 1$. The electrical conductivity increases as sodium composition increases when $x < 1.5$, and decreases when $x > 1.5$. This leads to an interesting result that the sample with $x=1.5$ has both the lowest thermal conductivity and highest electrical conductivity.

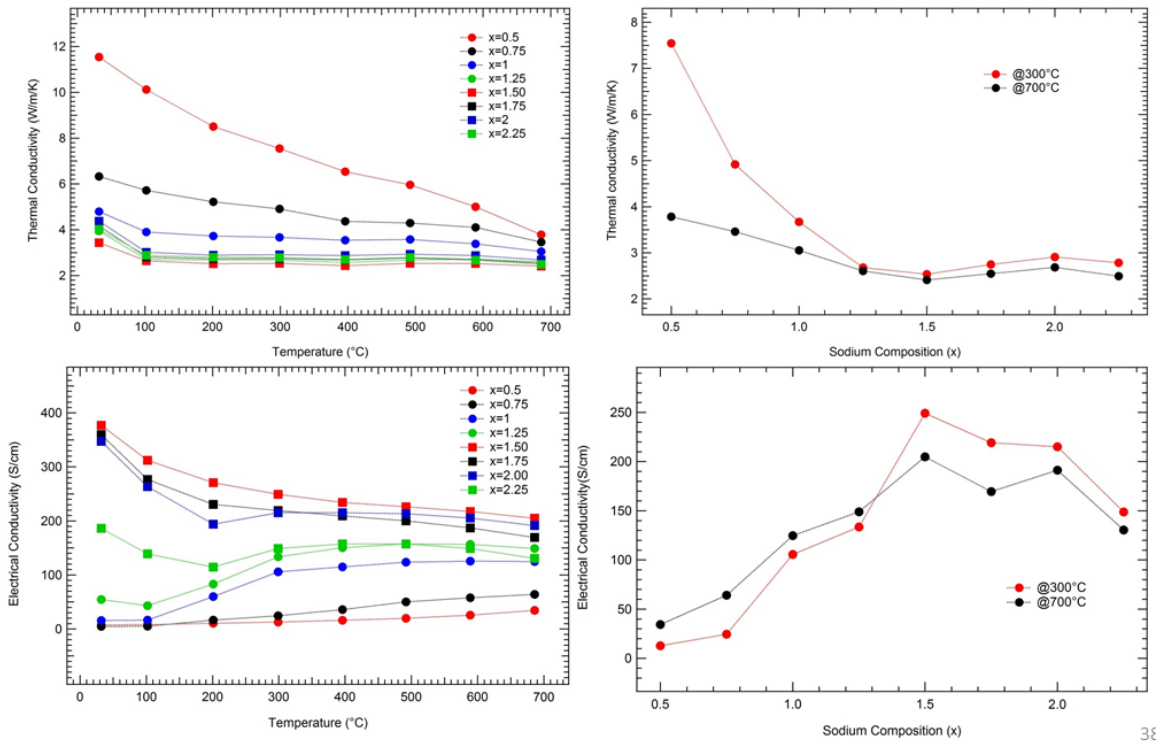

Figure 6-4 Electrical and thermal transport properties of $Na_xCo_2O_4$ with different sodium composition.

The Seebeck coefficient, shown in Figure 6-5, does not change much with sodium composition, and all the samples have the same trend of increased Seebeck coefficient with higher temperature.

6.3.3 Conclusion

As a result, x=1.5 would be the best sodium composition for further investigation, since it has the best properties over the temperature range, which is further demonstrated in the calculated power factors and *ZT* values shown in Figure 6-5.

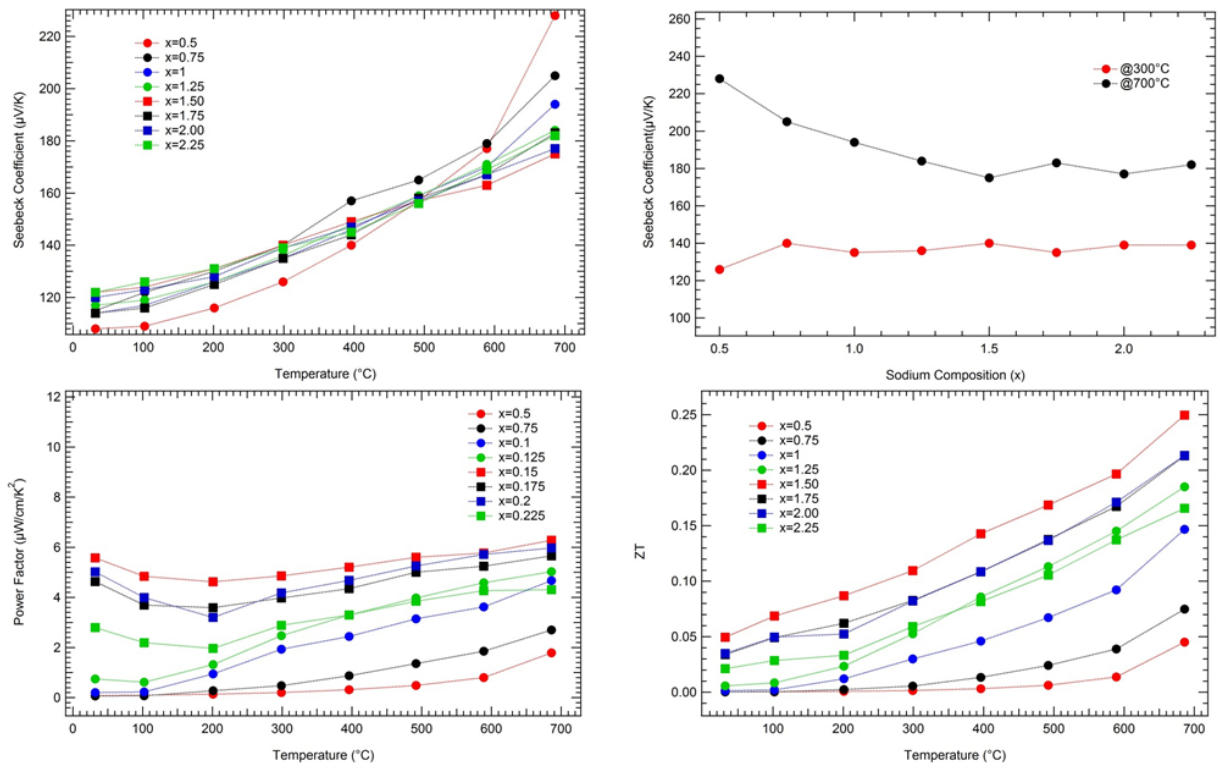

Figure 6-5 Thermoelectric properties of $Na_xCo_2O_4$ with different sodium composition.

6.4 Anisotropic Analysis

$Na_xCo_2O_4$ has layered structure and electrical conductivity measurement shows that there is a large difference between in-plane and out-plane direction, as discussion in Section 5.1. So it is worthwhile to examine the anisotropic thermoelectric properties of the SPS sintered polycrystalline $Na_xCo_2O_4$ samples.

6.4.1 Sample preparation

Figure 6-6 shows how the testing samples were cut from a thick pellet (thickness > 10 mm) for anisotropic measurements. For a textured layer structure, the direction of applied pressure is perpendicular to the layer structure inside the sintered pellet. A and D are cut from the layer

structure perpendicular to the pressure. B and C are cut from the plane that is perpendicular to the top surface. They are used for thermal and electrical measurement in different directions, as shown in Figure 6-6.

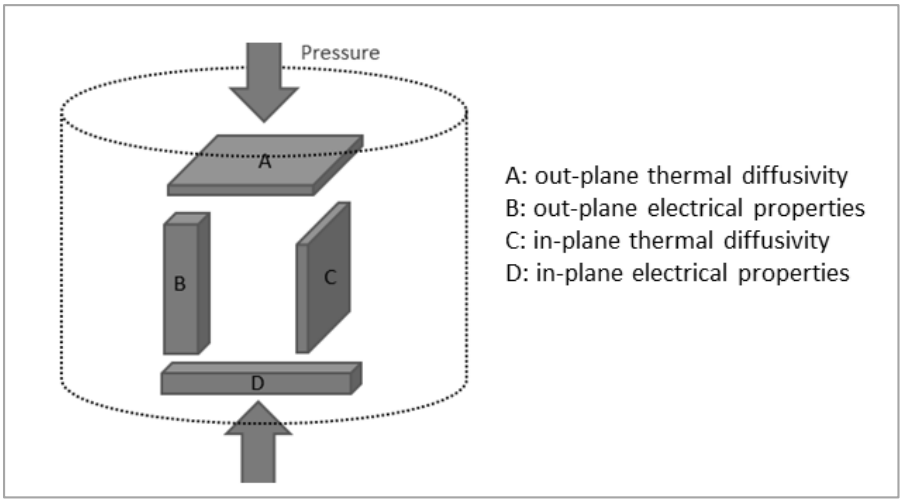

Figure 6-6 Cutting geometry for anisotropic measurement.

Normally for isotropic materials, a thin pellet with a thickness around 1mm is good enough, and only part A and D in the figure are needed. A is used for the thermal diffusivity and D is used for electrical conductivity measurement. But for a textured sample with anisotropic properties, the obtained thermal diffusivity is actually lower than the real value along the direction of electric measurement, and the *ZT* of the sample is overestimated.

6.4.2 Thermoelectric properties analysis

The thermoelectric properties along both directions are measured and shows a large difference, as shown in Figure 6-7. The thermal and electrical conductivities along in-plane direction is higher than out-plane direction as expected. The in-plane Seebeck coefficient is also higher, the reason of which is not clear and need more investigation in the future. As a result, the *ZT* value along in-

plane direction is higher than out-plane direction, and the difference increases with higher temperature, which leads to a conclusion that texture is more important at higher temperature.

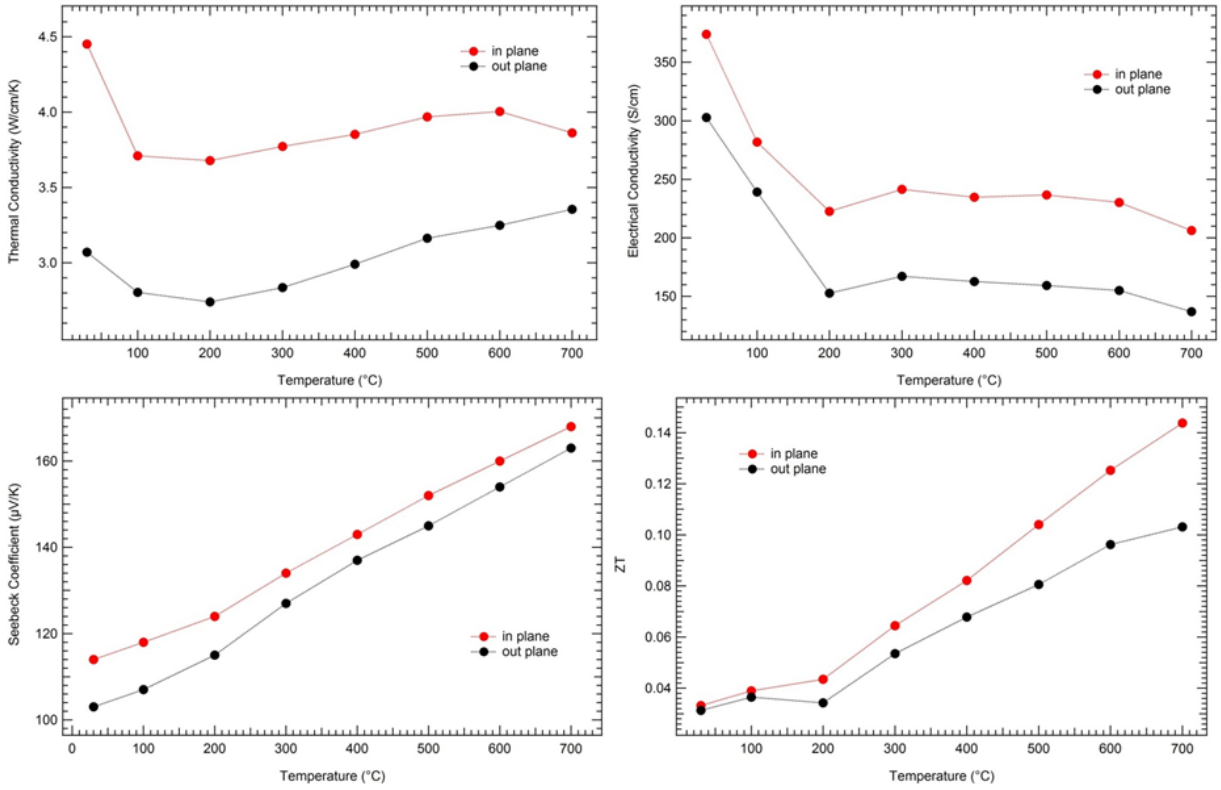

Figure 6-7 Thermoelectric properties in both in-plane and out-plane direction of a SPS sintered $Na_xCo_2O_4$ pellet.

6.5 Nanostructuring by Ball Milling Method

6.5.1 Ball milling process

Figure 6-8 shows the equipment for the ball milling process. $Na_xCo_2O_4$ powder and an alumina ball were put into an alumina vial which is clamped on the shaking arm. The alumina ball grinded the power violently when the arm is shaking at a high speed. To prevent the vial getting too hot,

the process is sectioned into 10-minute periods, and between each period, the vial will have 5 minutes to cooling down.

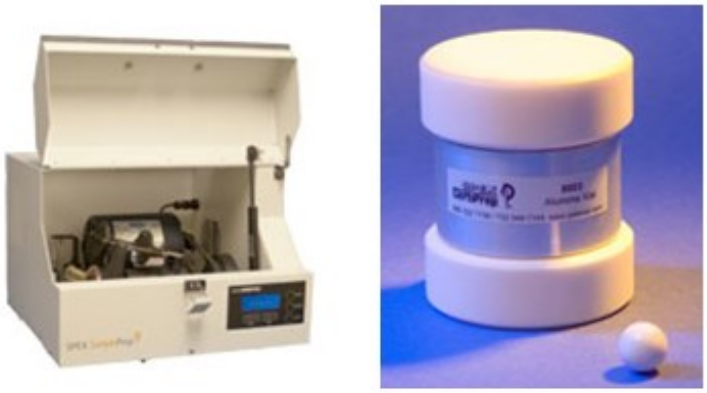

Figure 6-8 Equipment for ball milling process.

6.5.2 Structure of ball milled powder

Figure 6-9 shows that great size reduction has been achieved by 1 hour ball milling. The average particle size is reduced to less than 100 nm. For longer time, it is difficult to see the difference, and it seems that the broken particles tend to aggregate together as the milling time increase.

The XRD of the ball milled powders show wider peaks than those without ball milling, as shown Figure 6-10, which indicates a small average grain size.

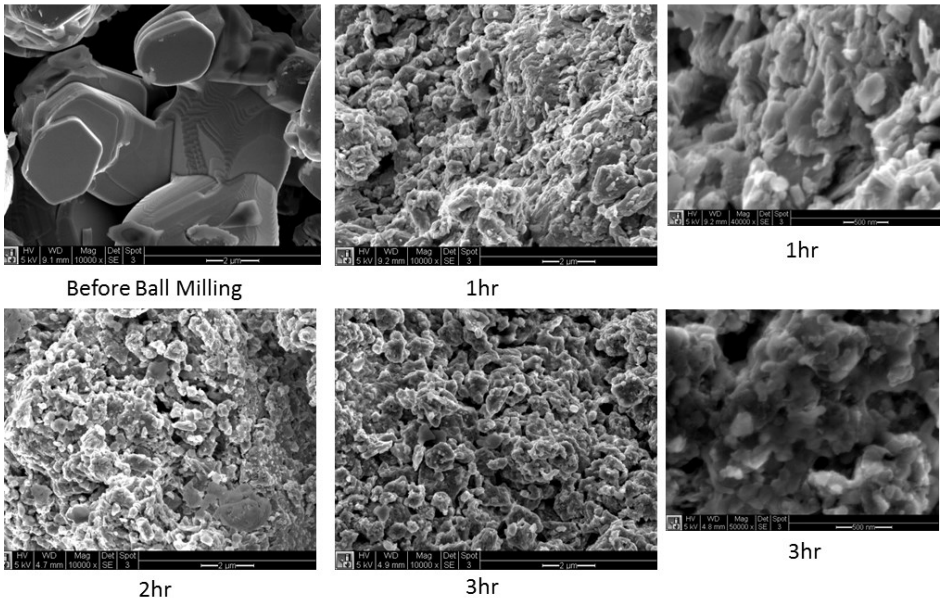

Figure 6-9 SEM of ball milled powders with different ball milling time.

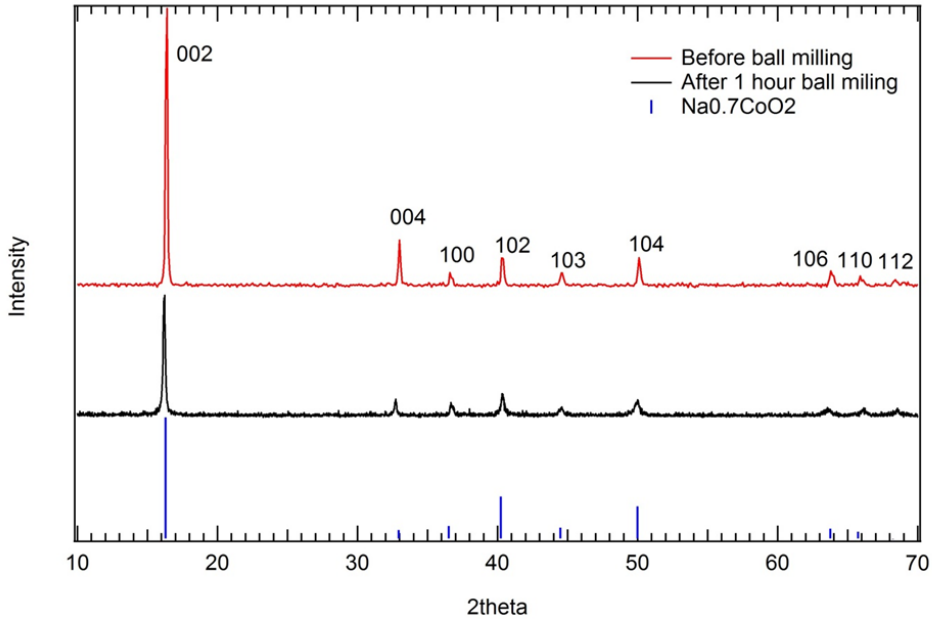

Figure 6-10 XRD of $Na_xCo_2O_4$ powders before and after ball milling.

6.5.3 Thermoelectric properties analysis

Thermoelectric properties of those samples have been examined and shown in Figure 6-11. The electrical conductivity is increased significantly after ball milling, and the thermal conductivity almost stays unchanged. This is unexpected, and a possible reason could be that the nanosize particles grow to micrometer size during the SPS process and form better texture perpendicular to the pressure direction. The Seebeck coefficient is decreased after ball milling process, which usually happen when electrical conductivity is increased.

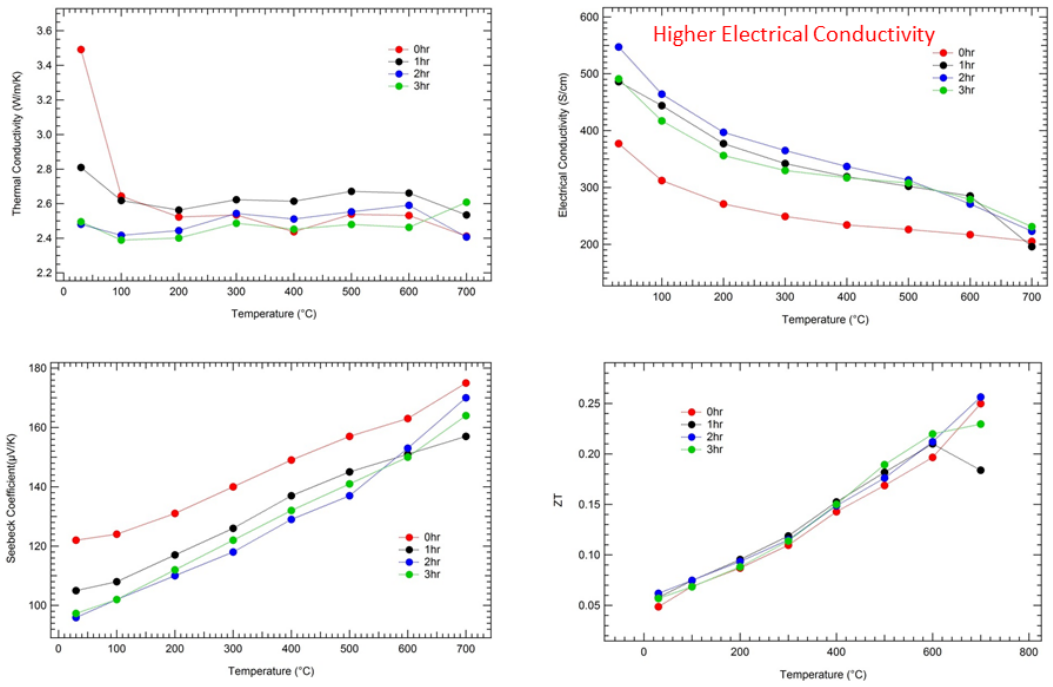

Figure 6-11 Thermoelectric properties of samples with different ball milling time.

In summary, ball milling is very effective in breaking down materials into nano-size. The resulting material is aggregated together like paste rather than loose powder with separated individual particles, and this leads to a high density pellet and better electrical conductivity. Compared to

SSR samples, ball milled samples have better electrical conductivity, similar thermal conductivity and lower Seebeck coefficient, leaving the *ZT* value almost unchanged.

6.6 Conclusion

In this chapter, $Na_xCo_2O_4$ has been successfully fabricated using solid state method. Three experiments have been carried out based on this synthesis method:

1) A systematic study of sodium composition was carried out. It is found that $Na_xCo_2O_4$ reaches its maximum thermoelectric performance when x = 1.5.
2) Anisotropy thermoelectric properties were characterized using a sample synthesized without any special texturing process. The sample shows different performance in difference directions, and the in plane direction show better thermoelectric performance.
3) Ball-milling method is used to successfully break down the materials into nanometer size. Due to the grain growth during the SPS sintering process, no decrease of thermal conductivity is observed, and the electrical conductivity is greatly improved instead.

Chapter 7 $Na_xCo_2O_4$ Synthesis by Solution Based Method

7.1 Introduction

In this chapter, three methods have been studied for the structure modification of $Na_xCo_2O_4$ in the following order: (1) electrospinning method; (2) co-axial Electrospinning; (3) solution base combustion synthesis.

7.2 $Na_xCo_2O_4$ by Electrospinning Method

7.2.1 Introduction to electrospinning

Electrospinning is a versatile technique to fabricate fibers with dimensions down to the nanometer range. A schematic illustration of the electrospinning process is shown in Figure 7-1. A syringe with a metal needle tip is loaded with polymer solution. When a high voltage is applied to the needle tip, the pendent drop of polymer solution at the nozzle will become highly electrified and the induced charges are distributed over the surface of the solution drop. As a result, the drop will bear two major types of forces: the surface tension trying to keep the spherical shape and the Columbic force exerted by the external electrical field trying to drag the drop to the grounded collector. Due to those forces, and also the viscoelastic property of the liquid, the drop will be distorted into a conical object. This conical shape is also known as the Taylor cone [81]. Once the strength of electric field has surpassed a threshold value, the electrostatic forces can overcome the surface tension of the polymer solution and thus force the ejection of a liquid jet from the nozzle. Then this jet was further stretched by the electrostatic force, and forming a long and thin thread. As the liquid jet is continuously elongated and the solvent is evaporated, its diameter can be greatly reduced from hundreds of micrometers to as small as tens of nanometers. Finally, this charged

continuous long nanofiber is deposited on the grounded collector, often randomly oriented as a non-woven mat.

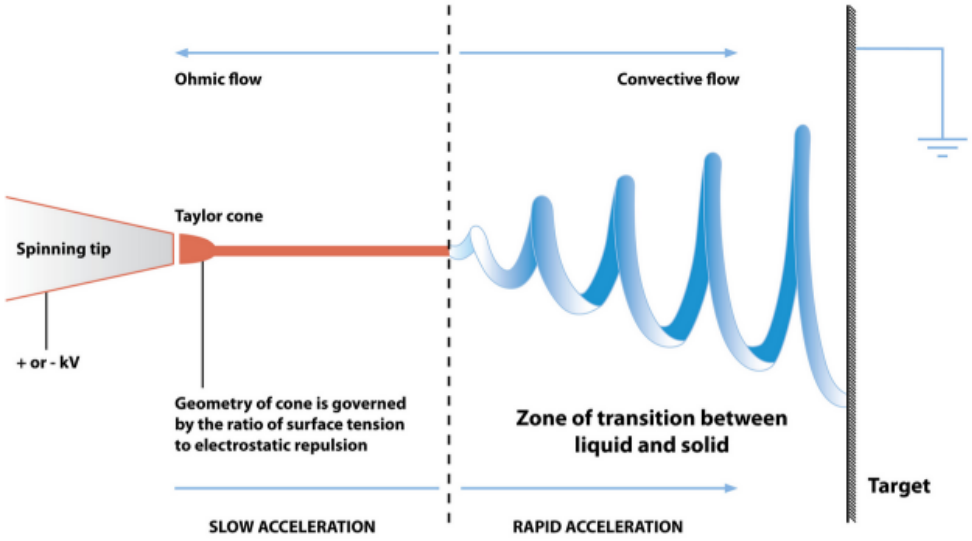

Figure 7-1 Formation process of an electrospun nanofiber from a liquid drop under an electrical field.

A basic setup for electrospinning is shown in Figure 7-2. The electrospinning system consists of three major components: high voltage supply, movable stage and syringe pump. The high voltage supply (Model: ES40P5W, Gamma High Voltage, Inc) can provide a high voltage between 0 ~ 40 kV to the metallic needle. The movable stage, a normal lab jack, can go up and down to adjust the distance between needle tip and its top surface in a range from 0 to 40 cm. The syringe pump (Model: NE-500, New Era Pump System, Inc.) can pump the solution at a speed between 0.73μL/hr ~ 2100mL/hr.

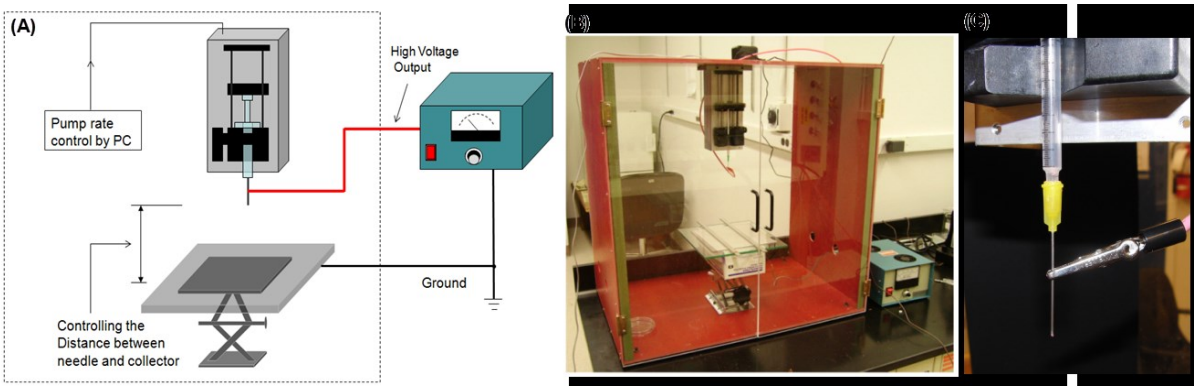

Figure 7-2 Our home-made electrospinning system: (A) a sketch of our electrospinning system; (B) the photo of the real setup; (C) a zoom-up showing the syringe needle connected to the high voltage outlet clip.

7.2.2 Fabrication of $Na_xCo_2O_4$ nanofibers

The fabrication process can be divided into three parts: precursor preparation, electrospinning process, and annealing process, as shown in Figure 7-3. First, $Na_xCo_2O_4$ sol-gel precursor solution is prepared; then electrospinning process is carried out with the precursor, and $Na_xCo_2O_4$/Polymer nanofibers are obtained; and finally, $Na_xCo_2O_4$ ceramic nanofiber is fabricated by the annealing process in air.

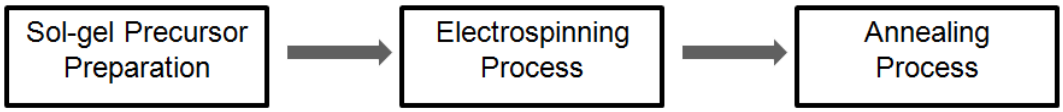

Figure 7-3 Three steps of processing $Na_xCo_2O_4$ nanofibers.

Sol-gel Process

The raw materials used to prepare the sol-gel $Na_xCo_2O_4$ precursor are listed in table 7.1

Table 7-1 Chemicals for $Na_xCo_2O_4$ sol-gel precursor preparation

Chemical Name	Formula	Purity	Company
Cobalt(II) Acetate Tetrahydrate	$(CH_3COOH)_2Co.4H_2O$	Reagent grade	Sigma-aldrich
Sodium Acetate Trihydrate	$(CH_3COOH)Na.3H_2O$	Reagent grade	Mallinckrodt Baker
Polyvinylpyrrolidone(PVP)	$(C_6H_9NO)_n$ Mw=1,300,000 g/mol	Reagent grade	Sigma-aldrich
Methanol	CH_3OH	Reagent grade	Mallinckrodt Baker

Following is the recipe for preparing 10 ml 0.3mol/L $Na_xCo_2O_4$ sol-gel precursor:

- Cobalt (II) acetate tetrahydrate (0.006 mol) is dissolved into 5 ml distilled water in a 20ml vial, stirred or sonicated until a homogenous pink solution is formed.
- Sodium acetate trihydrate (0.0033mol, 10% more than stoichiometry quantity) is dissolved into cobalt acetate solution, stirred or sonicated until totally dissolved. The color of the solution will become dark red.
- 5ml methanol is added to the solution, stirred or sonicated until homogenous solution is formed.
- 0.8g Polyvinylpyrrolidone (PVP) is added into the solution to achieve a PVP concentration of 8% (0.08 g/ml), stirred or sonicated until PVP is totally dissolved, and a dark red and viscous solution is formed.

Electrospinning process

The $Na_xCo_2O_4$ nanofiber is electrospun using the device described in Section 7.2.1. The electrospinning process is carried out in following steps:

- The prepared $Na_xCo_2O_4$ sol-gel precursor is loaded into a plastic syringe with a metal needle tip.

- Preset the pumping rate. Normally the pumping rate for 0.3 M $Na_xCo_2O_4$ sol-gel precursor is 0.2 ml/hr.
- The high voltage clip is connected to the needle, and the metal collector underneath is connected to the ground. The distance between needle tip and collector is adjusted to 15 cm by moving up or down of the stage.
- Start the syringe pump, turn on the power of high voltage supply and wait until the first drop of liquid shows up at the tip of needle. Then start to increase the high voltage slowly and carefully, until the liquid is shaped into a cone shape, and some fibers are stretched out.

Annealing process

The as-spun $Na_xCo_2O_4$ nanofibers are followed by a two-step annealing process:

- Evaporate the solvent inside nanofibers in the oven (Yamato DX400) at 80 ℃ for 2 hours ~ 12 hours.
- Preheat the furnace (Carbolite RWF1200) to 750℃, then put the nanofiber sample directly into the furnace, and keep the temperature of 750℃ for 2 hour, and then cool down with the oven naturally to room temperature.

Because the Sodium component can easily evaporate around 400℃, 10% extra sodium is added for compensation of this loss when preparing the solution. In addition, the heating rate of annealing process is also required to be very fast to avoid large amount of sodium loss. So instead of setting a heating rate (highest heating rate 100℃/min), a preheat process was selected for nanofibers annealing.

In this thesis, in order to compare the nanofibers with $Na_xCo_2O_4$ powders processed by conventional solution based method, a normal sol-gel process has also been applied to synthesize $Na_xCo_2O_4$ powders. The sol-gel process is carried out in following steps:

- The sol-gel precursor mentioned in the electrospinning process was baked in the oven at 80℃ for gelation.
- After the gel formed, increase the temperature to 160℃ for two days to get a dry gel.
- Then annealing the nanofibers in the preheat furnace at 750℃ for two hours, and cool down with in the oven.

7.2.2 Microstructure and crystal structure analysis

SEM images of $Na_xCo_2O_4$ fibers before and after annealing process are shown in Figure 7-4. The diameter of nanofiber before annealing is around 200 nm. After annealing, the diameter of nanofiber becomes a little smaller and the surface morphology becomes rougher.

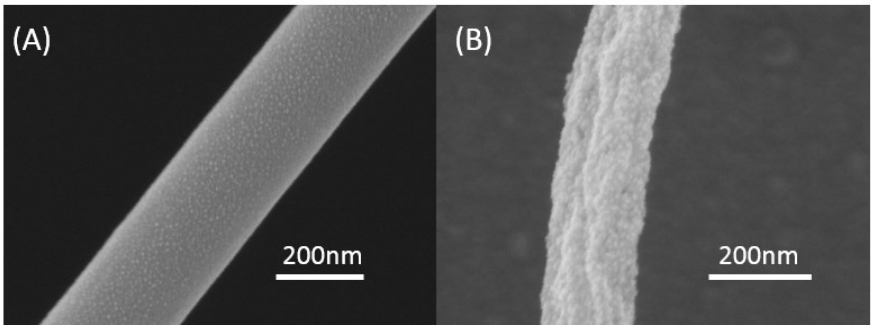

Figure 7-4 SEM images of a electrospun $Na_xCo_2O_4$ nanofiber (A)before annealing (B) after annealing.

In the Transmission Electron Microscopy (TEM) image showing in Figure 7-5, nanosize crystalline structures with a grain size less than 20 nm is observed. Electron diffraction is used to

identify the crystal structure of the nanofiber, and the pattern is consistence with a previous report [82]. But after a careful analysis, the diffraction pattern actually matches the lattice structure of Co_3O_4 rather than $Na_xCo_2O_4$.

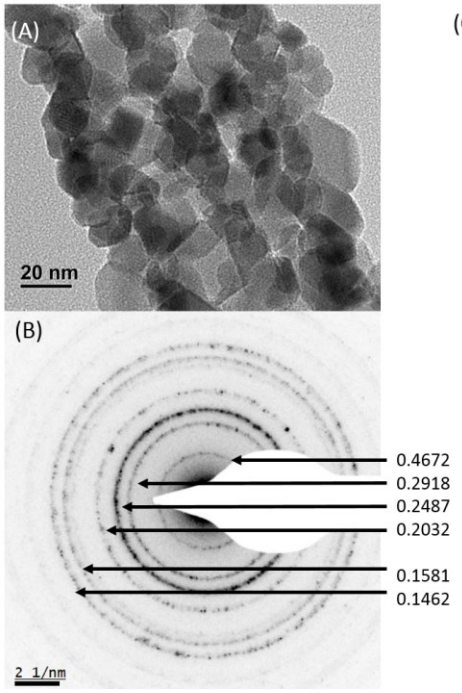

(C) Co3O4

#	d(Å)	I(f)	(hkl)
1	4.6690	20.0	(111)
2	2.8600	40.0	(220)
3	2.4380	100.0	(311)
4	2.3330	12.0	(222)
5	2.0210	25.0	(400)
6	1.6505	12.0	(422)
7	1.5559	35.0	(511)
8	1.4293	45.0	(440)
9	1.2788	6.0	(620)
10	1.2330	12.0	(533)
11	1.2191	8.0	(622)
12	1.1671	4.0	(444)
13	1.1321	4.0	(551)
14	1.0803	8.0	(642)
15	1.0524	16.0	(553)
16	1.0105	8.0	(800)
17	0.9529	6.0	(660)
18	0.9335	16.0	(751)
19	0.9275	6.0	(662)

(D) NaCo2O4

#	d(Å)	I(f)	(hkl)
1	5.4100	100.0	(002)
2	2.7020	13.0	(004)
3	2.4610	17.0	(100)
4	2.2400	45.0	(102)
5	2.0330	17.0	(103)
6	1.8200	45.0	(104)
7	1.4540	25.0	(106)
8	1.4210	25.0	(110)
9	1.3750	13.0	(112)
10	1.3510	3.0	(008)

Figure 7-5 TEM image and electron diffraction pattern of an electrospun $Na_xCo_2O_4$ nanofiber.

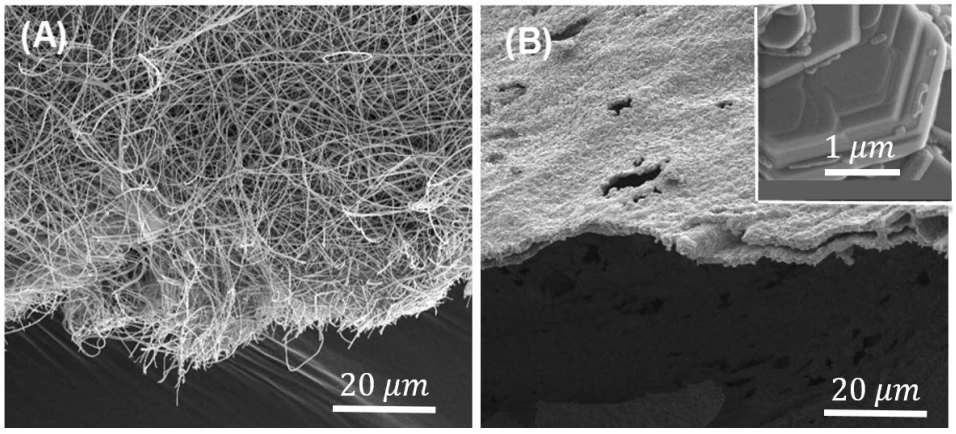

Figure 7-6 SEM images of $NaCo_2O_4$ nanofiber mats before and after annealing.

Unlike the isolated single nanofiber, the fiber mat fabricated by electrospinning mass production has substantial grain growth during the high temperature annealing process, as shown in Figure 7-6. All the grains appear as plate structures with grain size as large as 5μm, and the nanofiber structures before annealing are lost. The crystal phases of fiber mats were confirmed using X-ray diffraction (XRD). As showing in Figure 7-7, the major phase of those nanofibers is $NaCo_2O_4$, with a small amount of Co_3O_4 impurities.

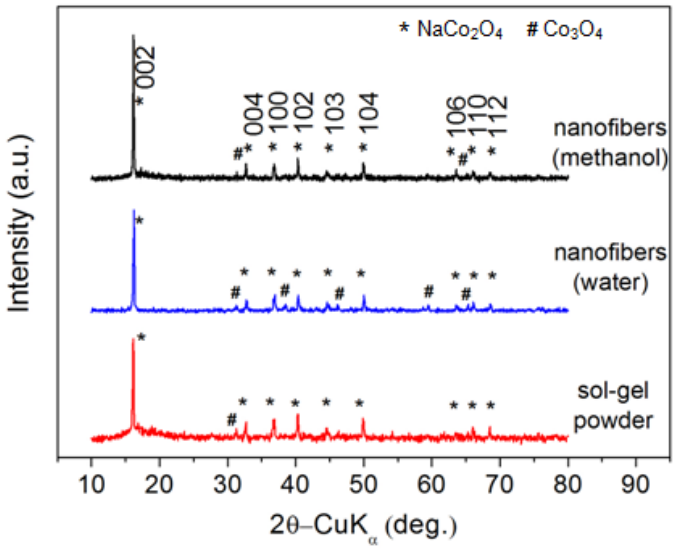

Figure 7-7 X-ray diffraction patterns of electropun nanofibers and sol-gel powder.

7.3.4 Summary

In summary, $Na_xCo_2O_4$ nanofibers with diameters around 200nm have been successfully fabricated by electrospinning method. The isolated fibers shows fine grain size around 20 nm after annealing process, but there could also be severe sodium loss according to the electron diffraction result. For the mass production of $Na_xCo_2O_4$ nanofibers, the annealed mat was able to form a major

crystal structure phase of $NaCo_2O_4$, but the original fiber structure was lost during high temperature annealing process.

7.3 $Na_xCo_2O_4$-TiO_2 Nanocomposites by Electrospinning Method

In order to sustain the nanofiber structure that was produced through electrospinning process, a $Na_xCo_2O_4$ -TiO_2 core-shell structure is designed to isolate each $Na_xCo_2O_4$ nanofibers.

7.3.1 Coaxial electrospinning processing

A schematic of core-shell electrospinning process is shown in Figure 7-8(A). A actual setup is shown in Figure 7-8(C). The setup consists of two coaxial capillaries, which can be loaded with different solutions. When the high voltage is applied to the liquid drop, a compound liquid jet is formed because of coaxial solution set-up, and this core-shell structured liquid jet is stretched into core-shell nanofibers by the same process of normal electrospinning.

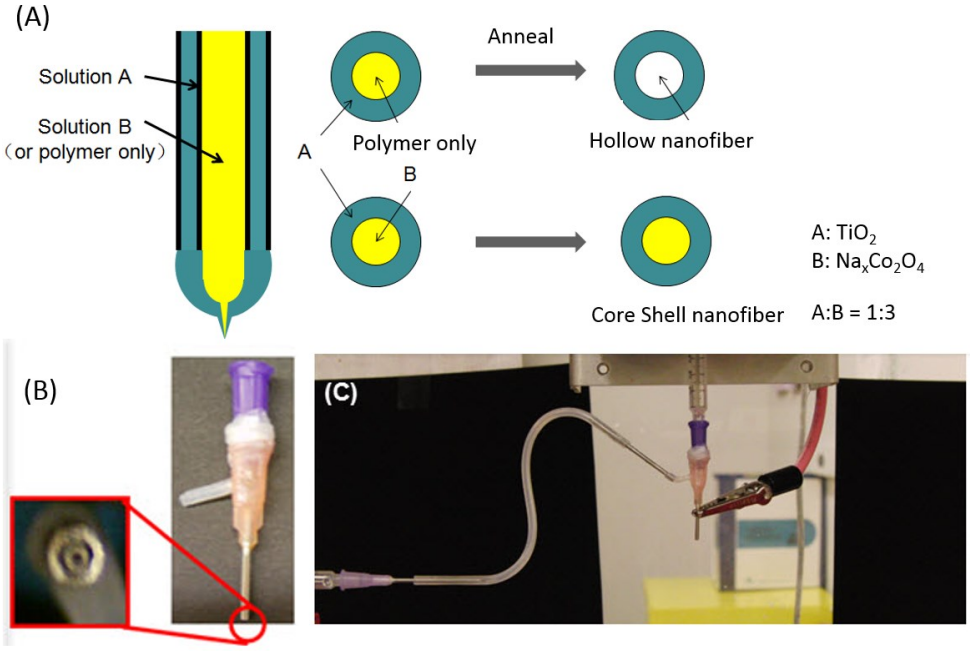

Figure 7-8 Schematic of coaxial electrospinning method.

The setup can also be used to fabricate hollow nanofibers, when the outer layer solution A uses ceramics sol, and inside layer uses pure polymer solution. After electrospinning process with this special coaxial capillaries, nanofibers with core-shell structure (A, shell; B, core) is fabricated. Hollow structure can be obtained subsequently by annealing this A/B core-shell nanofiber, since pure polymer phase (B) will turn into carbon dioxide under high temperature in air. If solution A and B are both ceramic sols, then core-shell nanofibers can be obtained after annealing.

In this work, $Na_xCo_2O_4$ precursor was prepared by dissolving cobalt (II) acetate tetrahydrate (Aldrich, reagent grade) and sodium acetate trihydrate (Baker, reagent grade) into distilled water, with the mole ratio of Na:Co controlled at 1.1:2, and the concentration of Co in the water was set to be 1.2 mol/L. After the salt was fully dissolved, the aqueous solution was mixed with same volume of methanol, and then PVP with molecular weight of 1,300,000 and concentration of 0.08 g/ml was added into the precursor solution and stirred until a homogeneous polymer solution was formed. TiO_2 precursor was prepared by dissolving $Ti(OBu)_4$ and PVP into methoxyethanol with a Ti concentration of 0.06 mol/L and a PVP concentration of 0.08 g/ml. The core-shell $Na_xCo_2O_4$ -TiO_2 nanofiber was prepared by co-axial electrospinning of these two precursors with a feed rate ratio of 3:1.

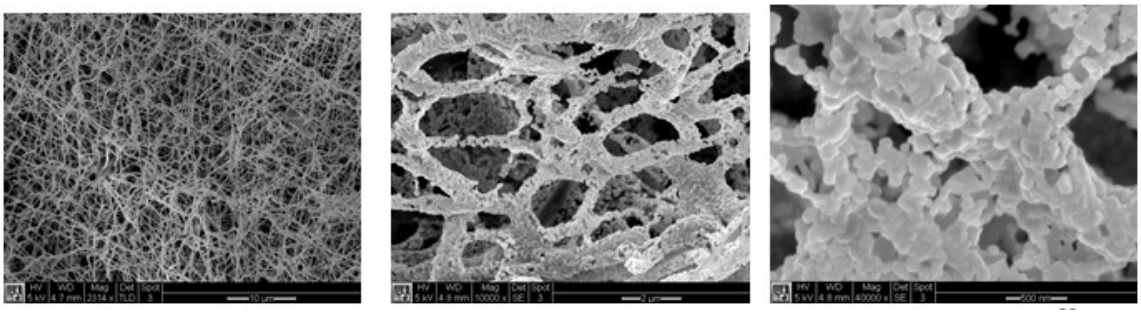

Figure 7-9 SEM of $Na_xCo_2O_4$ -TiO_2 coaxial electrospun nanofibers.

7.3.2 Microstructure and crystal structure analysis

As shown in Figure 7-9, it is difficult to identify the coreshell structure from the SEM images. The nanofiber structure of $Na_xCo_2O_4$-TiO_2 nanofiber survives after high temperature annealing, and the grain size is less than 100 nanometers.

Since core-shell electrospinning is rather complicated to operate and very inefficient for mass production, it would be better to check that whether this is process necessary. If a random mixed electrospinning process or mixed sol-gel process will do the job, then there is no need to go through the difficult core-shell electrospinning. In order to make a thorough comparison, all the samples are fabricated using same precursor and annealing procedure but with different solution processing method. The XRD result is shown in Figure 7-10. All the samples shows $Na_xCo_2O_4$ as its major phase, even with nearly 30% TiO_2 in the solution. However, instead of showing the TiO_2 peak in the composite samples, the peak of Co_3O_4 is shows up, and the possible explanation is that the Titanium ion in the TiO_2 exchange of position with the Cobalt ions during annealing, and the excess cobalt ions forms Co_3O_4, while the titanium mixed into the lattice of $Na_xCo_2O_4$ without showing any evident TiO_2 phases.

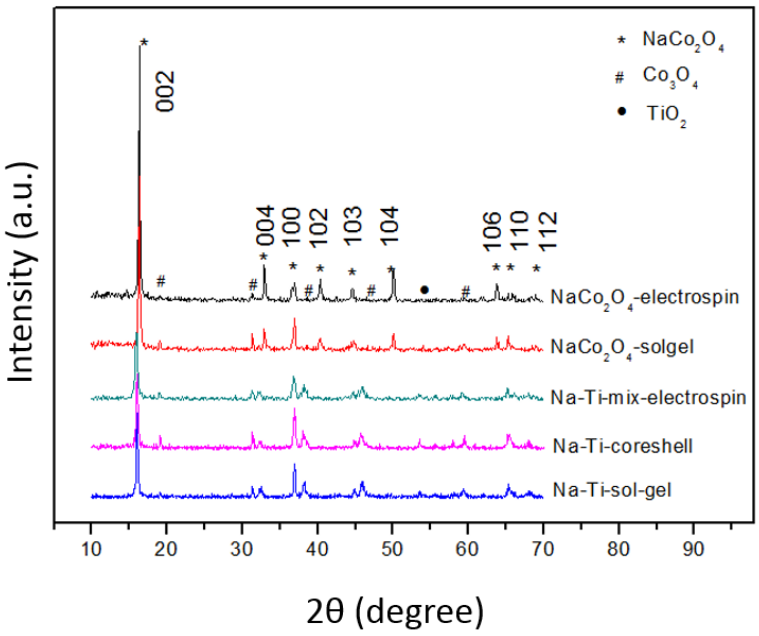

Figure 7-10 XRD of $NaCo_2O_4$ processed by different solution based methods.

A group of SEM images in Figure 7-11 shows the comparison of the grain size. It is obvious that the core-shell one has the smallest grain size, and all the Na-Ti composites show particle size less than 500 nm. And for pure $Na_xCo_2O_4$-TiO_2 sample, either from sol-gel or electrospinning processing, the grain size goes up to 5 μm, and they clearly shows the 2D plate structure. Compared to the sol-gel processed powder, the microplates shown in electrospinning sample are more likely to be separately from each other, and with a thinner and more uniform thickness.

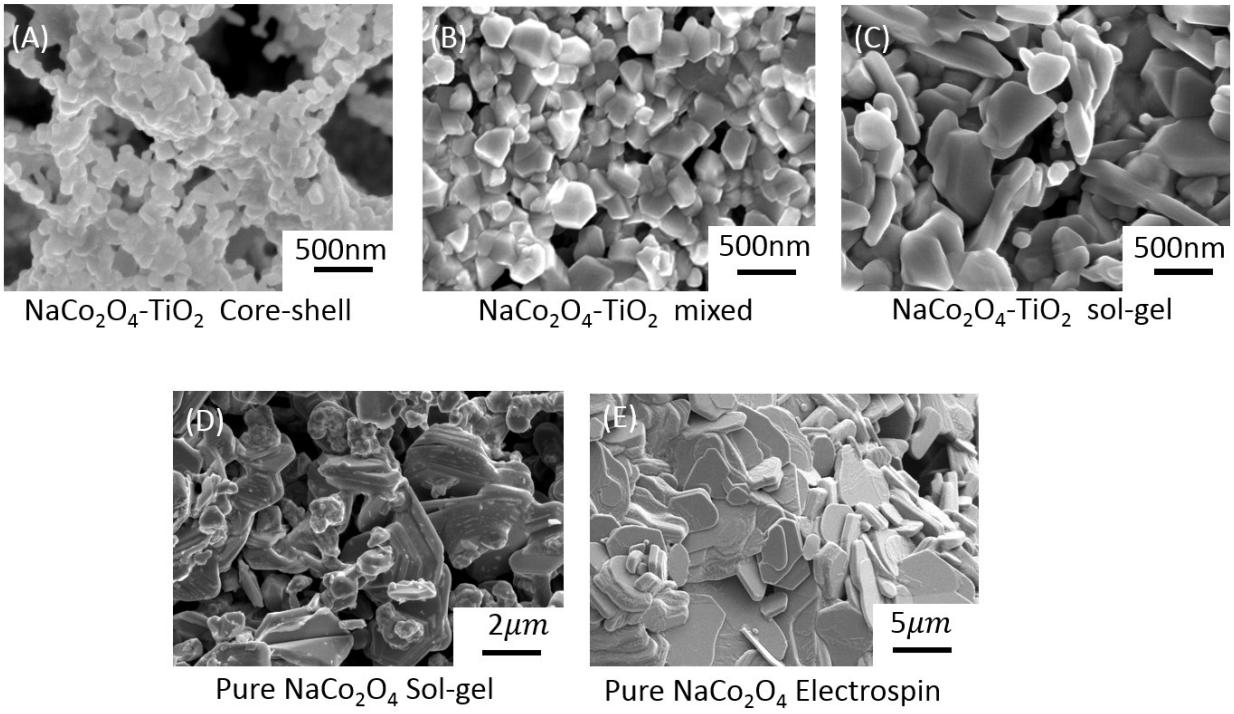

Figure 7-11 SEM images of $Na_xCo_2O_4$ -TiO_2 processed by different solution based methods.

7.3.3 Thermoelectric properties

All the samples shown in section 7.3.2 are consolidated into bulk samples for thermoelectric properties measurement.

Bulk sample preparation:

- *Cold press recipes:* Most samples went through cold press process. The powders are compressed under 600 MPa using a 13mm ID stainless steel die with a 15 ton hydraulic press. After consolidation, the pellet is annealed at 750℃ for 12 hours.
- *Hot press recipes:* One sample is consolidated using hot press technique. The powder is compressed under 100MPa using a home-made half-inch diameter alumina die, and heated to 800℃ for 1 hour.

Density measurement:

The density of the compressed pellet is measured using Archimedes method, as shown in Table 7-2. The density of all the cold pressed pellets are very low except the pellet made from electrospun powder of pure phase $NaCo_2O_4$. The relative high density of pure electrospun sample could be due to the loose bonding between the microplates and uniform size distribution. The hot press sample has a much higher density than the cold press samples as expected.

Table 7-2 Density of the fabricated pellets (unit: g/cm^3).

Sol-gel-cold-press	Electrospin-cold-press
3.108	3.77

Na-Ti-Core Shell-ES	Na-Ti-Mixed-ES	Na-Ti-Mixed-SG	Mixed-SG-Hot-Press
3.124	3.127	3.339	4.026

Thermoelectric properties

Thermoelectric properties of all pellets prepared were measured using home-built Seebeck and resistivity measurement system, and the thermal properties were measured using laser flash method. As shown in Figure 7-12, the $Na_xCo_2O_4$-TiO_2 composite process does largely reduced the thermal conductivity, and the core-shell structure sample have the lowest thermal conductivity as we expected. On the other hand, the electrical conductivity of the cold pressed composite sample is too low, and as a result *ZT* is much lower than those unmodified sample.

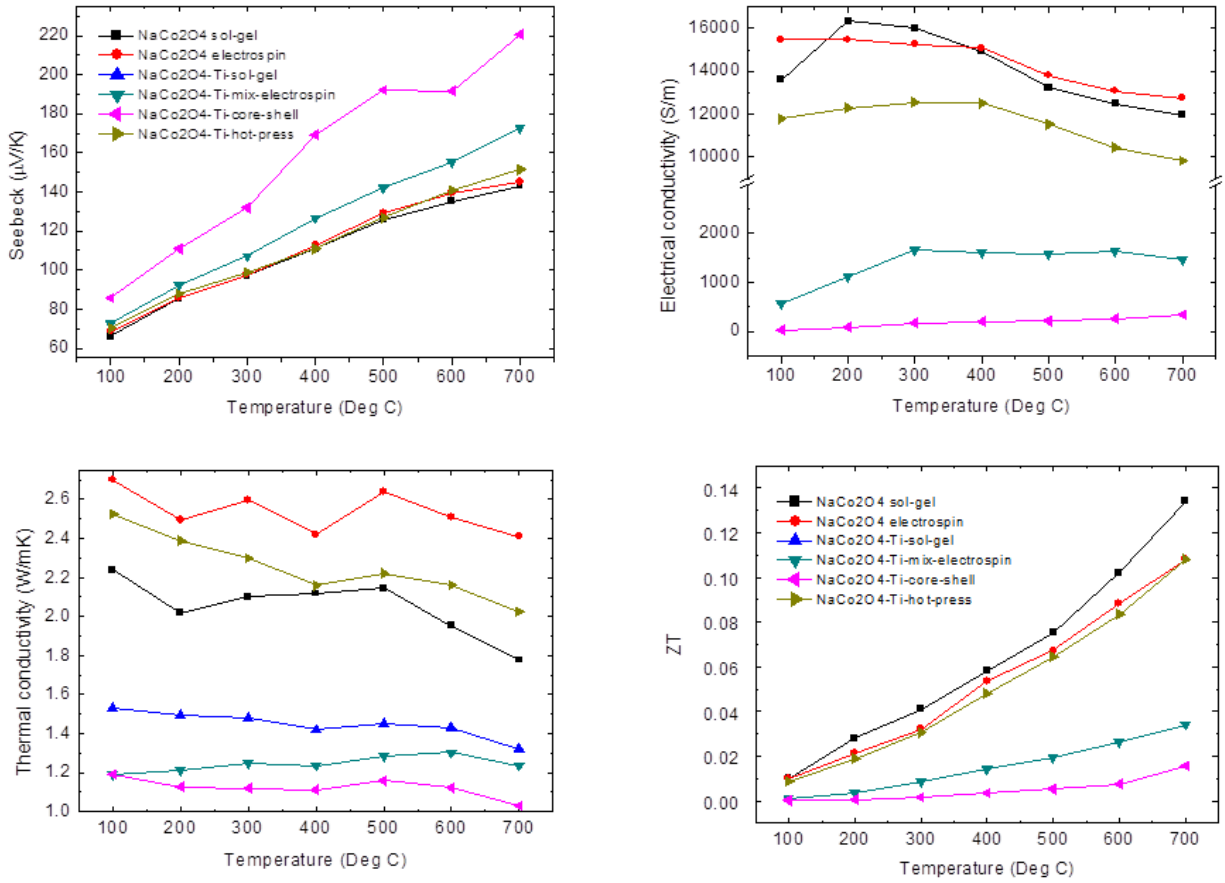

Figure 7-12 Thermoelectric properties of $Na_xCo_2O_4$ processed by different solution based methods.

7.3.4 Summary

In summary, co-axial electrospinning method has been explored to fabricate $Na_xCo_2O_4$-TiO_2 nanocomposites. Compared to all other techniques, the co-axial electrospinning produced the smallest particle size and the lowest thermal conductivity, but because of the poor electrical conductivity, the *ZT* value of $Na_xCo_2O_4$ - TiO_2 nanocomposites was not improved.

7.4 Highly Textured $Na_xCo_2O_4$ by Combustion Synthesis

7.4.1 Introduction of Combustion Synthesis

Solution based combustion synthesis is a versatile, simple and fast process for fabrication of a variety of nanosize materials. This process involves a self-sustained reaction in homogeneous solution of different oxidizer and fuels [83, 84]. In this work, sodium nitrate and cobalt nitride are used as oxidizers, urea and polyacrylic acid (PAA) are used as fuels.

7.4.2 Combustion synthesis recipes

Two recipes have been adopted for $Na_xCo_2O_4$ synthesis. The main difference of the two recipes was the fuel: one was used urea $CO(NH_2)_2$, and the other used PAA.

Recipe 1:

$NaNO_3$, $Co(NO_3)_2$, and $CO(NH_2)_2$ powders of a mole ratio 9:12:25 were dissolved in deionized water, according to following formula:

$$9NaNO_3+12Co(NO_3)_2+25CO(NH_2)_2 \xrightarrow{500degC} 6Na_{1.5}Co_2O_4+29N_2+25CO_2+50H_2O$$

After all the solutes were dissolved, the solution was transfer into a flask, and heated by a hot plate with a temperature setting of 500℃. It took about1 hour to evaporate most of the water. When the solution became dark purple and viscous, it took an extra 5~ 10 minute to start the combustion process. The combustion reaction process was very short and less than 5 second. During the reaction, dark loose powder was produced. Figure 7-13 shows SEM images of the resulted powder from the combustion reaction. The particles are small and with an average particle size less than 500nm. From the shape, we can tell that the particles are of very good crystallinity. But

unfortunately, it is not the $Na_xCo_2O_4$ phase. An energy dispersive x-ray spectroscopy (EDX) result of the sample shows a strong evidence of sodium loss during the fabrication process, and only 6% atomic percentage of sodium element existed in the final product.

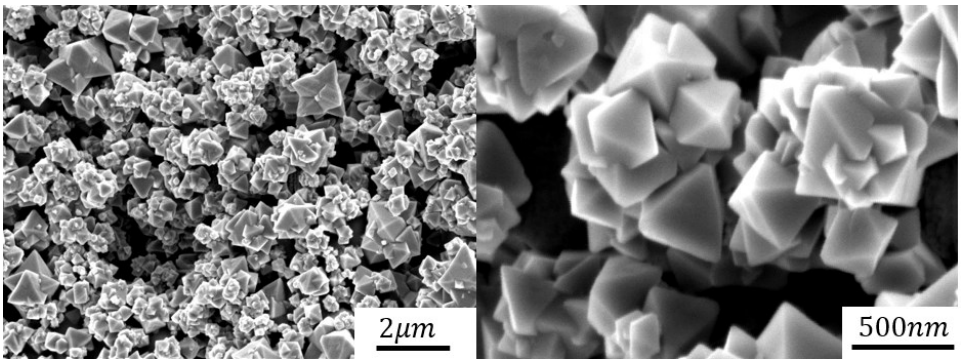

Figure 7-13 SEM images of particles fabricated from combustion synthesis with urea as the fuel.

Recipe 2:

$NaNO_3$, $Co(NO_3)_2$, and PAA powders of a weight ratio 1.2749 : 5.8206 : 1.26 were dissolved in deionized water, with a Co concentration of 0.2 M. All the other process was the same as recipe 1. It is worth noting here that the reactions are very strong in these two recipes. Normally a 500ml flask is used for the reaction of 20ml solution. The final product of recipe 2 was much looser than that from recipe1, and also less dark in color. From SEM images shown in Figure 7-14, the particle size was less than 50 nm with no sharp edges. XRD shows pure CoO peak. Since the particles didn't show good crystallinity, an annealing process was performed. After annealing, the particles size increased but not much, reaching about 70nm as an average particle size. And the crystal phase turned into Co_3O_4 with small portion of $Na_{0.6}CoO_2$.

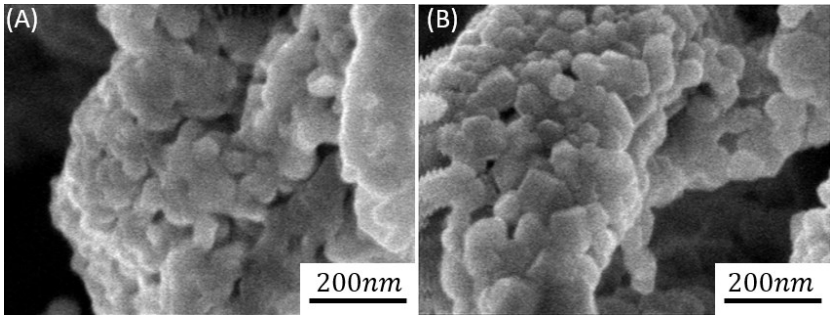

Figure 7-14 SEM images of particles fabricated from combustion synthesis with PAA as the fuel.

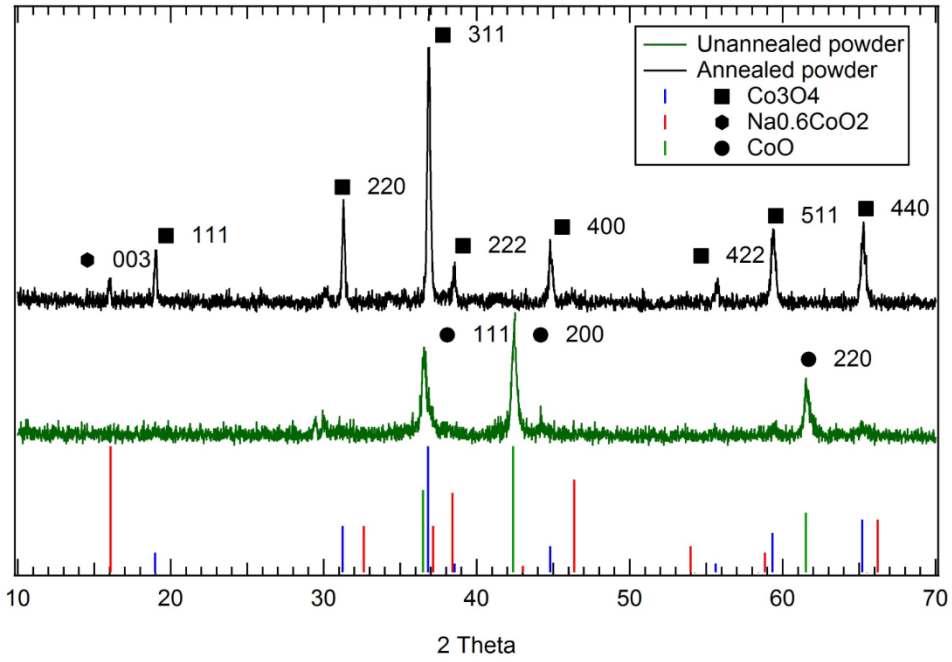

Figure 7-15 XRD patterns of powders fabricated from combustion synthesis with PAA as the fuel.

Modified recipe 2

A modification was made on the recipe trying to compensate the sodium loss during the annealing process. Instead of using a Na:Co ratio of 3:4, increased Na:Co ratios of 1:1 and 3:2 are adopted

in the starting solution in modified recipe 2. XRD result, shown in Figure 7-16, suggested an increased portion of $Na_xCo_2O_4$ phase after recipe modification. But the Co_3O_4 phase still existed. As the sodium increases, another unwanted effect takes place: SEM image in Figure 7-17 shows that the particle size increases greatly as the sodium component increases.

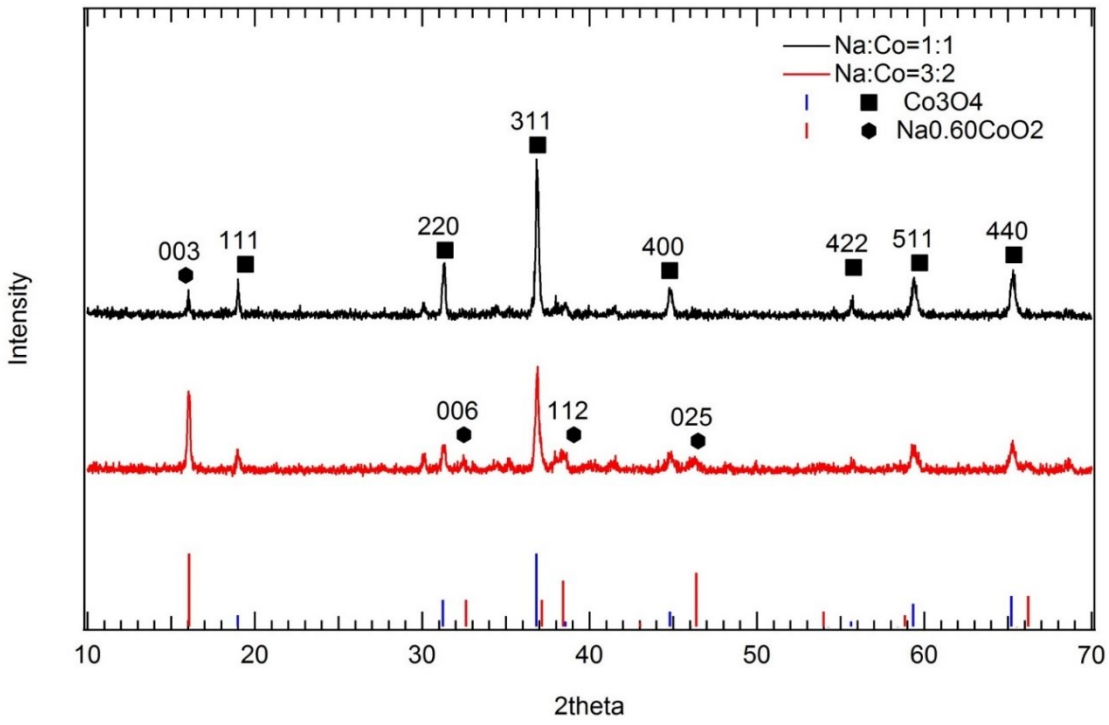

Figure 7-16 XRD patterns of powders fabricated from combustion synthesis when using a higher sodium composition.

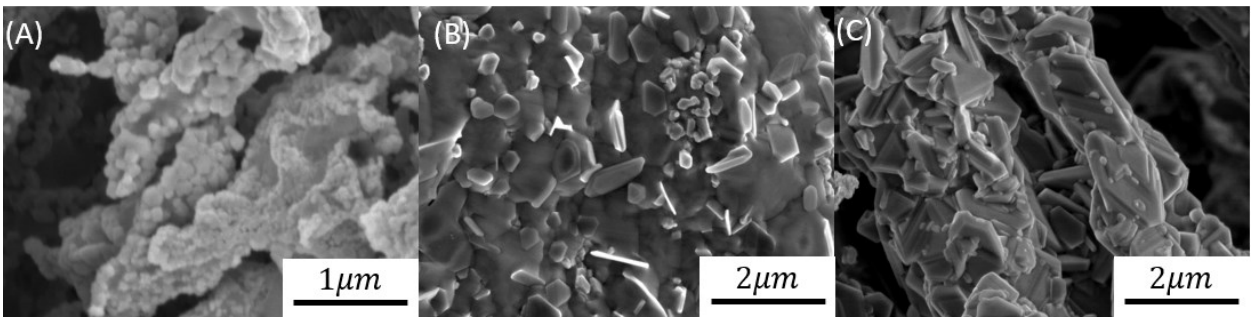

Figure 7-17 SEM images of combustion synthesized powders after annealing process; (A)Na:Co = 0.6:1;(B) Na:Co = 1:1; (C) Na:Co = 3:2.

Summary

In summary, it is not easy to directly fabricate pure and nanosized $Na_xCo_2O_4$ particle by combustion synthesis, because significant grain growth happens when the $Na_xCo_2O_4$ phase is formed. So instead of trying to reduce the particle size, it would be better to take advantage of this properties, and making extra-large $Na_xCo_2O_4$ crystals for highly textured sample.

7.4.3 Texturing process

It is reported that the combustion synthesized powders of layered cobalt oxides have been processed into large millimeter size nanosheet by chemical demixing and exfoliation [83]. The process can be modified to fabricate a highly textured bulk sample, with an average grain size larger than millimeter scale. Figure 7-18 shows the modified fabrication process for highly textured $Na_xCo_2O_4$.

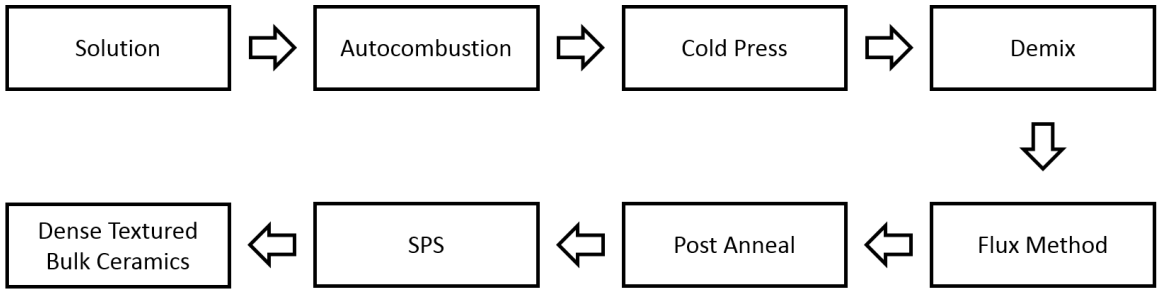

Figure 7-18 Fabrication process for highly textured $Na_xCo_2O_4$.

The first two steps have already been discussed in previous sections. Following steps are discussed below.

Cold press

The powder fabricated from combustion synthesis using recipe 2 was cold pressed into a 20x20 mm square pellet under a pressure about 500 MPa.

Chemical demixing

The purpose of this step is to create a sodium rich region inside the sample. Chemical demixing by electrical field is a common method to create metal ion concentration difference inside ceramic samples [85]. In this experiment, the square pellet was cut into a rectangular bar with a size of 10x20 mm. Then the bar was clamped between two aluminum electrodes, as shown in Figure 7-19. A constant current source was connected with the two electrode, and set to a current of 0.5A. The current density through the sample was about 10 mA/mm2. The entire assembly was put in to a furnace with an average temperature around 300°C. Normally the demixing process requires about 48 hrs, and after that the sample can be easily separated into two parts. As shown in Figure 7-19, the sample after demixing process has two distinct regions: the Na deficient region and

sodium rich region. The Na deficient part appears to be gray and porous, while the Na rich part appears black and dense. Noticed there are small portion of white substance on the electrode at Na rich side. This is the excess sodium that flows out of the sample along the current during the demixing process.

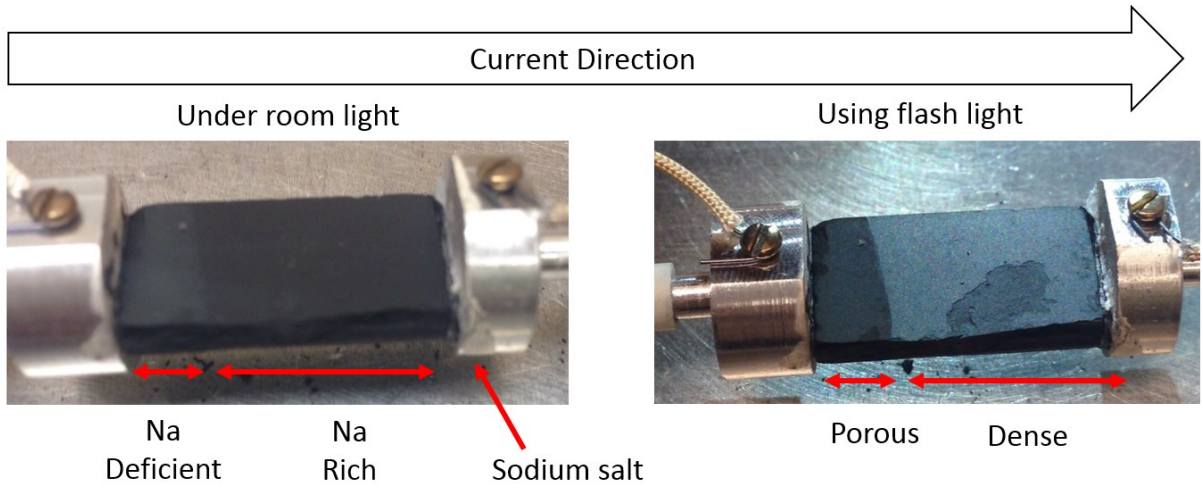

Figure 7-19 Photograph of samples after the chemical demixing process.

Flux Method

The flux method step is designed to grow large size crystal growth:

- Rapid heat sample up to 1030℃, keep for 15 minute
- Slowly Ramp down to 1000℃, with a cooling rate of 0.3 $℃/min$
- Cool down to room temperature with a cooling rate of 5 $℃/min$

During this process, in the Na rich part, the excess sodium is in its molten state and serves as a flux for $NaCo_2O_4$ crystal growth. As seen in Figure 7-20, The Na deficient part does not have as large crystal growth as the Na rich part in this step due to lack of sodium. The crystal growth

direction is along the direction of current applied, which is also perpendicular to the cold pressing direction.

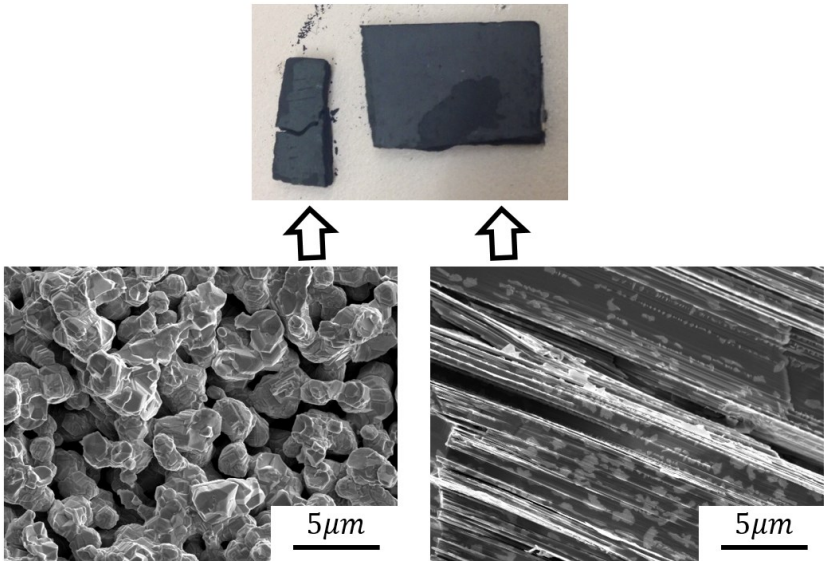

Figure 7-20 SEM images of demixed samples after flux method crystal growth.

Post annealing

The sample was further annealed at 850°C for 12 hrs. Figure 7-21 shows the surface and cross-section view of the annealed sample. The layered structure has a size larger than 200 μm, and all the layers are aligned in parallel to each other.

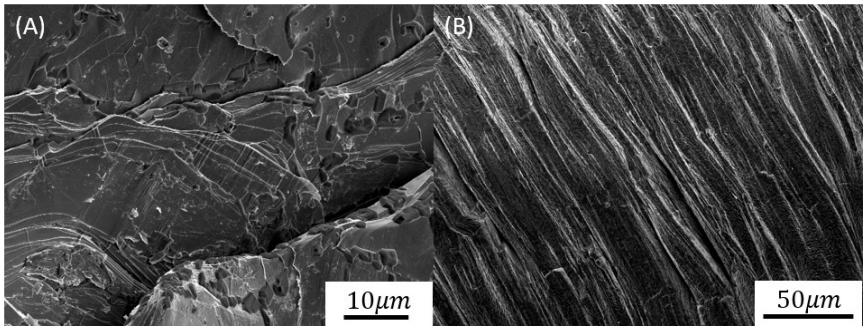

Figure 7-21 SEM images of demixed samples after post anneal step; (A) surface view; and (B) cross-section view.

SPS sintering

The demixed sample has many larges pores on the surface due to the melt of excess sodium salt in during the flux process. So SPS or hot press technique is needed to press the sample into a dense pellet for thermoelectric properties measurements. Several annealed samples from last step were stacked together and compressed into a single pellet using SPS at 900℃.

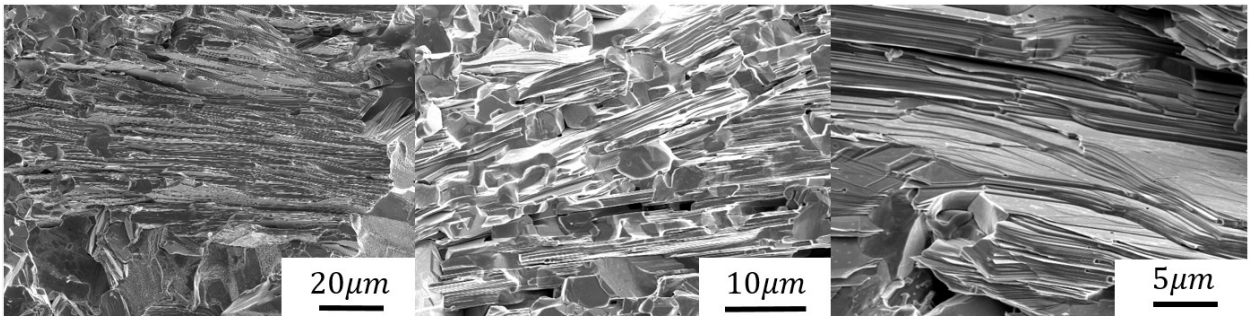

Figure 7-22 SEM images of the highly textured pellet.

7.4.4 Microstructure and crystal structure analysis

SEM

SEM images of the SPS sintered highly textured pellet are shown in Figure 7-22. The alignment of the layered structure is not as good as the sample before SPS process. The size of layered structures is also smaller, most of them less than 100 μm.

XRD

In Figure 7-23, for the textured sample, the XRD pattern only shows (00n) peaks. In contrast, the un-textured sample have all peaks expected. Lotgering factor [86] is calculated to quantify the degree of texture of the sample. A Lotgering factor of 0.85 is found in the XRD data of textured sample, while a Lotgering factor of 0.50 is found for the un-textured sample.

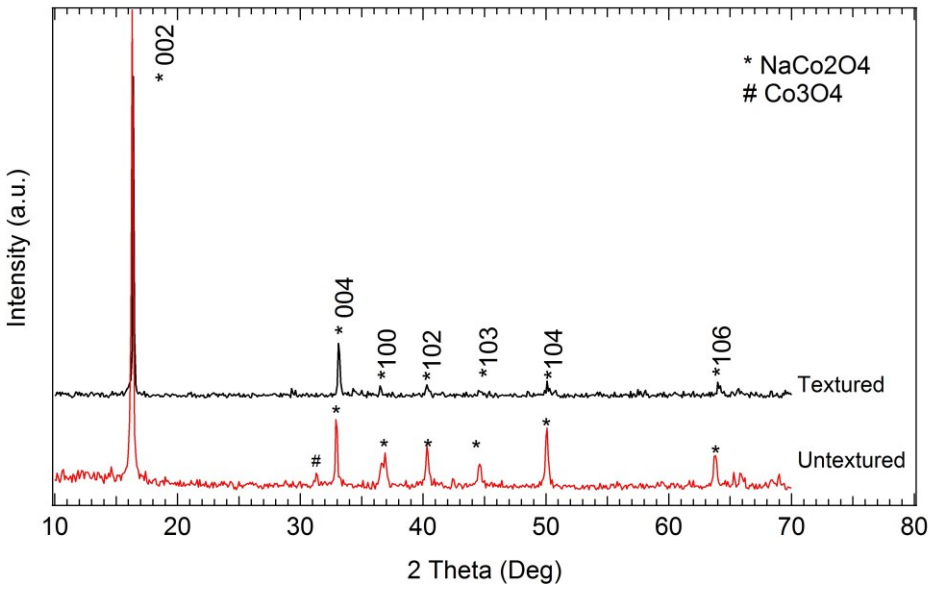

Figure 7-23 XRD pattern of the highly textured pellet; the pattern of an untextured pellet is displayed for a comparison.

7.4.5 Thermoelectric properties

The Seebeck coefficient and electrical resistivity of both textured and un-textured samples are measured from room temperature to 600°C, as shown in Figure 7-24.

The textured sample has a lower electrical conductivity than the un-textured sample, which is not expected. The possible reason of this poor electrical conductivity could due to the sodium loss during the SPS process. Because of this poor electrical conductivity, the textured sample exhibits a lower power factor over the entire temperature range.

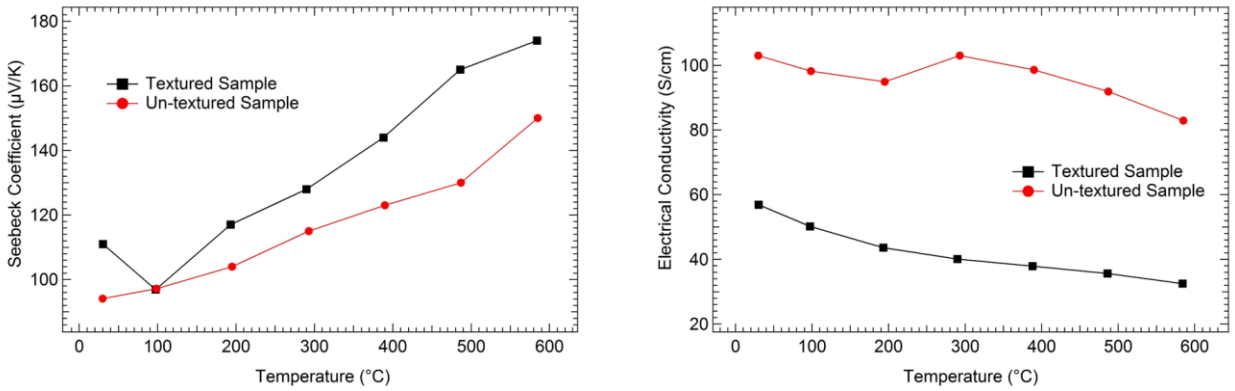

Figure 7-24 Electrical properties of a highly textured sample.

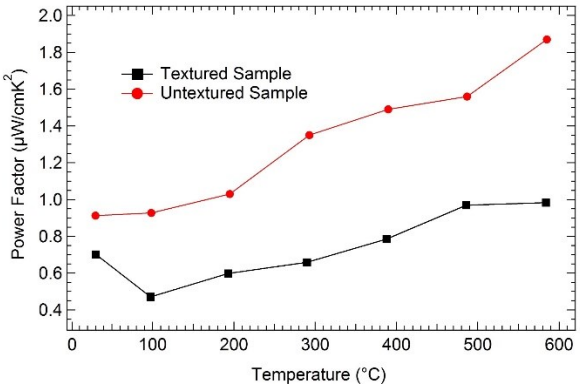

Figure 7-25 Power factor of a highly textured sample.

7.4.6 Summary

Solution based combustion synthesis method has been studied to synthesize $Na_xCo_2O_4$ nanoparticles. Sodium composition plays an important role in the grain growth process, and higher sodium concentration leads to larger crystal size. So it is difficult to get a pure $Na_xCo_2O_4$ phase without a substantial increase in grain size.

Texturing process is carried out using chemical demixing and flux method based on combustion synthesized powders. After the stage of flux method, SEM shows highly textured structure in the sample. After SPS process, the sample became less textured, with a Lotgering factor of 0.85. Although the Lotgering factor of textured sample is much higher, it does not show higher electrical conductivity or power factor possibly due to the loss of sodium.

7.5 Conclusion

In this chapter, several solution-based synthesis methods were studied for preparing $Na_xCo_2O_4$ ceramics with reduced grain size or increased texture.

(1) Electrospinning method was first studied to synthesize $NaCo_2O_4$ nanofibers. Electrospun nanofibers with fine grain structures were successfully fabricated through small volume production, but the crystal size increases greatly during mass production.

(2) Co-electrospinning method was attempted to solve the grain growth problem by adding a TiO_2 layer outside of each $NaCo_2O_4$ nanofiber. This method reduced the particle size and thermal conductivity as expected, but it also decrease the electrical conductivity of the material.

(3) Solution based combustion method was developed for nanoparticles preparation. However, the grain size increases with sodium composition during annealing process. So instead of try to reduce the grain size of $NaCo_2O_4$, a process that has a total opposite purpose has been carried out to produce highly textured sample with large grain size using demxing and flux methods. Composition modification and improvements of consolidation process are still needed for this method to further improve the thermoelectric performance.

Chapter 8 Conclusions and Future Work

8.1 Conclusions

8.1.1 Macroscale measurement system

High temperature Seebeck coefficient and electrical resistivity measurement system and high temperature Hall system have been designed, assembled and tested. Reliable and compact mechanical structures are designed for both systems. Original parts, such as dual-heater furnace for Seebeck coefficient measurement and compact heating stage for Hall effect measurement, are designed to overcome the limitations of commercial measurement systems.

For Seebeck and resistivity measurement system, different measurement methods have been studied, including steady-state method, quasi-steady-state method and DC dynamic method. The system is able to perform all three measurement mode without any changes of the hardware setup. DC dynamic method is developed specially based on the mechanical and electrical configuration of this system. This method is aiming to measure the Seebeck coefficient continuously without the need of establishing thermal equilibrium, which could save time for characterization of materials around phase transition temperature.

For Hall effect measurement system, the major improvement comes from its optimized mechanical design: Specially designed heating stage and vacuum chamber reduces the thickness of entire assembly down to 1 inch. This allows a maximum magnetic field around 1.88 T for the measurement. In addition, the probing mechanism and vacuum chamber designs greatly simplify the sample installation process and improve the accuracy and reliability of the measurement.

8.1.2 Nanoscale measurement system

Preliminary work has been carried out on localized thermal properties measurement by implementing scanning thermal microscopy with a heated probe. Different scanning modes and electronic control circuits have been developed and tested in details. Constant current mode is one of the most favorable measurement methods among the four options, due to its high signal resolution and simplicity for data analysis. Calibration procedures of the thermal probe are designed for this system, including the calibration of resistance-power relationship and resistance-temperature relationship. Possible artifacts and control parameters are also mentioned to further improve the quality of the measurement.

8.1.3 Nanostructuring of $Na_xCo_2O_4$ ceramics

Multiple methods, including ball milling, electrospinning, core-shell structuring and solution based combustion synthesis, have been studied trying to confine the grain size of $Na_xCo_2O_4$ ceramics for lattice thermal conductivity reduction.

Ball milling and electrospinning was found to be very effective to prepare nanosized particles, but the high temperature involved in the following annealing process for bulk specimen preparation ruined all the nanostructure and no reduction in thermal conductivity is observed. Similar grain growth has also been observed in combustion synthesized $Na_xCo_2O_4$. It is found that the sodium composition plays an important role on the resulting grain size. For combustion synthesis method, higher sodium composition leads to larger grain size and better crystallinity after annealing process.

$Na_xCo_2O_4$-TiO_2 core-shell structure was designed to isolate each $Na_xCo_2O_4$ nanofiber and prevent them from turning into micrometer sized crystals during the annealing process. The fine grain structure was successfully maintained after annealing process. The product shows a major crystal

phase of $NaCo_2O_4$ and a largely reduced thermal conductivity. However, the reduction in electrical conductivity was much greater than its thermal counterpart, resulting in a poor *ZT* value.

8.1.4 Texturing of $Na_xCo_2O_4$ ceramics

Instead of reducing lattice thermal conductivity, texturing method is aiming to improve the electrical conductivity in one direction. Through a combination of combustion synthesis, chemical demixing and flux method, a highly textured bulk sample was successfully fabricated. The resulting pellet has a Lotgering factor of 0.85, much higher than 0.5 of the non-textured sample. However, no improvement of electrical conductivity was observed in the textured sample, and a possible reason could be the change of sodium composition during the high temperature process.

8.2 Future Work

8.2.1 Thermoelectric instrumentation

Compared to Seebeck coefficient and Hall effect measurement systems, scanning probe microscopy (SPM) is a fairly new tool for materials characterization, especially for thermoelectric materials. Scanning thermal microscopy techniques have been successfully applied for probing the relative difference of local thermal properties, and the future research should be focused on the development of methods and theories to quantify the localized thermal conductivity. It is also worth exploring possible SPM techniques to probe localized Seebeck effect and carrier concentration at nanoscale, which are more challenging yet quite important for the development of nanostructured thermoelectric materials.

For macroscale measurements, the techniques are already mature and widely used in the area of thermoelectric research. However, several fundamental scientific and engineering problems are not yet solved or verified. For examples, linearity has often been used to check the validity of measured result in Seebeck coefficient measurement, because it can effectively eliminate the effect of offset voltages. But in the DC dynamic method discussed in this work, linearity was not quite effective to measure the reliability of the data, and this suggested that the error source could also vary in a linear manner versus temperature difference.

8.2.2 Materials synthesis

Although nanostructuring methods explored in this work did not improve the thermoelectric properties of $Na_xCo_2O_4$, similar methods could be applied to other oxide materials systems, such as ZnO and $SrTiO_3$, which were reported can be greatly improved through nanostructuring as reported [65]. From this work, it is found that not all thermoelectric materials can be or suitable to be nanosized. Crystals such as $Na_xCo_2O_4$ tend to grow at high temperature and in sodium rich environment, which is typical for bulk $Na_xCo_2O_4$ sample preparation. Foregoing research on texturing method shows that extra-large crystal size of $Na_xCo_2O_4$ can be obtained, as long as excess molten sodium flux is provided during annealing process. For high temperature application, highly textured samples could also be more stable than nanostructured samples. So texturing method could be a more efficient way for improving thermoelectric performance of $Na_xCo_2O_4$ and other similar material systems.

References

1. Yang, J.H. and T. Caillat, *Thermoelectric materials for space and automotive power generation.* Mrs Bulletin, 2006. **31**(3): p. 224-229.
2. Tritt, T.M., H. Boettner, and L. Chen, *Thermoelectrics: Direct solar thermal energy conversion.* Mrs Bulletin, 2008. **33**(4): p. 366-368.
3. Seebeck, T.J., *Magnetische polarisation der metalle und erze durck temperatur-differenz.* Abh. K. Akad. Wiss., 1823(265).
4. Peltier, J.C., *Nouvelles experiences sur la caloriecete des courans electriques.* Ann. Chem., 1834(LVI): p. 371-387.
5. Goldsmid, H.J., *Electronic refrigeration*. Vol. 76. 1986: Pion London.
6. Shi, L., et al., *Design and batch fabrication of probes for sub-100 nm scanning thermal microscopy.* Microelectromechanical Systems, Journal of, 2001. **10**(3): p. 370-378.
7. Nolas, G.S., D.T. Morelli, and T.M. Tritt, *Skutterudites: A phonon-glass-electron crystal approach to advanced thermoelectric energy conversion applications.* Annual Review of Materials Science, 1999. **29**: p. 89-116.
8. Rao, A.M., X.H. Ji, and T.M. Tritt, *Properties of nanostructured one-dimensional and composite thermoelectric materials.* Mrs Bulletin, 2006. **31**(3): p. 218-223.
9. Heremans, J.P., et al., *Enhancement of thermoelectric efficiency in PbTe by distortion of the electronic density of states.* Science, 2008. **321**(5888): p. 554-557.
10. Broido, D.A. and T.L. Reinecke, *Effect of Superlattice Structure on the Thermoelectric Figure of Merit.* Physical Review B, 1995. **51**(19): p. 13797-13800.
11. Linchung, P.J. and T.L. Reinecke, *Thermoelectric Figure of Merit of Composite Superlattice Systems.* Physical Review B, 1995. **51**(19): p. 13244-13248.
12. Harman, T.C., et al., *Quantum dot superlattice thermoelectric materials and devices.* Science, 2002. **297**(5590): p. 2229-2232.
13. Bottner, H., G. Chen, and R. Venkatasubramanian, *Aspects of thin-film superlattice thermoelectric materials, devices, and applications.* Mrs Bulletin, 2006. **31**(3): p. 211-217.
14. Venkatasubramanian, R., et al., *Thin-film thermoelectric devices with high room-temperature figures of merit.* Nature, 2001. **413**(6856): p. 597-602.

15. Hochbaum, A.I., et al., *Enhanced thermoelectric performance of rough silicon nanowires.* Nature, 2008. **451**(7175): p. 163-U5.
16. Boukai, A.I., et al., *Silicon nanowires as efficient thermoelectric materials.* Nature, 2008. **451**(7175): p. 168-171.
17. Szczech, J.R. and S. Jin, *Mg2Si nanocomposite converted from diatomaceous earth as a potential thermoelectric nanomaterial.* Journal of Solid State Chemistry, 2008. **181**(7): p. 1565-1570.
18. Ebling, D.G., et al., *Structure and thermoelectric properties of nanocomposite bismuth telluride prepared by melt spinning or by partially alloying with IV-VI compounds.* Physica Status Solidi-Rapid Research Letters, 2007. **1**(6): p. 238-240.
19. Mi, J.L., et al., *Thermoelectric properties of n-type CoSb3 nanocomposite prepared by in situ solvothermal synthesis and hot pressing.* Journal of Inorganic Materials, 2008. **23**(4): p. 715-718.
20. Chatterjee, S., *Titania-germanium nanocomposite as a thermoelectric material.* Materials Letters, 2008. **62**(4-5): p. 707-710.
21. Abramson, A.R., et al., *Fabrication and characterization of a nanowire/polymer-based nanocomposite for a prototype thermoelectric device.* Journal of Microelectromechanical Systems, 2004. **13**(3): p. 505-513.
22. Nolas, G.S., J. Poon, and M. Kanatzidis, *Recent developments in bulk thermoelectric materials.* Mrs Bulletin, 2006. **31**(3): p. 199-205.
23. Dresselhaus, M.S., et al., *New directions for low-dimensional thermoelectric materials.* Advanced Materials, 2007. **19**(8): p. 1043-1053.
24. Heremans, J.P., et al., *Thermoelectric power of bismuth nanocomposites.* Physical Review Letters, 2002. **88**(21).
25. Zhou, M., J.F. Li, and T. Kita, *Nanostructured AgPbmSbTem+2 system bulk materials with enhanced thermoelectric performance.* Journal of the American Chemical Society, 2008. **130**(13): p. 4527-4532.
26. Toberer, E.S., A.F. May, and G.J. Snyder, *Zintl Chemistry for Designing High Efficiency Thermoelectric Materials.* Chemistry of Materials, 2010. **22**(3): p. 624-634.
27. Li, Q., Z.W. Lin, and J. Zhou, *Thermoelectric Materials with Potential High Power Factors for Electricity Generation.* Journal of Electronic Materials, 2009. **38**(7): p. 1268-1272.
28. Salzgeber, K., et al., *Skutterudites: Thermoelectric Materials for Automotive Applications?* Journal of Electronic Materials, 2010. **39**(9): p. 2074-2078.
29. Kanatzidis, M.G., *Nanostructured Thermoelectrics: The New Paradigm?* Chemistry of Materials, 2010. **22**(3): p. 648-659.

30. Ohta, H., K. Sugiura, and K. Koumoto, *Recent progress in oxide thermoelectric materials: p-type Ca3CO4O9 and n-type SrTiO3-.* Inorganic Chemistry, 2008. **47**(19): p. 8429-8436.
31. Terasaki, I., I. Tsukada, and Y. Iguchi, *Impurity-induced transition and impurity-enhanced thermopower in the thermoelectric oxide NaCo2-xCuxO4.* Physical Review B, 2002. **65**(19).
32. Koumoto, K., I. Terasaki, and R. Funahashi, *Complex oxide materials for potential thermoelectric applications.* Mrs Bulletin, 2006. **31**(3): p. 206-210.
33. Julien, M.H., et al., *Electronic texture of the thermoelectric oxide Na0.75CoO2.* Physical Review Letters, 2008. **100**(9).
34. Kobayashi, W., et al., *Enhanced thermoelectric properties in a layered rhodium oxide with a trigonal symmetry.* Physical Review B, 2007. **76**(24).
35. Limelette, P., et al., *Strongly correlated properties of the thermoelectric cobalt oxide Ca3Co4O9.* Physical Review B, 2005. **71**(23).
36. Terasaki, I., et al., *Out-of-plane thermal conductivity of the layered thermoelectric oxide Bi2-xPbxSr2Co2Oy.* Physical Review B, 2004. **70**(21).
37. Terasaki, I., Y. Sasago, and K. Uchinokura, *Large thermoelectric power in NaCo2O4 single crystals.* Physical Review B, 1997. **56**(20): p. 12685-12687.
38. Takahata, K., et al., *Low thermal conductivity of the layered oxide (Na,Ca)Co2O4: Another example of a phonon glass and an electron crystal.* Physical Review B, 2000. **61**(19): p. 12551-12555.
39. Fujita, K., T. Mochida, and K. Nakamura, *High-temperature thermoelectric properties of NaxCoO2-delta single crystals.* Japanese Journal of Applied Physics Part 1-Regular Papers Short Notes & Review Papers, 2001. **40**(7): p. 4644-4647.
40. Ito, M., et al., *Synthesis of NaxCo2O4 thermoelectric oxides by the polymerized complex method.* Scripta Materialia, 2003. **48**(4): p. 403-408.
41. Kinaci, A., C. Sevik, and T. Cagin, *Electronic transport properties of SrTiO3 and its alloys: Sr1-xLaxTiO3 and SrTi1-xMxO3 (M = Nb, Ta).* Physical Review B, 2010. **82**(15).
42. Ohta, S., et al., *High-temperature carrier transport and thermoelectric properties of heavily La- or Nb-doped SrTiO3 single crystals.* Journal of Applied Physics, 2005. **97**(3).
43. Wang, Y., et al., *High Temperature Thermoelectric Response of Electron-Doped CaMnO3.* Chemistry of Materials, 2009. **21**(19): p. 4653-4660.
44. Zhang, F.P., et al., *Doping induced electronic structure and estimated thermoelectric properties of CaMnO3 system.* Physica B-Condensed Matter, 2011. **406**(6-7): p. 1258-1262.

45. Ohtaki, M., K. Araki, and K. Yamamoto, *High Thermoelectric Performance of Dually Doped ZnO Ceramics.* Journal of Electronic Materials, 2009. **38**(7): p. 1234-1238.
46. Jood, P., et al., *Al-Doped Zinc Oxide Nanocomposites with Enhanced Thermoelectric Properties.* Nano Letters, 2011. **11**(10): p. 4337-4342.
47. Mikami, M. and K. Ozaki, *Thermoelectric properties of nitrogen-doped TiO2-x compounds.* J. Phys.: Conf. Ser., 2012. **379**: p. 012006.
48. Martin, J., T. Tritt, and C. Uher, *High temperature Seebeck coefficient metrology.* Journal of Applied Physics, 2010. **108**(12).
49. Wood, C., A. Chmielewski, and D. Zoltan, *Measurement of Seebeck Coefficient Using a Large Thermal-Gradient.* Review of Scientific Instruments, 1988. **59**(6): p. 951-954.
50. Borup, K.A., et al., *Measurement of the electrical resistivity and Hall coefficient at high temperatures.* Review of Scientific Instruments, 2012. **83**(12): p. 123902.
51. Burkov, A., et al., *Experimental set-up for thermopower and resistivity measurements at 100-1300 K.* Measurement Science and Technology, 2001. **12**(3): p. 264.
52. Uher, C., *Use of high‐Tc superconductors for the determination of absolute thermoelectric power.* Journal of applied physics, 1987. **62**(11): p. 4636-4638.
53. Iwanaga, S., et al., *A high temperature apparatus for measurement of the Seebeck coefficient.* Review of Scientific Instruments, 2011. **82**(6): p. 063905.
54. Wood, C., D. Zoltan, and G. Stapfer, *Measurement of Seebeck coefficient using a light pulse.* Review of scientific instruments, 1985. **56**(5): p. 719-722.
55. Parker, W., et al., *Flash method of determining thermal diffusivity, heat capacity, and thermal conductivity.* Journal of applied physics, 1961. **32**(9): p. 1679-1684.
56. Freeman, R.H. and J. Bass, *An ac System for Measuring Thermopower.* Review of Scientific Instruments, 1970. **41**(8): p. 1171-1174.
57. Resel, R., et al., *Thermopower measurements in magnetic fields up to 17 tesla using the toggled heating method.* Review of scientific instruments, 1996. **67**(5): p. 1970-1975.
58. Chen, F., et al., *Low-frequency ac measurement of the Seebeck coefficient.* Review of Scientific Instruments, 2001. **72**(11): p. 4201-4206.
59. Zhou, Y., et al., *Fast Seebeck coefficient measurement based on dynamic method.* Review of Scientific Instruments, 2014. **85**(5): p. -.
60. Kasap, S., *Thermoelectric effects in metals: thermocouples.* Canada: Department of Electrical Engineering University of Saskatchewan, 2001.

61. Liu, H., et al., *Ultrahigh Thermoelectric Performance by Electron and Phonon Critical Scattering in Cu2Se1 - xIx.* Advanced Materials, 2013. **25**(45): p. 6607-6612.
62. Hall, E.H., *On a new action of the magnet on electric currents.* American Journal of Mathematics, 1879. **2**(3): p. 287-292.
63. PHILIPS'GLOEILAMPENFABRIEKEN, O., *A method of measuring specific resistivity and Hall effect of discs of arbitrary shape.* Philips research reports, 1958. **13**(1).
64. Wood, C., et al., *High temperature Hall - effect apparatus.* Review of scientific instruments, 1984. **55**(1): p. 110-113.
65. Jood, P., et al., *Al-doped zinc oxide nanocomposites with enhanced thermoelectric properties.* Nano letters, 2011. **11**(10): p. 4337-4342.
66. Wang, Y. and H.J. Fan, *Improved Thermoelectric Properties of La1-xSrxCoO3 Nanowires.* Journal of Physical Chemistry C, 2010. **114**(32): p. 13947-13953.
67. Hong, S., *Nanoscale phenomena in ferroelectric thin films*. 2004: Springer.
68. Chu, Y.H., et al., *Nanoscale domain control in multiferroic BiFeO3 thin films.* Advanced Materials, 2006. **18**(17): p. 2307-2311.
69. Ma, F., et al., *Nanocrystalline structure and thermoelectric properties of electrospun NaCo2O4 nanofibers.* The Journal of Physical Chemistry C, 2010. **114**(50): p. 22038-22043.
70. Wang, Z., J. Hu, and M.-F. Yu, *One-dimensional ferroelectric monodomain formation in single crystalline BaTiO 3 nanowire.* Applied physics letters, 2006. **89**(26): p. 263119-263119-3.
71. Fletcher, P.C., B. Lee, and W.P. King, *Thermoelectric voltage at a nanometer-scale heated tip point contact.* Nanotechnology, 2012. **23**(3).
72. Shi, L. and A. Majumdar, *Micro-nano scale thermal imaging using scanning probe microscopy*, in *Applied Scanning Probe Methods*. 2004, Springer. p. 327-362.
73. Dai, Z., E.A. Corbin, and W.P. King, *A microcantilever heater–thermometer with a thermal isolation layer for making thermal nanotopography measurements.* Nanotechnology, 2010. **21**(5): p. 055503.
74. Nelson, B. and W. King, *Temperature calibration of heated silicon atomic force microscope cantilevers.* Sensors and Actuators A: Physical, 2007. **140**(1): p. 51-59.
75. Takada, K., et al., *Superconductivity in two-dimensional CoO2 layers.* Nature, 2003. **422**(6927): p. 53-55.

76. Motohashi, T., et al., *Simultaneously enhanced thermoelectric power and reduced resistivity of NaxCo2O4 by controlling Na nonstoichiometry.* Applied Physics Letters, 2001. **79**(10): p. 1480-1482.
77. Nagira, T., et al., *Thermoelectric properties of (Na1-yMy)(x)Co2O4 (M=K, Sr, Y, Nd, Sm and Yb; y=0.01 similar to 0.35).* Journal of Alloys and Compounds, 2003. **348**(1-2): p. 263-269.
78. Nagira, T., M. Ito, and S. Katsuyama, *Thermoelectric properties of NaxCo2O4 prepared by the polymerized complex method and hot-pressing.* Materials Transactions, 2003. **44**(1): p. 155-160.
79. Tajima, S., et al., *Thermoelectric properties of highly textured NaCo2O4 ceramics processed by the reactive templated grain growth (RTGG) method.* Materials Science and Engineering B-Solid State Materials for Advanced Technology, 2001. **86**(1): p. 20-25.
80. Parker, W.J., et al., *Flash Method of Determining Thermal Diffusivity, Heat Capacity, and Thermal Conductivity.* Journal of Applied Physics, 1961. **32**(9): p. 1679-&.
81. Yarin, A.L., S. Koombhongse, and D.H. Reneker, *Taylor cone and jetting from liquid droplets in electrospinning of nanofibers.* Journal of Applied Physics, 2001. **90**(9): p. 4836-4846.
82. Maensiri, S. and W. Nuansing, *Thermoelectric oxide NaCo< sub> 2</sub> O< sub> 4</sub> nanofibers fabricated by electrospinning.* Materials chemistry and physics, 2006. **99**(1): p. 104-108.
83. Aksit, M., D.P. Toledo, and R.D. Robinson, *Scalable nanomanufacturing of millimetre-length 2D NaxCoO2 nanosheets.* Journal of Materials Chemistry, 2012. **22**(13): p. 5936-5944.
84. Zhang, Y., et al., *Effect of Sintering Temperature on the Texturing Behavior of NaCo2O4-delta Synthesized by Urea Auto-Combustion Method.* Journal of Materials Science & Technology, 2009. **25**(6): p. 742-744.
85. Monceau, D., et al., *Kinetic demixing of ceramics in an electrical field.* Solid State Ionics, 1994. **73**(3): p. 221-225.
86. Lotgering, F., *Topotactical reactions with ferrimagnetic oxides having hexagonal crystal structures—I.* Journal of Inorganic and Nuclear Chemistry, 1959. **9**(2): p. 113-123.